KAUNAS UNIVERSITY OF TECHNOLOGY

MARZIEH RABIEI

DEVELOPMENT AND ANALYSIS OF NANOCOMPOSITE BASED ON HYDROXYAPATITE FOR APPLICATION IN BIOENGINEERING

Doctoral dissertation
Technological Sciences, Mechanical Engineering (T 009)

Kaunas, 2023

This doctoral dissertation was prepared at Kaunas University of Technology, Faculty of Mechanical Engineering and Design, Department of Mechanical Engineering during the period of 2019–2023. The studies were supported by the Research Council of Lithuania.

The doctoral right has been granted to Kaunas University of Technology together with Vytautas Magnus University.

Scientific Supervisor
Prof. Hab. Dr. Arvydas PALEVIČIUS (Kaunas University of Technology, Technological Sciences, Mechanical Engineering, T 009).

Scientific Advisor
Prof. Dr. Giedrius JANUŠAS (Kaunas University of Technology, Technological Sciences, Mechanical Engineering, T 009).

Edited by: English language editor Brigita Brasienė (Publishing House *Technologija*), Lithuanian language editor Rozita Znamenskaitė (Publishing House *Technologija*).

Dissertation Defence Board of Mechanical Engineering Science Field:
Prof. Habil. Dr. Vytautas OSTAŠEVIČIUS (Kaunas University of Technology, Technological Sciences, Mechanical Engineering, T 009) – **chairman;**
Prof. Dr. Vytenis JANKAUSKAS, (Vytautas Magnus University, Technological Sciences, Mechanical Engineering, T 009);
Assoc. Prof. Dr. Sayed Ali HASSANZADEH-TABRIZI (Islamic Azad University, Iran, Technological Sciences, Materials Engineering, T 008);
Prof. Dr. Daiva ZELENIAKIENĖ (Kaunas University of Technology, Technological Sciences, Mechanical Engineering, T 009).

The official defence of the dissertation will be held at 10 a.m. on 13 January, 2023 at the public meeting of Dissertation Defence Board of Mechanical Engineering Science Field in the Meeting Room No. 1 of Student‘s Infocenter of Kaunas University of Technology.

Address: Studentu 50, Kaunas, LT-51368, Lithuania.
Tel. no. (+370) 37 300 042; e-mail doktorantura@ktu.lt

Doctoral dissertation was sent on 13 December, 2022.
The doctoral dissertation is available on the internet http://ktu.edu and at the libraries of Kaunas University of Technology (K. Donelaičio 20, Kaunas, LT-44239, Lithuania) and Vytautas Magnus University (K. Donelaičio 52, Kaunas, LT-44244, Lithuania).

© M. Rabiei, 2023

KAUNO TECHNOLOGIJOS UNIVERSITETAS

MARZIEH RABIEI

NANOKOMPOZITO KŪRIMAS HIDROKSIAPATITO PAGRINDU IR JO TYRIMAS BEI PANAUDOJIMAS BIOINŽINERIJOJE

Daktaro disertacija
Technologijos mokslai, mechanikos inžinerija (T 009)

Kaunas, 2023

Disertacija rengta 2019–2023 metais Kauno technologijos universiteto Mechanikos technologijos fakultete. Mokslinius tyrimus rėmė Lietuvos mokslo taryba.
Doktorantūros teisė Kauno technologijos universitetui suteikta kartu su Vytauto Didžiojo universitetu.

Mokslinis vadovas:
prof. habil. dr. Arvydas Palevičius (Kauno technologijos universitetas, technologijos mokslai, mechanikos inžinerija, T 009).

Mokslinis konsultantas:
prof. habil. dr. Giedrius Janušas (Kauno technologijos universitetas, technologijos mokslai, mechanikos inžinerija, T 009).

Redagavo: anglų kalbos redaktorė Brigita Brasienė (leidykla „Technologija“), lietuvių kalbos redaktorė Rozita Znamenskaitė (leidykla „Technologija“)

Mechanikos inžinerijos mokslo krypties disertacijos gynimo taryba:
Prof. habil. dr. Vytautas OSTAŠEVIČIUS (Kauno technologijos universitetas, technologijos mokslai, mechanikos inžinerija, T 009) – **pirmininkas;**
Prof. dr. Daiva ZELENIAKIENĖ (Kauno technologijos universitetas, technologijos mokslai, mechanikos inžinerija, T 009);
Prof. dr. Vytenis JANKAUSKAS (Vytauto Didžiojo universitetas, technologijos mokslai, mechanikos inžinerija, T 009);
Doc. dr. Sayed ALI HASSANZADEH-TABRIZI (Islamo Azado universiteto Nadžafabado filialas, Nadžafabadas (IAUN), Iranas, technologijos mokslai, mechanikos inžinerija, T 009).

Disertacija bus ginama viešame Mechanikos inžinerijos mokslo krypties disertacijos gynimo tarybos posėdyje 2022 m. sausio 13 d. 10 val. Kauno technologijos universiteto Studentų infocentre, posėdžių kambaryje Nr. 1.

Adresas: Studentų g. 50, Kaunas, LT-51368, Lietuva.
Tel. (370) 37 300 042; el. paštas doktorantura@ktu.lt

Disertacija išsiųsta 2022 m. gruodžio 13 d.
Su disertacija galima susipažinti interneto svetainėje http://ktu.edu ir Kauno technologijos universiteto (K. Donelaičio g. 20, Kaunas, LT-44239, Lietuva) ir Vytauto Didžiojo universiteto (K. Donelaičio g. 52, Kaunas, LT-44244, Lietuva) bibliotekose.

© M. Rabiei, 2023

TABLE OF CONTENTS

LIST OF TABLES

LIST OF FIGURES

LIST OF ABBREVIATIONS

a	lattice parameter
$AgNO_3$	silver nitrate
B	bulk modulus
BET	Brunauer–Emmett–Teller
$CaCl_2$	calcium chloride
$Ca(NO_3)_2.4H_2O$	calcium nitrate tetrahydrate
$(CHCl_3)$	chloroform
$(CH_2OH)_3CNH_2$	tris(hydroxymethyl)aminomethane
CH_3COOH	acetic acid
C_{ij}	elastic stiffness constant values
c_l	velocity of longitudinal
Cu	copper
CuI	copper iodide
$CuSO_4$	copper (II) sulfate
c_t	velocity of transverse
C_2H_5OH	ethyl alcohol
(C_3H_6O)	acetone
(C_3H_8O)	isopropyl alcohol
DCCA	drying control chemical additive
DSC	differential scanning calorimetry
EDX	energy dispersive X-ray spectroscopy
E_{hkl}	Young's modulus of each plane
ESPI	speckle pattern interferometry
FTIR	Fourier-transform infrared spectroscopy
g	gram
h	hour
HA	hydroxyapatite
HCl	hydrochloric acid
(hkl)	index of planes
HNO_3	nitric acid
K	shape factor
KCl	potassium chloride
KI	potassium iodide
$K_2HPO_4.3H_2O$	potassium phosphate dibasic trihydrate
L	nanocrystal size
L	length of the sample
$MgCl_2.6H_2O$	magnesium chloride hexahydrate
NaCl	sodium chloride
$NaHCO_3$	sodium bicarbonate
NaOH	sodium hydroxide
Na_2SO_4	sodium sulfate

$(NH_2C(CH_2OH)_3 \cdot HCl)$	tris
PD	planar density
PVD	physical vapor deposition
PVTMS	polyvinyltrimethoxysilane
P_2O_5	phosphorus pentoxide
rpm	rate per minute
S	specific surface area
SBF	simulated body fluid
SEM	scanning electron microscope
S_{ij}	elastic compliance values
Si-O-Si	siloxane
SPS	spark plasma sintering
t	difference between two echoes
TEM	transmission electron microscopy
u	lattice strain energy density
USDM	uniform stress deformation model
VTMS	vinyltrimethoxysilane
W–H	Williamson–Hall
XRD	X-ray diffraction
β	full width at half maximum (FWHM)
ε	lattice strain
Θ	diffracted angle of the peak
λ	wavelength
$\lambda_{Cu_{K\alpha}}$	wavelength of copper as a source, 0.15405 nm
μ	shear modulus
ρ	density
σ	lattice stress
υ	poisson's ratio

ABSTRACT

This dissertation is written based on six published papers. First study focuses on the comparison of methods based on the XRD patterns for calculating the crystal size. In this case, XRD peaks of hydroxyapatite (HA) obtained from cow, pig, and chicken bones were presented, and crystallite size values were gained from the methods based on XRD. The Monshi−Scherrer method, out of all methods, provided a simple calculation and a reduction in error by applying least squares to the linear plot, and it gave crystallite size values of 60, 60, and 57 nm for cow, pig, and chicken, respectively. In the second study, a new method for obtaining Young's modulus of crystallite materials is presented. In this method, the Young's modulus of crystallite materials is obtained by X-ray diffraction. In this study, Young's modulus values were gained through the arbitrary planes, such as random (hkl) in the research. Young's modulus is calculated from the relationship between the elastic compliances, the geometry of the crystal lattice and the planar density of each diffracted plane by X-ray diffraction. This method is introduced with planar density values as the X-axis and the Young's modulus values as the Y-axis that the intercept coul register Young's modulus with high accuracy. In addition, sodium chloride (NaCl) with the FCC crystal lattice was selected as an example, and the Young's modulus value of NaCl was measured to be 35.68 GPa. In the third study, this method is used for the Perovskite lattice ($CaTiO_3$), and the Young's modulus of unit cell, super cells (2×2×2) and symmetry cells were calculated. The extracted Young's modulus values were recorded as 162.62, 151.71, and 152.21 GPa for the unit cell, super cells (2×2×2), and symmetry cells tandemly. Moreover, the calculated Young's modulus value of the symmetry cells agreed well with the experimental methods and data from the literature. In the fourth study, this method was used for HA as a hexagonal example of unit cell and super cells (2×2×2). The Young's modulus values extracted by this method were 108.15 and 121.17 GP for unit cell and super cells (2×2×2), respectively. In the fifth study, the hair band was chosen as a new approach to prepare big and open porosities of a nanocomposite that consisted of Ag/HA/PVTMS, because these porosities are the best sites for blood cells nucleation and growth. The physical, mechanical, and bioactive properties of the prepared nanocomposites were investigated, and the maximum value of compressive strength was measured to be 15.71 MPa at a strain of ~0.77. In the sixth study, a nanocomposite consisting of 5 mol% crystalline CuI-doped HA was prepared for the first time by a simple chemical method and calcined at different temperatures, such as 300 °C, 500 °C, 700 °C, and 900 °C, respectively. In this study, HA played a role of the matrix, and CuI was the reinforcement. Furthermore, the mechanical properties of these nanocomposites were fully discussed extensively by using the ASTM-E9 standard, and CuI (5 mol%)/HA, calcined at 900 °C, was in a better range than the other compounds, and the σ_{yc} and hardness values were reported to be 7.32 Mpa and 40.81 HV, respectively.

1.INTRODUCTION

Hydroxyapatite (HA) is a diverse material complex that is a candidate for being utilized in the fabrication of bio composites. HA is a ceramic, and there are several methods to prepare artificial HA, such as a solid state reaction, mechanochemistry, sonochemistry, hydrothermal, sol–gel, and precipitation. The chemical formula of HA is ($Ca_{10}(PO_4)_6(OH)_2$), and recently, HA has been considered by the researchers as a potential adsorbent for heavy metals due to its large specific surface area, high thermal and chemical stability, and high ion exchange capacity. There are two crystal structures of HA, i.e., 1) hexagonal structure and 2) monoclinic structure. In order to improve the properties of HA, the researchers replaced the Ca^{2+} ions with other metal ions. The structure of HA consists of a quasi-compact packing of phosphate groups with two types of Ca^{2+} ions, such as tunnel and parallel positions. One of the main characteristics of the HA structure is the ability of a large number of substitutions, which does not change the basis of the crystallographic structure. HA has a hexagonal system with a $P6_3/m$ space group and little deviation from the stoichiometry. Different approaches have been extensively explored to improve the mechanical properties of HA ceramics, such as making composites and controlling microstructures through the novel sintering techniques or using nanostructured powders. Moreover, the most and emergent application of HA are attributed to the bone repairing, although being biocompatible, due to its brittleness, and it does not meet the mechanical requirements of a bone replacement; therefore, the attention to the mechanical properties and structural geometry of HA can be helpful in a research as well as in the industrial applications. Understanding the mechanical properties of HA during the crystallization and growth stages of the synthesis processes is important, because the Young's modulus affects the growth of HA crystal in mechanically strained environments directly. Paying attention to the details of the structural geometry of HA is essential for employing easy, cost-effective, and reliable method to determine the Young's modulus. Furthermore, for the investigation of structural geometry of HA, the study of X-ray diffraction is essential.

XRD profile analysis is a convenient and powerful method to investigate crystallite size, lattice strain, and mechanical properties. Furthermore, X-ray diffraction is a conventional procedure to analyze materials. Moreover, X-ray diffraction can determine the crystalline size, stress, strain, and density energy of materials. Utilizing X-ray patterns and crystallography are the easy ways for calculating the size of nanocrystallites.

Young's modulus can be defined as the ratio of stress to strain. The elastic constants are specific to the reaction of the lattice crystal against forces, as determined by the bulk modulus, shear modulus, Young's modulus, and Poisson's ratio. The elastic constants play a role in determining the strength of the materials. Furthermore, elastic constant values have a correlation with the planar density values due to the bonding characteristic between adjacent atomic planes and the anisotropic character of the bonding and structural stability. Moreover, elastic

constants are related to stress and strain and depend on the configuration of the crystal lattice; therefore, the elastic constants derive from the planes in the crystal lattice, and the crystallographic planes that are equivalent have similar atomic planar densities. Planar density is the fraction of the total crystallographic plane area that is occupied by atoms. The planar density is a significant parameter of a crystal structure, and it is specified as a number of atoms per unit area on a plane. X-ray diffraction is the only technique that allows determining both the mechanical and microstructural states of each diffracted plane. Diffracted planes are utilized as a strain gauge to measure Young's modulus in one or several planes/directions of the diffraction vector. Nowadays, X-ray diffraction is a conventional technique for the study of crystal structures and atomic spacing. X-ray diffraction is based on the constructive interference of monochromatic X-rays and a crystalline sample. Hanabusa et al. presented a new method for measuring the elastic constant of cementite phase in steel, but the restriction of this method was related to utilization of high-angle region only, and it was not capable to detect in low-angle regions. In contrast, Williamson–Hall (W–H) method corresponded to calculating and estimating strain well. The lattice strain (ε), lattice stress (σ), and lattice strain energy density (u) can be extracted with the W–H method. The elastic constants are specified from the lattice crystal deformation against force. These elastic moduli are the following: Young's modulus, shear modulus, and volumetric modulus. These modules are registered via inherent elastic properties of materials and their resistance to deformation due to the loading. The elastic behavior of materials is described by models, such as Cauchy elastic, hypo-elastic, and hyper-elastic. A hyper-elastic is a constitutive model for ideally elastic material that responds to stress gain from a strain energy density function, while for hypo-elastic material, their governing equation is independent from finite strain quantity, except in the linearized state. The elastic properties are intimately connected to the crystal structure, the intrinsic character of bonding between the atoms and the anisotropic nature of materials; therefore, the elastic constants can be derived from the crystal lattice calculations. In this study, a new method and a technique for calculating and measuring the crystallite size and Young's modulus are presented. NaCl (FCC), $CaTiO_3$ (SC), and HA (HCP) are given as examples. In addition, the synthesis, physical and mechanical properties of two composites consisting of CuI/HA and Ag/PVTMS/HA are discussed in detail.

The aim of this work is the synthesis and investigation of mechanical properties of natural and artificial hydroxyaoatite (HA) and nanocomposites based on HA with establishing a new comprehensive technique to analyze the nanocrystal size, Young's modulus with high accuracy, and performance in all crystallite components and applying research results for bioengineering.

In order to achieve the aim of this work, **the following objectives** have been formulated:

1)Comparison of all extracted methods from the X-ray diffraction for calculating the nanocrystal size of natural HA.
2)Investigation of the nanocrystal size of natural HA by X-ray diffraction.

3)Evaluation of a new technique for measuring Young's modulus as a function of planar density in the unit cell and super cells of crystal lattices. For example, the study of Young's modulus and planar density of unit cell, super cells (2×2×2), and symmetry cells of cubic crystal lattices, such as sodium chloride (NaCl) and Perovskite ($CaTiO_3$).
4)Evaluation of stress-strain of unit cell and super cells (2×2×2) of HA as hexagonal lattice and W–H method in uniform stress deformation model (USDM) that derived from the X-ray diffraction.
5)Preparation of a new bioactive nanocomposite composed of Ag-doped HA and polyvinyl-trimethoxysilane (PVTMS) and investigation of the mechanical properties and in vitro bioactivity of nanocomposite Ag-doped HA/PVTMS.
6)Evaluation of the effect of calcination temperature on the mechanical properties of a new nanocomposite, consisting of HA/copper iodide (CuI).

Research methods and equipment

First, the natural bones of cow, pig, and chicken were boiled in hot water for two hours to eliminate meats and fats on the surface of the bones. Then, the bones were cleaned and dried at 110 °C for two hours. Finally, thermal treatment of hydroxyapatite was performed in a furnace at 950 °C for two hours to allow diffusion of proteins, such as collagens, from inside of the bones to the surface, and burning at high temperatures. The model of the furnace was E5CK-AA1-302 (Snol 6.7/1300). In this study, a Bruker D8 ADVANCE X-ray diffractometer with $Cu_{K\alpha}$ radiation was used. A white and clean hydroxyapatite was obtained. The product was grinded in a rotary ball mill with some volume ratios of fired grogs, steel balls, and empty space. The model of ball mill was planetary Fritsch Pulverisette-5. The particle sizes were micron scale, while the crystal sizes inside the particles were nano size, as it is known in literature. The powder X-ray diffraction was taken at 40 kV and 40 mA and recorded from 20 to 50 degrees for 2θ at a scanning speed of 2.5 degrees/minute and a step size of 0.02 degrees. The resulting patterns were studied by High Score X'Pert software analysis, which uses the fundamental parameter procedure implemented in ASC suffix files. In addition, the specific surface area of samples was measured by desorption isotherms of nitrogen (N_2) gas by using Brunauer Emmett Teller (BET) apparatus Gemini V analyzer, micrometrics GmbH, Germany. For thin layers of samples, the transmission electron microscopy (TEM) CM 10-Philips with acceleration voltage between 50–80 KV was used. A pulse echo method was used for the measurement of sound velocity for both transverse and longitudinal ultrasonic waves, and a specimen with a thickness of ~2 cm was fabricated. The model pulser receiver was Panametrics Co. (Waltham), and the oscilloscope was an Iwatsu model (100 MHz). The resonant frequencies were considered as 10 and 5 MHz for the longitudinal and transverse waves, respectively. Furthermore, the three-dimensional (3D) geometry of crystal structures was designed by Crystal Maker, Version 10.2.2 software. In addition, for investigating the mechanical properties, SANTAM STM-50 and H-25KT were used; additionally, the samples were prepared according to the ASTM-E9 standard. Moreover, for

measuring hardness, the model of device LECO M-400 was used, and the ASTM-E384 standard was considered. Electronic speckle pattern interferometry (ESPI) system PRISM (MM-SIC, high tech) and PRISM VIZ (DAQ-Version 1.2.0) software were utilized for investigating the imperfections on the surface of specimens.

Statements for the defence

1. The crystallite size can be calculated by X-ray diffraction and the modified Scherrer equation with high accuracy.
2. Young's modulus has a relationship with planar density directly.
3. Young's modulus values can be calculated by X-ray diffraction and least squares method with high accuracy.
4. NaCl, $CaTiO_3$, and HA are examples of calculation of Young's modulus using X-ray diffraction and least squares method in this dissertation.
5. A new approach to create porosities >100 microns and improve the mechanical properties of the composites composed of HA /Ag/PVTMS is presented.
6. The effect of calcination temperatures on the mechanical properties of new composites composed of HA /CuI is investigated.

Scientific novelty

The novelty of this work is to present and compare all methods for calculating the size of nanocrystals by X-ray diffraction and introduce a new method with high accuracy. Furthermore, a new technique is introduced to obtain the Young's modulus, corresponding to any crystallite lattice, such as the cubic and/or hexagonal lattice. In addition, the preparation and investigation of bioactivity and mechanical properties of a new nanocomposite consisting of Ag-doped HA and polyvinyltrimethoxysilane (PVTMS) are presented. Moreover, the preparation and evaluation of the effects of calcination temperatures on the mechanical properties of a new nanocomposite, consisting of HA/copper iodide (CuI) are presented in detail below.

1)Natural, artificial HA, scaffold containing Ag-doped HA and PVTMS as reinforcement, and composites containing HA as matrix doped with copper iodide (5 mol%) as reinforcement were synthesized and characterized.
2)X-ray diffraction and the relationship between Young's modulus and planar density can be used to measure the size of nanocrystals and their mechanical properties with high accuracy.
3)The new technique for measuring mechanical parameters using X-ray diffraction was confirmed by ultrasonic pulse-echo test.
4)The mechanical properties based on the new technique for measuring the Young's modulus of NaCl and $CaTiO_3$, as an example of cubic lattice, and HA, as an example of hexagonal lattice, were studied.
5)As a novelty, the hair band was used as a scaffold for the creation of porosities, since porosities are the best places for the nucleation and growth of blood cells.

6)A new bioactive Ag-doped HA + PVTMS composite was prepared where HA played the role of a matrix and Ag and PVTMS were reinforcements.
7)The mechanical properties of copper iodide (5 mol%) doped HA was investigated, and it has been shown that the mechanical properties can be improved when the calcination temperature is increased (900 °C).

Practical significance

1. To develop and explore a new method of calculating the crystallite size by affordable methods, such as X-ray diffraction;
2. To develop mechanical properties and discuss the relationship between Young's modulus and planar density in detail;
3. Low firing point of pieces, such as hair bands, can be used to create porosity without collapse;
4. Increasing the calcination temperature to the optimum point can improve the mechanical properties of HA/CuI composite.

Research approbation

The research results presented in the dissertation have been published in various journals and conferences: six articles in "Web of Science" indexed international journals with high impact: *Nanomaterials* IF: 5.076; Q1; *Materials* IF: 3.623; Q1; *Polymers* IF: 4.329; Q1; *Optical materials* IF: 3.080; Q2.

The results were presented at the following international conferences:
1. 2nd International Research Workshop in Biomechanical Microsystems, Kaunas University of Technology, Kaunas, Lithuania.
2. 22nd International Conference-School, Advanced Materials and Technologies, Palanga, Lithuania.
3. 8th International Conference on Mechanical, Construction, Industrial and Civil Engineering, Istanbul, Turkey.
4. 4th Conference on Technology Development in Mechanical and Aerospace Engineering, Tehran, Iran.
5. 23rd International Conference-School, Advanced Materials and Technologies, Palanga, Lithuania.
6. 15th International Conference Mechatronic Systems and Materials, Białystok, Poland.
7. International Research Workshop in Biomechanical Microsystems, Kaunas University of Technology, Kaunas, Lithuania.

Personal input of the author

The author investigated the mechanical and physical properties in six series of studies. The author synthesized, prepared, designed, analyzed, and used software, evaluated, developed a new methodology, curated data, and investigated all measurements on techniques and nanocomposites. The author wrote the original draft of all articles, being the first author of 5 articles and the third author of the last article. In addition, the author was a corresponding author in two articles. Prof. Ahmad Monshi (Department of Materials Engineering, Isfahan University of

Technology) analyzed the XRD pattern and planar density. The measurements of the ultrasonic pulse-echo test and X-ray diffraction were done by Sr. Sohrab Nasiri (Department of Mechanical Engineering and Design, Kaunas University of Technology). Dr. Andrius Vilkauskas (Institute of Mechatronics, Kaunas University of Technology) performed the methodology and processing. The theoretical calculations were performed in collaboration with Mr. Amir Dashti (Department of Materials Science and Engineering, Sharif University of Technology) and Ms. Akram Doustmohammadi (Materials and Energy Research Center (MERC), Meshkin-Dasht, Karaj). The investigation of chemical methods and synthesis routes of the composites was carried out by Prof. Reza Ebrahimi-Kahrizsangi (Department of Materials Engineering, Najafabad Branch, Islamic Azad University of Najafabad). Dr. Mozhgan Hosseinnezhad (Department of Organic Colorants, Institute for Color Science and Technology) evaluated the sol–gel method. Eventually, the X-ray diffraction analysis, Fourier-transform infrared spectroscopy (FTIR) investigation, and the editing of draft were performed by Prof. Giedrius Janušas (Department of Mechanical Engineering and Design, Kaunas University of Technology).

Structure of the dissertation

This dissertation consists of an introduction, literature review, the main part, which is divided into 6 chapters, conclusions, a list of references and publications.

2.LITERATURE REVIEW

There is a need to replace the bone lost due to the traumatic or non-traumatic events. The lost bone can be replaced by endogenous or exogenous bone tissue, which is associated with various problems. The use of endogenous bone substance is associated with an additional surgical procedure [1]. Moreover, the endogenous bone is only available in limited quantities. The main disadvantage of exogenous bone implants is that they can be rejected by the human body, the diseases can be transmitted with the implant, and the clinical performance of exogenous bone is significantly inferior to fresh endogenous graft material [2]. For these reasons, there is a growing need for the fabrication of artificial hard tissue replacement implants. The biomaterials industry generates $2.3 billion in annual sales worldwide in hard tissue repair and replacement ($12 billion in total) [2]. Currently, biomaterials in clinical applications are projected to grow at the annual rate of 7–12%. Although the biomaterials sector is expanding, the volume of materials that are required is never expected to exceed tens of tons, in contrast to thousands of tons in other developing technical markets. The metals are used extensively for important weight-bearing orthopedic applications. However, there are several problems associated with metallic materials in the human body due to corrosion, wear, and/or adverse tissue reactions [3]. Almost all metallic implants are encased in dense fibrous tissue, which prevents proper distribution of loads and may lead to loosening of the implant. Therefore, various ceramic materials have been used clinically [4]. Among them, ZrO_2 and Al_2O_3 have high mechanical strength and good biocompatibility, but like metals, they belong to bioinert materials. The types of implant-tissue reaction according to Hench are as follows [4]: if the material is toxic, the surrounding tissue dies; if the material is nontoxic and biologically inactive (bioinert), a fibrous tissue of varying thickness forms; if the material is nontoxic and biologically active (bioactive), an interfacial bond forms. However, calcium phosphates and bioactive glasses exhibit high bioactivity and biocompatibility. Biocompatibility generally refers to the acceptance of the implant at the tissue surface. This broad term as well includes nontoxicity, noncarcinogenity, chemical inertness, and stability of material in the living body. Similar phenomena have been described in several reviews, e.g., [5, 6]. Unfortunately, their mechanical properties are relatively poor, which limits their application to small, unloaded implants, powders, coatings, and low-loaded porous implants [7]. Ti-alloy hip replacements with ceramic (alumina or zirconia) heads are used worldwide. Approximately half a million of such hip replacements have been implanted, and their numbers are increasing by 100,000 annually. However, in the United Kingdom alone, from 40,000 hip replacements performed annually, 18% are revision surgeries [4]. The problems appear due to the loosening of implant because of its bioinertness5 and/or stress concentration due to the higher stiffness of implant compared to the natural bone. Therefore, there is a real need for the development of "second generation" bioactive implants that promote regeneration of the surrounding tissue. Such materials could be used for hip-

replacement prostheses as well as other artificial bones or artificial tooth roots. The clinical success of the implant requires simultaneous achievement of a stable interface with a connective tissue and a match between the mechanical behavior of the implant and the tissue that is being replaced. Suitable hard tissue replacement implants should be bioactive (i.e., establish a chemical bond at the bone-implant interface), have a modulus equivalent to that bone, and even be tougher than bone [8]. In case of trauma, bone should fracture rather than the implant. Unlike bone, the implant would not heal naturally, and it would be very difficult to remove it from the body [8]. Furthermore, if only the requirements for sufficient strength can be met, an ideal implant material should biodegrade over time and be replaced with natural host tissue. The organic components of the bone (mainly collagen) would behave like a compliant material with high toughness, low modulus, and other properties that are characteristic to polymers. Inorganic constituents, i.e., HA crystals, impart adequate stiffness to the bone. As a ceramic-organic composite, the bone exhibits high toughness and relatively high modulus. The high toughness is not only related to the presence of collagen, but to the complicated fibrous microstructure as well. It should be noted that bone is a tough material at low strain rates, but fractures more like a brittle material at high strain rates [9]. Bone exhibits excellent toughness (at low strain rates), mainly due to its hierarchical structure, which stops cracks after only a small amount of propagation. The most important toughness mechanisms appear to be microcracks occurring in the plastic region of the stress-strain curve, crack deflection, and pullout effects [2].

The mechanical properties of bone depend largely on moisture, type of load, direction of load, and kind of bone. As the degree of mineralization of bone increases, the strength increases, and the elongation at fracture decreases. In addition, the strength and other mechanical properties of bone depend on the orientation of the collagen fibers, bone density and porosity, and the molecular structure and arrangement of the apatite crystals that make up the bone within its collagen matrix. Finally, both the strength and volume of human bone decrease dramatically with age [10]. Various techniques have been used for the preparation of HA powders, which have been described in several papers [11, 12, 13, 14]. Two main methods for the preparation of HA powders are wet process and solid state reactions. In the preparation of HA, wet processes [15, 2] can be divided into three groups: precipitation hydrothermal processes [16] and hydrolysis of other calcium phosphates [17]. Depending on the process, materials with different morphology, stoichiometry, and level of crystallinity can be obtained. Solid-state reactions [18] usually give a stoichiometric and well-crystallized product, but require relatively high temperatures and long heat-treatment times. In addition, the sinterability of such powders is usually low. In the case of precipitation, where the temperature does not exceed 100 °C, crystals in the nanometer range can be prepared. They have the form of sheets, needles, rods, or equiaxed particles. Their crystallinity and their Ca/P ratio depend strongly on the conditions of preparation and are in many cases lower than those of well-crystallized stoichiometric hydroxyapatite. The hydrothermal technique usually results in HA materials with a high degree of crystallinity and a

Ca/P ratio close to the stoichiometric value. Their crystal size is in the range of nanometers to millimeters. The hydrolysis of tricalcium phosphate, monetite, brushite, or octacalcium phosphate requires low temperatures (usually below 100 °C) and results in HA needles or sheets with a size of micrometers [19]. Synthetic hydroxyapatite has become one of the most important bone graft substitutes in orthopedics and dentistry in recent decades due to its chemical and biological similarity to the mineral phase of human bone [20]. A remarkable property of synthetic hydroxyapatite is its bioactivity, especially its ability to form a chemical bond with the surrounding hard tissue after implantation, for example, [4, 21]. However, most synthetic apatites are formed by high-temperature processes (e.g., sintering), resulting in a well-crystallized structure that has little or no activity for bioresorption. This is in contrast to nanocrystalline or biocrystalline apatites, which are generally non-stoichiometric and usually have a much higher degree of bioactivity. Recently, the use of sol–gel processes for the synthesis of HA has become an important research goal [22]. The formation and fusion of apatite crystals at low temperatures is the main advantage of the sol–gel process compared to the conventional methods. For example, temperatures of more than 1000 °C are usually required to sinter the fine apatite crystals produced by wet precipitation, while several hundred degrees Celsius less are required for the densification of sol–gel HA [23]. Moreover, sol–gel HA processing usually results in a fine-grained microstructure with a mixture of crystals in the nano- to submicron range, which is better accepted by the host tissue. Recently, a novel water-based sol–gel process for low-temperature HA synthesis was developed using triethyl phosphite and calcium nitrate as P and Ca precursors, respectively [22]. It was has been shown that the apatitic phase can be formed at a temperature as low as 350 °C. When used for coatings, the process results in a dense, fine-grained, firmly adherent apatite film (on a titanium alloy substrate) after consolidation in the air at temperatures <400 °C. A two-step procedure was used for the synthesis of HA, i.e., the phosphite was first hydrolyzed with water for 24 h, and then aqueous nitrate solution was added. In the recent communication by Schrotter et al. [24], the structural changes of the phosphite precursor ($P(OC_2H_5)_3$) were described by observing the analyses during hydrolysis. They indicated that the phosphite immediately reacted with water to form ($HPO(OC_2H_5)_2$) and then formed a mixture of $HPO(OC_2H_5)(OH)$ and $HPO(OH)_2$. It took several days for the hydrolysis reaction to complete, i.e., for $HPO(OH)_2$ to form.

Sol–gel technique has attracted much attention recently due to its well-known inherent advantages to generate glass, glass–ceramic, and ceramics powders. These include homogeneous molecular mixing, low processing temperature, the ability to generate sized particles, the tremendous flexibility to generate nanocrystalline powders, bulk amorphous monolithic solids, and thin films. The sol–gel process is easily applicable to surface coating, and it allows the preparation of high-quality HA thin films on metal substrates [25]. Thus, the sol–gel process can be usefully utilized to synthesize both HA powders and HA films under significantly mild conditions. The versatility of the sol–gel method opens a great opportunity to form thin film

coatings in a rather simple process, an alternative to thermal spraying, which is currently widely used for biomedical applications [26]. The sol–gel product is characterized by nano-size dimension of the primary particles. This small domain is a very important parameter for the improvement of the contact reaction and the stability at the artificial/natural bone interface. Moreover, the high reactivity of the sol–gel powder allows a reduction of processing temperature and any degradation phenomena that are occurring during sintering [22]. The major limitation of the sol–gel technique application is linked to the possible hydrolysis of phosphates and the high cost of raw materials [22]. Both these problems were solved in the proposed method of the present paper. However, most of the sol–gel processes require a strict pH control, vigorous agitation, and a long time for hydrolysis. In this paper, a simple technique to generate the gel by non-alkoxide-based sol–gel approach, using inexpensive precursors, has been described. More importantly, gel formation has been achieved without using any catalyst. The sol–gel approach provides significantly milder conditions for the synthesis of HA films. This results in a much better structural integrity, whereas the defects that originated from the plasma spraying can be largely avoided [27]. Furthermore, the lower temperature synthesis particularly benefits the metal substrates where the mechanical degradation or phase transition of the underlying Ti or Ti alloy (i.e., α→β phase transition, occurring at 883 and 960 °C, respectively) can be prevented. However, thermal treatment of HA sol–gel films under vacuum environment is frequently required to avoid metal oxidation. This leads to structural instability of the HA coating (i.e., evolution of structural water under vacuum environment) during thermal treatment. Therefore, from both economic and practical points of view, thermal treatment of the HA coating should be performed in the air and below the transition temperature of the substrate. In order to minimize oxidation of the underlying substrate, thermal treatment temperature should be selected at the minimum level, which still assures sufficient quality of HA film, in terms of crystallinity, film integrity, and adhesion to the substrate. At temperatures below ~500 °C, the oxidation of the underlying Ti or Ti alloy is negligible due to the presence of a natural, dense oxide layer on commercial titanium implants [28]. Therefore, the primary focus of this preliminary study is a search for a sol–gel process that leads to a high-quality HA coating after the heat treatment at temperatures below 500 °C.

HA occurs in the form of nanocrystals with dimensions of about 4 × 50 × 50 nm. The minerals are indirectly bound to collagen via non-collagenous proteins, such as osteocalcin, osteopontin, or osteonectin, which constitute about 3–5% of bone and represent active sites for biomineralization as well as cell attachment [29]. Natural HA and synthetic HA may differ in their chemical composition and behavior. In contrast, human bones do not have a pure or stoichiometric HA. Human bones contain other ions, mainly CO_3^{2-} and traces of Na^+, Mg^{2+}, Fe^{2+}, Cl^-, F^-. The molar ratio of Ca/P in bones is less than 1.67, compared with a molar ratio of Ca/P in synthetic HA [30]. Calcium deficiency HA is of greater biological interest, because the mineral fraction of hard tissue consists primarily of carbonate-substituted calcium deficiency HA [31] with a Ca/P ratio of about 1.5, which is

chemically and compositionally similar to tricalcium phosphate but structurally similar to stoichiometric hydroxyapatite [32]. Bone-related diseases derive from skeletal diseases, infections, trauma, which can lead to permanent damage to many patients and make the treatment of bone-related disease a clinical challenge [33]. Commonly used bone repair materials mainly include polymeric materials, inorganic materials, metals and their composites [34]. Among polymeric materials, poly (lactic acid) (PLA) [35], polycaprolactone (PCL) [36], poly(lactide-co-glycolide) (PLGA) [37], poly(l-lactic acid) (PLLA) [38], and their composites have attracted much attention because of their excellent biodegradability and biocompatibility. These polymers are not toxic to human body and approved by the U.S. Food and Drug Administration (FDA). They can degrade within body gradually with no residue, no stimulation, and no toxic side effects on the tissues. Moreover, by adjusting the molecular weight and choosing different polymerization and molding processes, the degradation rate and mechanical properties of these biodegradable polymers can be controlled and adapted to different clinical requirements. However, there are some polymers that have the disadvantage of low mechanical strength, no biological activity, and the degraded acid products are not conducive to cell and tissue growth [33]. In order to solve the above mentioned problems, the addition of bioceramic components to polyester can greatly improve its mechanical strength and bioactivity and regulate the acidic microenvironment, created by the acidic degradation products of polyesters, to induce bone formation and prevent inflammatory reactions [39]. In recent years, the effect of various additives on HA coatings to improve compactness, purity, homogeneity, and adhesion to the substrate has been intensively researched. Zhiwei Zhou et al. prepared a polydopamine/HA hybrid coating on AZ31 Mg alloy with a hydrothermal process [40]. They prepared a thick and dense coating using polydopamine as the inner layer and hydroxyapatite as the outer layer. Polydopamine enhanced the corrosion protection properties due to its catechol functional groups, binding to metal ions, and absorption of Ca^{2+} ions. Zomorodian et al. studied the corrosion and cell proliferation properties of a composite coating consisting of a polycaprolactone matrix modified with nano HA and applied to AZ31-Mg alloys [41]. The magnesium alloy was pretreated with hydrofluoric acid, and since the polycaprolactone does not adhere to the Mg substrate, a thin inner layer of polyetherimide was applied to the Mg surface as an adhesion promoter.

Taking into account the existence of Calcium Phosphates (CaPs) in the body, nowadays, the researchers have considered CaPs for the replacement and repair of injured bones. One of the most desirable and well-known CaPs groups is associated with hydroxyapatite (HA) [42, 43]. One of the main characteristics of the HA structure is the ability of a large number of substitutions, which does not change the basis of the crystallographic structure. Fig. 2.1 shows a sketch of a unit cell of hexagonal HA and a cif file of synthesized HA through heat treatment method. There are two different situations of calcium ions, and in total, 18 ions are closely packed to create the hexagonal structure. At each hexagonal corner, a calcium ion is restricted by 12 calcium ions shared with 3 hexagons. Void spaces between two

hexagons are filled with three phosphates tetrahedral per unit cell. Ions in HA can be interchangeably replaced with biologically useful ions due to the inherent versatility of this crystal structure and can be referred to as doping. In addition, the substitution of calcium, phosphate, and/or hydroxyl ions is possible [44]. Notably, the specific feature of HA is related to the OH^- ions forming inner channels along the c axis. This property plays an important role in mechanical and physical properties [45].

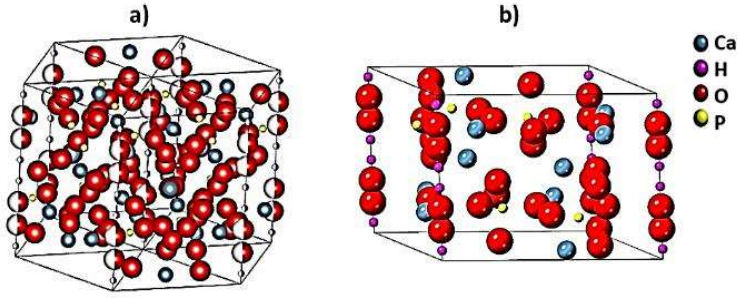

Fig. 2.1. Schematic representation of (a) HA unit cell and (b) HA structure extracted by cif file [8]

One of the challenges for using HA as a bioactive component is related to the likelihood of infection; therefore, the use of antibacterial materials is the best way to solve this problem [46]. However, the studies have proven that silver (Ag) has antibacterial properties [47, 48]. Moreover, one of the best elements for biocompatibility is Ag, since it is related to the high value of the antibacterial coefficient (100%) [49, 50]. However, the biocompatibility properties of Ag are directly dependent on the strength, density, and the manufactured final phase of bioactive composites. There are several mechanisms that involve Ag in the interaction with biological macromolecules [51]. In addition, the Ag^+ has been shown to bind to protein functional groups, leading to protein denaturation [52].

Polyvinyltrimethoxysilane (PVTMS) has a functional group like silanol (Si-O-H), which can help in bonding; therefore, it is useful for preventing the decomposition of composites [53]. PVTMS is a type of component-based on polysiloxane that is of particular interest due to its dense structure of siloxane cross-linked with polymeric groups; in addition, PVTMS is bioactive and enhances mechanical properties by providing a stable Si-O-Si framework [54].

The research on copper iodide (CuI) is very interesting, because it has several advantages, such as a wide large band gap, photosensitivity, diamagnetism behavior, as a dye in solar cells, and superionic conductor [55, 56]. Several metals, e.g., Ag^+, Sr^{2+}, Mn^{2+}, and Fe^{3+}, with different weight percentages have been used for doping in HA by different methods, and the evaluations of properties have been brought in [57, 58, 59, 60]. Moreover, the Cu^{2+}-doped HA was prepared by the sol–gel method in the research of Renaudin et al. [61]. According to the experimental observations, it was undeniable that the Cu^{2+}-doped HA structure leads to bonding, and Cu^{2+} cations are placed along the crystallographic hydroxyl sites through the formation of linear O-Cu-O units. Subsequent studies involving copper have shown significant similarities and revealed specific behaviors. Moreover, a higher doping level can be

achieved with a reduction of Cu^{2+} to Cu^{+}, but this requires a higher sintering temperature [62, 63, 64].

Uwe Holzwarth and Neil Gibson announced that the Scherrer equation is related to a sharp peak of X-ray diffraction. The equation was introduced with the subscript (hkl), because it is related to the one peak only. It is important to note that the Scherrer equation can only be utilized for average sizes up to around 100 nm. It depends on the instrument as well as the relationship between signal and sample to criterion noise, because when the crystallite size increases, the diffraction peak broadening decreases. It can be very hard to provide separation and distinguishing of broadening through the crystallite size from the broadening due to the other parameters and factors. The errors exist always, and successful calculation methods are those that can decrease the errors in the best possible way to yield more accurate data. The calculation of nanoparticle size extracted by the XRD patterns is not possible because a particle has several nanoscale or microscale crystals. An X-ray can penetrate through the crystal size to provide information; therefore, the calculation of size is not related to the particles and is related to the crystals. The Scherrer equation relates to the diffraction peak submitted in Equation 2.1 [65], where L is the nanocrystal size, K is the shape factor, usually taken as 0.89 for ceramic materials, λ is the wavelength of radiation in nanometer ($\lambda_{CuK\alpha}$= 0.15405 nm), Θ is the diffracted angle of the pea, β is the full width at half maximum (FWHM) of the peak in radians. In addition, the broadening in peaks is related to the physical broadening and instrumental broadening [66, 67].

$$L = \frac{K\lambda}{\beta}.\frac{1}{\cos\theta} \text{ [67].} \quad (2.1)$$

In order to decrease this error of the instrument, Equation 2.2 can be used:

$$\beta_d^2 = \beta_m^2 - \beta_i^2 \text{ [67].} \quad (2.2)$$

In this formula, β_m is the measured broadening, β_i is the instrumental broadening, and β_d is introduced as the corrected broadening responsible for the crystal size. The instrumental broadening and the physical broadening of the sample measured via the full width at half maximum (FWHM) and the correction of the physical broadening allow the crystal size to be calculated with the Scherrer equation as described in Ref [68, 69]. There are several publications that used the calculation of Scherrer equation for the sharpest peak only, and they were not considering the calculations of all peaks.

Hooke's law is shown in Equation 2.3: the stress corresponds to the strain for small displacements. It is the basic form that this symmetry can be converted to the six items of σ and ε [70].

$$\begin{pmatrix}\sigma_{xx}\\ \sigma_{yy}\\ \sigma_{zz}\\ \sigma_{yz}\\ \sigma_{zx}\\ \sigma_{xy}\end{pmatrix}=\begin{pmatrix}c_{11}\,c_{12}\,c_{13}\,c_{14}\,c_{15}\,c_{16}\\ c_{21}\,c_{22}\,c_{23}\,c_{24}\,c_{25}\,c_{26}\\ C_{31}C_{32}C_{33}C_{34}C_{35}C_{36}\\ C_{41}C_{42}C_{43}C_{44}C_{45}C_{46}\\ C_{51}C_{52}C_{53}C_{54}C_{55}C_{56}\\ C_{61}C_{62}C_{63}C_{64}C_{65}C_{66}\end{pmatrix}=\begin{pmatrix}\varepsilon_{xx}\\ \varepsilon_{yy}\\ \varepsilon_{zz}\\ \varepsilon_{yz}\\ \varepsilon_{zx}\\ \varepsilon_{xy}\end{pmatrix} \quad (2.3)$$

Additionally, Hooke's law can be written as (Equation (2.4)):

$$\begin{aligned}\sigma_{xx} &= C_{11}\varepsilon_{xx}+C_{12}\varepsilon_{yy}+C_{13}\varepsilon_{zz}+C_{14}\varepsilon_{yz}+C_{15}\varepsilon_{zx}+C_{16}\varepsilon_{xy}\\ \sigma_{yy} &= C_{21}\varepsilon_{xx}+C_{22}\varepsilon_{yy}+C_{23}\varepsilon_{zz}+C_{24}\varepsilon_{yz}+C_{25}\varepsilon_{zx}+C_{26}\varepsilon_{xy}\\ \sigma_{zz} &= C_{31}\varepsilon_{xx}+C_{32}\varepsilon_{yy}+C_{33}\varepsilon_{zz}+C_{34}\varepsilon_{yz}+C_{35}\varepsilon_{zx}+C_{36}\\ \sigma_{yz} &= C_{41}\varepsilon_{xx}+C_{42}\varepsilon_{yy}+C_{43}\varepsilon_{zz}+C_{44}\varepsilon_{yz}+C_{45}\varepsilon_{zx}+C_{46}\varepsilon_{xy}\\ \sigma_{zx} &= C_{51}\varepsilon_{xx}+C_{52}\varepsilon_{yy}+C_{53}\varepsilon_{zz}+C_{54}\varepsilon_{yz}+C_{55}\varepsilon_{zx}+C_{56}\varepsilon_{xy}\\ \sigma_{xy} &= C_{61}\varepsilon_{xx}+C_{62}\varepsilon_{yy}+C_{63}\varepsilon_{zz}+C_{64}\varepsilon_{yz}+C_{65}\varepsilon_{zx}+C_{66}\varepsilon_{xy}.\end{aligned} \quad (2.4)$$

The elastic stiffness determines the response of crystal to an externally applied stress or strain and provides information about the bonding characteristics, mechanical and structural stability [71]. The HA system has five elastic constants (Equation (2.5)). Therefore, the values of five independent (elastic stiffness constant C_{ij}), can be named C_{11}, C_{12}, C_{13}, C_{33}, C_{44}.

Hydroxyapatite matrix $$\begin{vmatrix}C_{11} & C_{12} & C_{13} & 0 & 0 & 0\\ C_{12} & C_{11} & C_{13} & 0 & 0 & 0\\ C_{13} & C_{13} & C_{33} & 0 & 0 & 0\\ 0 & 0 & 0 & C_{44} & 0 & 0\\ 0 & 0 & 0 & 0 & C_{44} & 0\\ 0 & 0 & 0 & 0 & 0 & \frac{1}{2}(C_{11}-C_{12})\end{vmatrix} \quad (2.5)$$

For conventional hexagonal systems, such as HA, the relationship between C_{ij} and elastic compliances S_{ij} is introduced in Equations (2.6–2.16) [72, 72].

$$S_{11}=\frac{1}{2}\left(\frac{C_{33}}{C_{33}(C_{11}+C_{12})-2(C_{13})^2}+\frac{1}{C_{11}-C_{12}}\right) \quad (2.6)$$

$$S_{12}=\frac{1}{2}\left(\frac{C_{33}}{C_{33}(C_{11}+C_{12})-2(C_{13})^2}-\frac{1}{C_{11}-C_{12}}\right) \quad (2.7)$$

$$S_{33} = \frac{C_{11} + C_{12}}{C_{33}(C_{11} + C_{12}) - 2(C_{13})^2} \tag{2.8}$$

$$S_{13} = -\frac{C_{13}}{C_{33}(C_{11} + C_{12}) - 2(C_{13})^2} \tag{2.9}$$

$$S_{44} = \frac{1}{C_{44}} \tag{2.10}$$

According to the Equations (2.6–2.10), in order to obtain S values, C values are needed. The complete set of five values: C_{11}, C_{12}, C_{13}, C_{33}, and C_{44} of samples, was found from ultrasonic measurements of the phase velocity anisotropy. In these equations, ρ and V are the density of the sample and velocity [73, 74, 75].

$$C_{11} = \rho V_{1/1}^2,\ C_{22} = \rho V_{2/2}^2 \tag{2.11}$$

$$C_{66} = \rho V_{1/2}^2 = \rho V_{2/1}^2,\ C_{55} = \rho V_{1/3}^2 = \rho V_{3/1}^2 \tag{2.12}$$

$$C_{12} = \sqrt{(C_{11} + C_{66} - 2\rho V_{12/12}^2)(C_{22} + C_{66} - 2\rho V_{12/12}^2)} - C_{66} \tag{2.13}$$

$$C_{44} = \rho V_{2/3}^2 = \rho V_{3/2}^2 \tag{2.14}$$

$$C_{13} = \sqrt{(C_{11} + C_{55} - 2\rho V_{13/13}^2)(C_{33} + C_{55} - 2\rho V_{13/13}^2)} - C_{55} \tag{2.15}$$

$$C_{33} = \rho V_{3/3}^2 \tag{2.16}$$

For measuring the velocities, the standard ultrasonic pulse-echo ASTM E797/E797-M-15 was accomplished according to Ref [76]. Accordingly, the shear modulus is proportional to the Burgers vector and the Young's modulus; in addition, dislocation density is in agreement with the Young's modulus [77, 78]. In the ultrasonic method, longitudinal and transverse waves were used for measuring the Young's modulus value [79, 80]. According to this method (Equation (2.17)), based on the velocity of ultrasound waves and density of the sample, the Young's modulus value was determined.

$$E = \frac{\rho c_l^2 [3(\frac{c_l}{c_t})^2 - 4]}{(\frac{c_l}{c_t})^2 - 1} \tag{2.17}$$

In Equation 2.17, ρ, c_l, and c_t are density, velocity of longitudinal and transverse ultrasound waves tandemly. Furthermore, according to Equation 2.18, the velocity of longitudinal and transverse waves can be registered by determining the length of the specimen and the differences between two echoes ($t = t_2 - t_1$) in the signals [81].

$$c = \frac{2L}{t}; \tag{2.18}$$

where, L is the length of the sample, and t is the difference between two echoes, and the density of the sample can be detected by measuring the mass and volume of the sample [36]. Additionally, with the substitution of Equations 2.17 and 2.18, the main equation for the calculation of Young's modulus is introduced as the Equation 2.19 [82].

$$E = \frac{4\rho\left(\frac{L}{t_s}\right)^2 (3t_s^2 - 4t_l^2)}{t_s^2 - t_l^2} \tag{2.19}$$

3. REVIEW OF THE PROVIDED ARTICLES AND DISCUSSION

3.1. Comparing Methods for Calculating Nano Crystal Size of Natural Hydroxyapatite Using X-Ray Diffraction (Scientific Publication No. 1, Q1, 67 Quotations)

This chapter is based on the paper published in *Nanomaterials*, 2020, *10*, 1−21 [83]. 1) Femur bones of cow, pig, and chicken were prepared. First, bovine bones were separated and boiled in hot water and then immersed in acetone for 2 h to remove collagen and fat (step 1, Fig. 3.1). In step 2, the bones were washed with distilled water and dried two times. Then, the bones were placed in separate steps in the furnace under ambient conditions, and the rate of increasing temperature was 10 °C/minute. Finally, the bones were fired at 950 °C for 2 h, and they were cooled in the furnace very slowly. Following this process, the first black fired bones (due to the carbon release) turned into a white granular bulk. Furthermore, the bones were transformed to fully crystallized HA at 950 °C (step 3) [84]. The HA extracted from cow, pig, and chicken bones was placed into a planetary ball mill device involving a bowl (tungsten carbide) and balls to fabricate fine particles after heat-treating. The feed ratio was 30 g powder to 300 g of balls (1 to 10 weight ratio), the speed was fixed at 250 rpm, and the milling time was adjusted at 2 h with pause and reverse mode (step 4), according to the procedure described in literature [85, 86]. The images of the production route of HA are presented in Fig. 3.1.

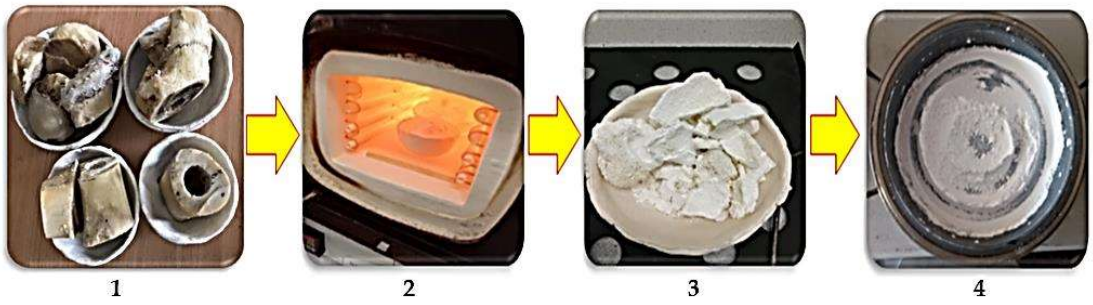

Fig. 3.1. Images of the production route of HA obtained from cow, pig, and chicken bones (steps 1–4)

The phase composition and purity of the materials were determined by X-ray diffraction. The XRD patterns of the HA white powder produced after milling are presented in Fig. 3.2. The XRD patterns were investigated completely through the X'Pert software, and the patterns were confirmed via standard XRD peaks of HA based on ICDD 9-432. Similar observations have been reported by Bahrololoom and Shahabi [87, 88]. In addition, crystallographic parameters of each individual XRD pattern are presented in Table 3.1, respectively. Moreover, crystallographic parameters related to the structures resulting from X'Pert software analysis could be seen in Table 3.2. The unit cell parameters were in good agreement with the results by other researchers for the fabrication of HA [89, 44].

According to the XRD patterns (Fig. 3.2), it has been observed that the crystallization of HA samples was nearly similar. The pattern of XRD is shown at angles between $20° < 2\theta < 50°$. The largest peaks have been observed, corresponding to crystalline HA, at around 31.96°, 32.04°, and 32.03° for cow, pig, and chicken, respectively. Based on the pattern, the strong diffraction peaks at 2θ values are attributed to the HA structure, whose hkl values of exact HA peaks are related to 002, 102, 210, 211, 112, 300, and 202, respectively [90]. In addition, the values of FWHM of the peaks (β) in radians were recorded in the range from 0.00174 to 0.00348, 0.00226 to 0.00313, and 0.00244 to 0.00313 for HA obtained from cow, pig, and chicken bones, respectively (Table 3.1). Furthermore, the maximum intensity of samples was not different, and the count was in the range of ~250 counts. The reason is related to the same generation and nature of the HA samples.

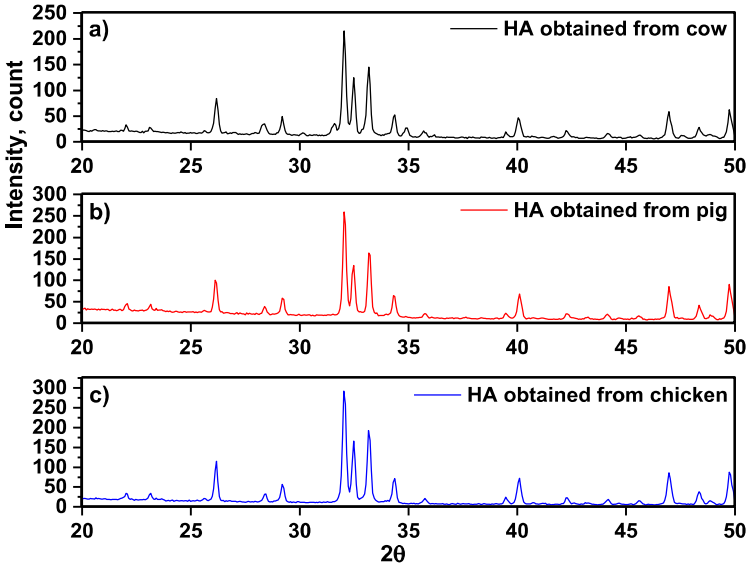

Fig. 3.2. XRD patterns of HA obtained from (a) cow, (b) pig, and (c) chicken bones

Table 3.1. Crystallographic parameters of the XRD pattern related to the hydroxyapatite obtained from cow

Cow												
2θ (Degree)	β = FWHM (Degree)	Θ (Degree)	cosΘ (Degree)	1/cosΘ (Degree)	Ln(1/cosΘ) (Degree)	β = FWHM (Radian)	Ln β (Radian)	4 sinΘ (Degree)	β(Radian).cosΘ (Degree)	hkl	d_{hkl} (Å)
26.15	0.14	13.07	0.9740	1.02669	0.02634	0.00244	−6.0174	0.9045	0.00238	002	3.46500
28.32	0.2	14.16	0.9696	1.03135	0.03087	0.00348	−5.66072	0.9785	0.00337	102	3.17485
29.18	0.1	14.59	0.9677	1.03338	0.03283	0.00174	−6.35387	1.007	0.00168	210	3.07687
31.96	0.15	15.98	0.9613	1.04026	0.03947	0.00261	−5.94841	1.1012	0.00251	211	2.81215
32.54	0.14	16.27	0.9599	1.04178	0.04093	0.00244	−6.0174	1.1206	0.00234	112	2.78900
32.98	0.15	16.49	0.9588	1.04297	0.04207	0.00261	−5.94841	1.1353	0.0025	300	2.71354
33.97	0.14	16.98	0.9564	1.04559	0.04458	0.00244	−6.0174	1.1681	0.00233	202	2.63845
40.03	0.15	20.01	0.9396	1.06428	0.0623	0.00261	−5.94841	1.3687	0.00245	310	2.26285
46.94	0.16	23.47	0.9172	1.09027	0.08643	0.00278	−5.88387	1.5930	0.00255	222	1.94339
48.35	0.2	24.17	0.9123	1.09613	0.09179	0.00348	−5.66072	1.6377	0.00317	320	1.87176
49.73	0.15	24.86	0.9073	1.10217	0.09728	0.00261	−5.94841	1.6816	0.00237	213	1.84732

Pig											
2θ (Degree)	β = FWHM (Degree)	Θ (Degree)	cosΘ (Degree)	1/cosΘ (Degree)	Ln(1/cosΘ) (Degree)	β = FWHM (Radian)	Ln β (Radian)	4 sinΘ (Degree)	β(Radian).cosΘ (Degree)	hkl	d_{hkl} (Å)
26.12	0.13	13.06	0.9741	1.02659	0.02624	0.00226	−6.09151	0.9038	0.0022	002	3.46500
29.20	0.14	14.60	0.9677	1.03338	0.03283	0.00244	−6.0174	1.0082	0.00236	210	3.07687
32.04	0.14	16.02	0.9611	1.04047	0.03968	0.00244	−6.0174	1.1038	0.00235	211	2.81215
32.44	0.13	16.22	0.9601	1.04156	0.04072	0.00226	−6.09151	1.1173	0.00217	112	2.78900
33.07	0.14	16.53	0.9586	1.04319	0.04228	0.00244	−6.0174	1.1380	0.00234	300	2.71354
34.02	0.14	17.01	0.9562	1.04581	0.04479	0.00244	−6.0174	1.1701	0.00233	202	2.63845
40.07	0.18	20.03	0.9395	1.0644	0.06241	0.00313	−5.76608	1.3700	0.00294	310	2.26285
46.96	0.15	23.48	0.9171	1.09039	0.08654	0.00261	−5.94841	1.5937	0.00239	222	1.94339
48.34	0.14	24.17	0.9123	1.09613	0.09179	0.00244	−6.0174	1.6377	0.00223	320	1.87176
49.73	0.15	24.86	0.9073	1.10217	0.09728	0.00261	−5.94841	1.6816	0.00237	213	1.84732

Chicken											
2θ (Degree)	β = FWHM (Degree)	Θ (Degree)	cosΘ (Degree)	1/cosΘ (Degree)	Ln(1/cosΘ) (Degree)	β = FWHM (Radian)	Ln β (Radian)	4 sinΘ (Degree)	β(Radian).cosΘ (Degree)	hkl	d_{hkl} (Å)
26.20	0.14	13.10	0.9739	1.0268	0.02645	0.00244	−6.0174	0.9066	0.00238	002	3.46500
28.39	0.16	14.19	0.9694	1.03157	0.03108	0.00278	−5.88387	0.9805	0.00269	102	3.17485
29.19	0.15	14.59	0.9677	1.03338	0.03283	0.00261	−5.94841	1.0076	0.00253	210	3.07687
32.03	0.16	16.01	0.9612	1.04037	0.03957	0.00278	−5.88387	1.1032	0.00267	211	2.81215
32.45	0.15	16.22	0.9601	1.04156	0.04072	0.00261	−5.94841	1.1173	0.00251	112	2.78900
33.16	0.15	16.58	0.9584	1.04341	0.04249	0.00261	−5.94841	1.1414	0.0025	300	2.71354
34.21	0.16	17.10	0.9557	1.04635	0.04531	0.00278	−5.88387	1.1761	0.00266	202	2.63845
40.05	0.17	20.02	0.9395	1.0644	0.06241	0.00296	−5.82324	1.3693	0.00278	310	2.26285
46.95	0.18	23.47	0.9172	1.09027	0.08643	0.00313	−5.76608	1.5930	0.00287	222	1.94339
48.34	0.17	24.17	0.9123	1.09613	0.09179	0.00296	−5.82324	1.6377	0.0027	320	1.87176
49.74	0.18	24.87	0.9072	1.10229	0.09739	0.00313	−5.76608	1.6822	0.00284	213	1.84732

Table 3.2. Crystallographic parameters related to the HA structure resulting via X'Pert software

Bone	Crystal System	a (Å)	c (Å)	c/a (Å)	Cell Volume ($Å^3$)	Crystal Density (g/cm^3)
Cow	Hexagonal	9.4000	6.9300	0.7340	530.30	3.14
Pig	Hexagonal	9.4210	6.8930	0.7316	529.83	3.14
Chicken	Hexagonal	9.4210	6.8800	0.7302	528.83	3.18

The Scherrer equation (Equation 3.1) systematically shows increased values of nanocrystallite size as the distance of diffracted planes (d) values decreases and 2θ values increase, since β.cosθ cannot be maintained as constant. Furthermore, the modified Scherrer equation can provide advantages when decreasing the errors or $\Sigma\,(\pm\Delta \ln\beta)^2$ to give a more accurate value of L from all or some of the different peaks [91].

$$\text{Ln}\ \beta = \text{Ln}\ (\frac{K\lambda}{L}) + \text{Ln}\ (\frac{1}{\text{Cos}\,\theta}) \tag{3.1}$$

Thus, the linear plot of Ln β (β in radians) versus Ln $(\frac{1}{\text{Cos}\,\theta})$ (degree) can be a linear plot for all or some of the chosen peaks; the least squares statistical method is used to decrease the sources of errors. After establishing the most accurate linear plot, the value of Ln $(\frac{K\lambda}{L})$ can be obtained from the intercept. The $e^{(\text{intercept})}$ gives $\frac{K\lambda}{L}$, from which a single value of L is obtained from all of the available peaks. Lnβ versus ln(1/cosΘ) is demonstrated in the plots of Fig. 3.3 together with the equations of the linear least squares method, obtained from the linear regression of data in the plots. According to the Monshi–Scherrer equation, in order to find the size of the crystals, Equation 3.2 is employed. When using X'Pert software, it is better for making and using the ASC file of peaks data (with suffix ASC) and obtain the peak list, including FWHM, which is related to the fit profile icon (right click on the peak and select fit profile in X'Pert software) to create a full fitting in finding β (FWHM).

$$\frac{K\lambda}{L} = e^{(\text{intercept})} \tag{3.2}$$

Linear equations of HA obtained from cow, pig, and chicken recorded y = 2.7055x − 6.0921, y = 1.5815x − 6.0826, and y = 2.7184x − 6.0285, respectively, and intercept values were −6.0921 for cow, −6.0826 for pig, and −6.0285 for chicken tandemly. Nevertheless, the intercepts were calculated as $e^{(-6.0921)} = 0.00227$, $e^{(-6.0826)} = 0.00228$, and $e^{(-6.0285)} = 0.00240$, respectively. Therefore, $\frac{K\lambda}{L} = 0.00227$, $\frac{K\lambda}{L} = 0.00228$, and $\frac{K\lambda}{L} = 0.00240$ for cow, pig, and chicken tandemly. After the calculations, the values of crystal sizes were obtained equal to 60, 60, and 57 nm for cow, pig, and chicken, respectively.

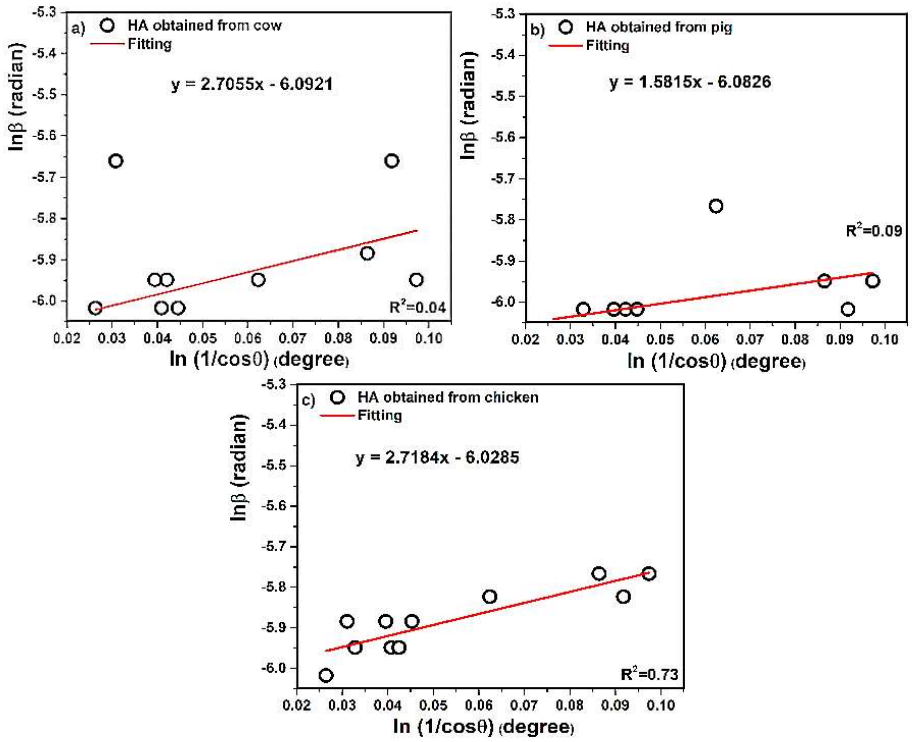

Fig. 3.3. Linear plots of the modified Scherrer equation and gained intercepts for different HA obtained from (a) cow, (b) pig, and (c) chicken bones

Monshi–Scherrer is the only method according to the methods employed in this research that provides a checkpoint for the evaluation of the validity of results. The linear plot must have a slope of one. Therefore, if it deviates from one, some of the points can be eliminated. In this study, the points for all of the methods were kept the same for the proper comparison between methods. However, when using the Monshi–Scherrer method, the elimination of some peaks is advisable to get a slope nearer to one. This decreases sources of errors and gives a more accurate crystal size. This checkpoint can only be assessed in this method. In all other methods, the results should be accepted without any judgement on the validity of the obtained data.

The most widely used technique for estimating a specific surface area is the brunauer-emmett-teller (BET) method. Under normal atmospheric pressure and at the boiling temperature of liquid nitrogen, the amount of nitrogen adsorbed in relationship with pressure gives specific surface area of the powder. The observations are interpreted following the model of BET method. The samples were degassed at 200 °C under reduced pressure (13×10^{-7} atmosphere) for around 15 to 20 h before each measurement. The reported surface area for a bone-derived HA is much lower, and the value is around 0.1 m^2/g [71]. However, one synthetic HA (not sintered or deproteinized bone) is 17 to 82 m^2/g [72]. The theoretical particle size can be calculated from the adsorption specific surface area data by using Equation 3.3.

$$D = \frac{6}{\rho . S} \tag{3.3}$$

In this formula, ρ is the density of the sample, and S refers to the specific surface area of the sample, obtained from the BET method [92]. The BET specific surface area of HA particles that have been obtained from cow, pig, and chicken were 34.36 ± 0.01, 36.95 ± 0.01, and 43.39 ± 0.01 m^2/g. As explained, a theoretical particle size can be calculated from these data, and the values of crystal size for HA calcined at 950 °C obtained from cow, pig, and chicken were 56, 52, and 49 nm, respectively.

Fig. 3.4 shows transmission electron microscopy (TEM) images and stoichiometric composition of HA nanocrystal powders of cow, pig, and chicken bones after the ball milling process. Based on the energy dispersive X-ray spectroscopy (EDX) signatures, the values of ratio Ca/P for HA obtained from cow, pig, and chicken bones were found to be 1.81, 1.79, and 1.68, respectively. A particle may be made of several different crystallites. In addition, the TEM images show agglomerated nanosize of crystals, and it is very clear that the TEM images exhibited the particle size, and between all the particles, there are crystals. TEM size often matches grain size, and in this case, it is apparent that some of the powder particles have nanosized, and the size values are less than 100 nm (width and diameters). One single particle of about 50 nm can be observed clearly in chicken bone in Fig. 3.4 c. Furthermore, the images seem to have an irregular spherical morphology, and such morphologies were cited and confirmed in [75]. The results that have been obtained from the methods and models are summarized in Table 3.3. In general, knowledge of the size of crystals can help to improve the physical and mechanical properties of materials, especially composites.

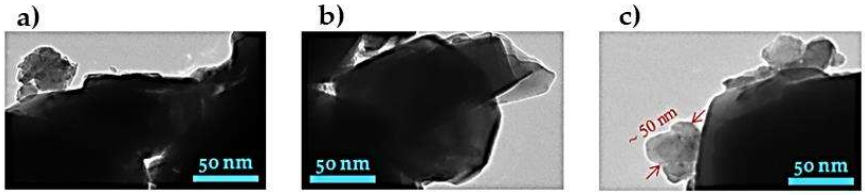

	O (Weight %)	P (Weight %)	Ca (Weight %)	Ca/P
HA obtained from cow bone	17.58	29.33	53.08	1.81
HA obtained from pig bone	19.32	28.94	51.73	1.79
HA obtained from chicken bone	16.87	31.01	52.11	1.68

Fig. 3.4. TEM images and stoichiometric composition of HA nanocrystals obtained from (a) cow, (b) pig, and (c) chicken bones

Table 3.3. Nanosize of HA crystallites obtained from cow, pig, and chicken bones extracted with some calculation methods and experimental methods (BET, TEM) in this study

Size of Crystals	Scherrer (All Peaks/New Model/Average Model)	Monshi–Scherrer	Williamson–Hall (UDM/USDM/UDEDM)	HW	SSP	BET	TEM
L_{cow} (nm)	1371/60/56	60	65/60/62	4	43	56	~50
L_{pig} (nm)	457/60/58	60	62/62/62	4	62	52	~50
$L_{chicken}$ (nm)	196/53/52	57	65/62/65	4	57	49	~50

3.2. Measurement Modulus of Elasticity Related to the Atomic Density of Planes in Unit Cell of Crystal Lattices (Scientific Publication No. 2, Q1, 11 Quotation)

This chapter is based on the paper published in *Journal of Materials,* 2020, 13, 1−17 [93]. This chapter serves as an example of an introduction of a new technique for measuring the Young's modulus for crystallite structures, such as NaCl (FCC).

In this chapter, combining X-ray diffraction of crystallite materials with the planar density of each diffracted plane was performed. It is possible to determine the Young's modulus value of each crystallite solid material accurately. The schematic XRD pattern was chosen for compound x (powder/crystal sample) (Fig. 3.5). These crystallites are assumed to be randomly oriented to one another. In addition, if the powder is placed in the path of a monochromatic X-ray beam, the diffraction will occur from the planes in those crystallites that are oriented at the correct angle to fulfill the Bragg condition. According to Fig. 3.5, five planes consisting of ($h_1 k_1 l_1$), ($h_2 k_2 l_2$), ($h_3 k_3 l_3$), ($h_4 k_4 l_4$), and ($h_5 k_5 l_5$) were diffracted, and the diffracted beams were taken at an angle of 2Θ for each plane with the incident beam. As a result, extracted by the X'Pert software, the lattice parameter (a), index of planes (hkl), and lattice type (seven crystal systems) of compound will be recognized. In order to follow the gaining Young's modulus value with high accuracy, the elastic stiffness constant values (C_{ij}) and elastic compliance values (S_{ij}) are needed.

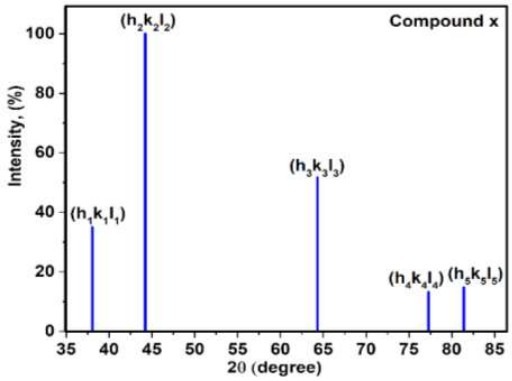

Fig. 3.5. X-ray diffraction of compound x

In most cases, elastic constant values of materials are tabulated in the literature [94, 95]. Furthermore, the Young's modulus of each plane (E_{hkl}) can be expressed for cubic and hexagonal crystals as Equations 3.4 and 3.5, respectively.

For cubic:

$$\frac{1}{E_{hkl}} = S_{11} - 2\left[(S_{11} - S_{12}) - \frac{1}{2}S_{44}\right]\left[\frac{h^2k^2 + k^2l^2 + l^2h^2}{(h^2 + k^2 + l^2)}\right]. \quad (3.4)$$

For hexagonal:

$$E_{hkl} = \frac{\left[h^2 + \frac{(h+2k)^2}{3} + \left(\frac{al}{c}\right)^2\right]^2}{S_{11}\left(h^2 + \frac{(h+2k)^2}{3}\right)^2 + S_{33}\left(\frac{al}{c}\right)^4 + (2S_{13} + S_{44})\left(h^2 + \frac{(h+2k)^2}{3}\right)\left(\frac{al}{c}\right)^2}. \quad (3.5)$$

The type of crystal lattice of compound x must be determined according to the X-ray diffraction file. In this case, it is presumed that compound x has a cubic crystal structure. According to Equations 3.6–3.16, the elastic compliance values of compound x were calculated as S_{11}, S_{12}, and S_{44}; therefore, Young's modulus values of diffracted planes (Fig. 3.6) were registered by Equation 3.4. The values of Young's modulus of diffracted planes of compound x are named as $E_{(h_1k_1l_1)}$, $E_{(h_2k_2l_2)}$, $E_{(h_3k_3l_3)}$, $E_{(h_4k_4l_4)}$ and $E_{(h_5k_5l_5)}$. In addition, the planar density (PD) values of diffracted planes were calculated as $PD_{(h_1k_1l_1)}$, $PD_{(h_2k_2l_2)}$, $PD_{(h_3k_3l_3)}$, $PD_{(h_4k_4l_4)}$, and $PD_{(h_5k_5l_5)}$. Applying the least squares method for the line between the values extracted from Young's modulus and planar density of diffracted planes can give the average Young's modulus value of compound x with high accuracy. In this method, Young's modulus values of diffracted planes play a role as the y axis and the x axis is the planar density. The Young's modules values extracted from each plane of compound x versus the planar density are presented in Fig. 3.6.

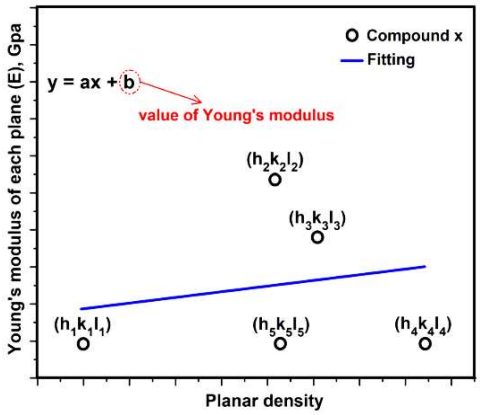

Fig. 3.6. Young's modulus extracted from planes of compound x versus planar density

In this method, the unit of Young's modulus depends on the unit of the elastic stiffness constant and elastic compliance values, and in this case, it is GPa. Moreover, planar density does not always have a unit, and the value of planar

density is always less than 1. Furthermore, the values of the planar density depend on the situation of the planes. For example, in this curve (Fig. 3.6) for compound x, $PD_{(h_4k_4l_4)} > PD_{(h_3k_3l_3)} > PD_{(h_5k_5l_5)} > PD_{(h_2k_2l_2)} > PD_{(h_1k_1l_1)}$. Furthermore, it is possible that two or more planes have similar planar density values.

In this method, the empty planes in one-unit cell are not considered in the calculations. However, if there is no atom in the plane inside the unit cell, they will appear when the plane is extended to the adjacent cells, and the atoms will appear, and the unit cell will be converted to super cells; then, calculating planar density of two or more adjacent unit cells or super cells will be possible.

For example, the X-ray diffraction of sodium chloride (NaCl) is presented in Fig. 3.7. The characterization peaks of NaCl are very close to the corresponding report in [96]. NaCl has ionic bonds and the ionic radius of Na^+ and Cl^- is 0.97 and 1.81 Å, respectively. The crystal of NaCl is FCC, and the location of the atom of Cl introduces (000) and Na at $(\frac{1}{2}\frac{1}{2}\frac{1}{2})$ position. According to the X'Pert analysis, the lattice parameter has gained 5.640 Å, and it is in good agreement with the values reported in [97]. In addition, crystallographic parameters of NaCl resulting from X'Pert are submitted in Table 3.4.

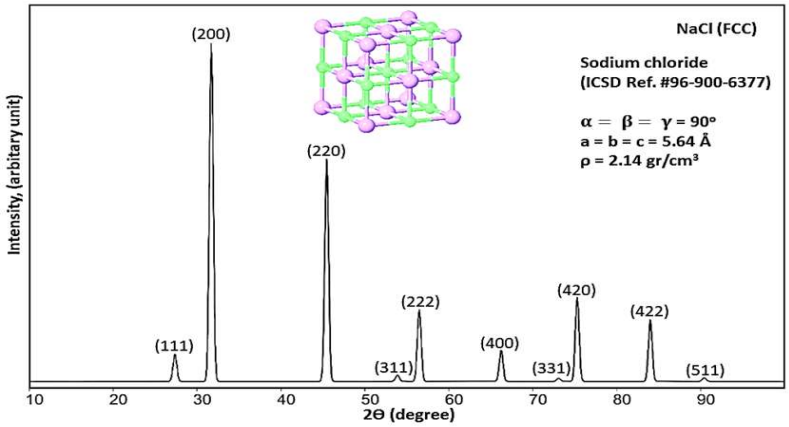

Fig. 3.7. X-ray diffraction of NaCl powder sample

Table 3.4. Crystallographic parameters of the NaCl (FCC) structure resulting from the X'Pert software

NaCl					
Crystal System	**a (Å)**	**c (Å)**	**Cell Volume $(Å)^3$**	**Crystal Density (g/cm^3)**	**Space Group**
FCC	5.640	5.640	181.511	2.141	Fm-3m

According to Fig. 3.7, 10 planes have shown diffraction. According to the discussed method in this study for gaining planar density values of each diffracted plane, the schematic geometry of planes, the situation of diffracted planes, and the location of atoms in the diffracted planes in the unit cell are shown. For illustration,

the situation of diffracted planes and atoms of NaCl and the calculation of the planar density values of diffracted planes (111) and (200) are presented in Fig. 3.8.

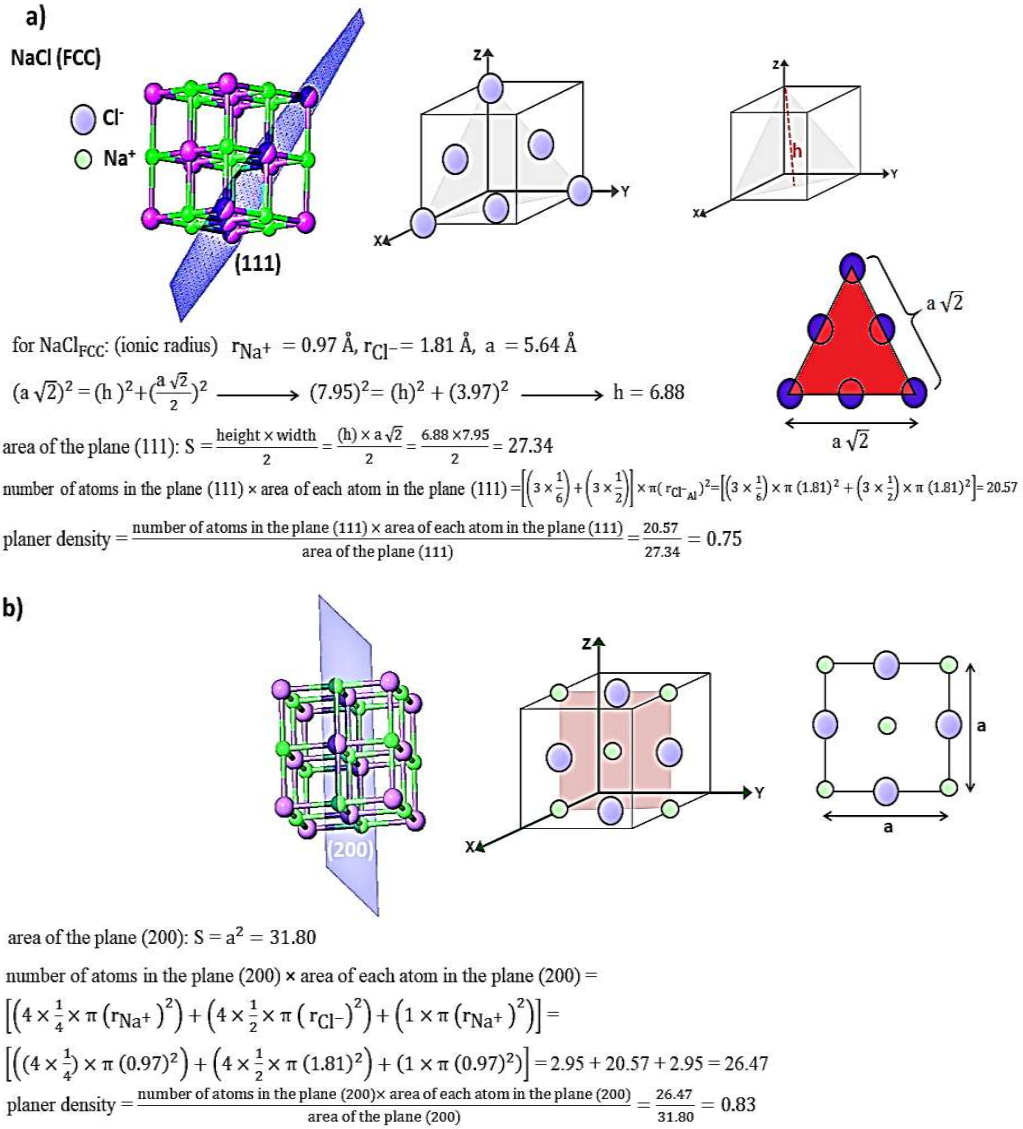

Fig. 3.8. Geometry and the situation of involved atoms in diffracted planes (a) (111) and (b) (200)

According to Equations 3.6–3.16 and 3.4 (because NaCl has an FCC structure), the values of elastic compliances (S) were substituted, and E_{hkl} values of each diffracted plane were calculated as 34.72, 44.24, 36.69, 39.18, 34.72, 36.10, 39.09, 36.69, and 41.83 GPa for planes (111), (200), (220), (311), (222), (331), (420), (422) and (511), respectively. In addition, there is no atom in (400) (as it was discussed above); therefore, this plane is not considered in the calculations. The Young's modulus of each plane of NaCl extracted by XRD patterns versus planar density is presented in Fig. 3.9. The linear equations of NaCl recorded y = 6.85x + 33.57 (Bartels et al.), y = 6.88x + 33.53 (Barsch et al.), y = 5.19x + 37.24 (Charles et al.), y = 6.79x + 33.85 (Anderson et al.), and y = 5.70x + 35.68 (this study).

Nevertheless, the intercepts were calculated as 33.57, 33.53, 37.24, 33.85, and 35.68 GPa, respectively, and the values of intercepts (Young's modulus) are tabulated in Table 3.5.

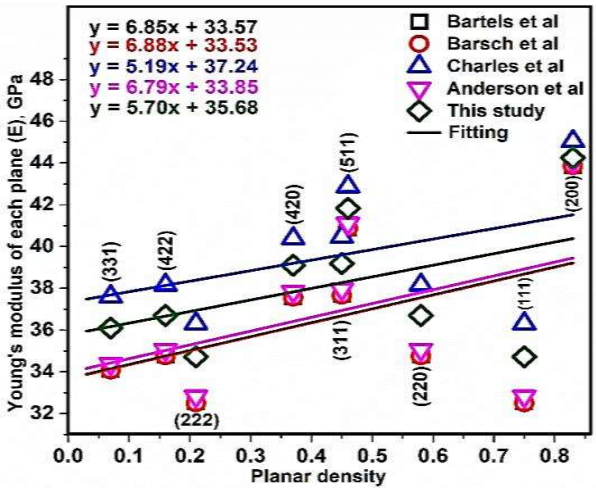

Fig. 3.9. Young's modulus of each plane of NaCl extracted by the XRD patterns versus planar density

Table 3.5. Young's modulus values of NaCl

Study	Young's Modulus (E), (Gpa) in This Method (Intercept Value)
Expt. by (Bartels et al.)	33.57
Expt. by (Barsch et al.)	33.53
Expt. by (Charles et al.)	37.24
Theory by (Anderson et al.)	33.85
This study	35.68

For a more realistic NaCl crystal system, the anisotropic nature of Young's modulus is considered [98]. The generalization of Hook's law states that the strain (ε) and stress (σ) are in a linear relationship with the constant of proportionality, being simply Young's modulus. In this method, for the NaCl structure, Hooke's law was performed for strain and stress, taking into account the linear proportionality. The exact parameters resulting from X-ray diffraction are given in Table 3.6. According to the W–H method in the USDM model, $\frac{4 \sin\theta}{E}$ (degree/GPa) played a role as the X axis, and β (radian).cosΘ (degree) played a role as the Y axis (Fig. 3.10). According to Fig. 3.10, the slope values are related to the stress (σ). The values of stress and strain have gained negative values. The positive values of intrinsic strain and stress can be provided by the tensile strain and stress, and if the values are negative, such as in Table 3.7, they will be related to the compressive stress and strain. Moreover, the stress (σ) and strain (ε) values extracted by the modified W–H method in the USDM model, shear modulus (μ), poisson's ratio (υ), and bulk modulus (B) of NaCl are reported in Table 3.7. The values of mechanical

properties were in good agreement with the values tabulated in [99]. Overall, this technique can lead to an improvement in mechanical properties with knowing the relationship between planar density and Young's modulus. Moreover, this method can be applied for research as well as industrial applications.

Table 3.6 Crystallographic parameters of each individual XRD pattern related to NaCl

NaCl										
2Θ (Degree)	B = FWHM (Degree)	Θ (Degree)	cosΘ (Degree)	1/cosΘ (Degree)	Ln(1/cosΘ) (Degree)	B = FWHM (Radian)	Ln β (Radian)	4 sinΘ (Degree)	β(Radian).cosΘ (Degree)	hkl
27.01	0.70	13.50	0.97	1.03093	0.03046	0.01218	−4.40796	0.92	0.01181	111
30.91	0.90	15.45	0.96	1.04167	0.04082	0.01566	−4.15665	1.04	0.01503	200
45.08	0.89	22.54	0.92	1.08696	0.08338	0.01549	−4.16782	1.52	0.01425	220
53.70	0.91	26.85	0.89	1.1236	0.11653	0.01583	−4.1456	1.80	0.01409	311
56.79	0.90	28.39	0.87	1.14943	0.13926	0.01566	−4.15665	1.88	0.01362	222
66.98	0.80	33.49	0.83	1.20482	0.18633	0.01392	−4.27443	2.20	0.01155	400
72.99	0.10	36.49	0.80	1.25	0.22314	0.00174	−6.35387	2.36	0.00139	331
76.05	0.70	38.02	0.78	1.28205	0.24846	0.01218	−4.40796	2.44	0.0095	420
83.93	0.81	41.96	0.74	1.35135	0.30111	0.01409	−4.26201	2.64	0.01043	422
92.60	0.10	46.30	0.69	1.44928	0.37106	0.00174	−6.35387	2.88	0.0012	511

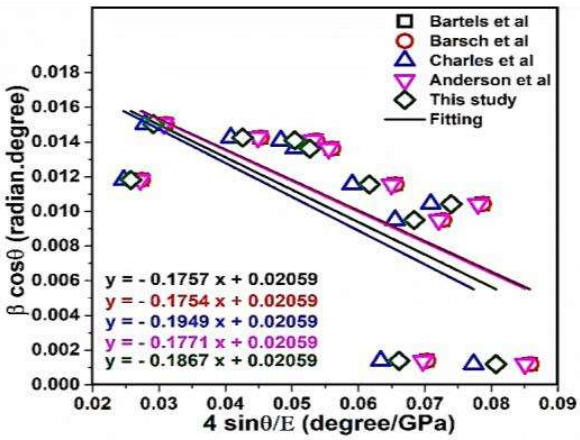

Fig. 3.10. Modified (William–Hall, W–H) uniform stress deformation model (USDM) plot of NaCl

Table 3.7. Values derived from the mechanical properties related to NaCl

Mechanical Properties					
Study	σ(GPa)	ε	μ [a] (GPa)	υ [b]	B [c] (GPa)
Expt. by (Bartels et al.)	−0.1757	−0.00523	14.91	0.24	24.71
Expt. by (Barsch et al.)	−0.1754	−0.00523	14.90	0.24	24.73
Expt. by (Charles et al.)	−0.1949	−0.00523	16.10	0.23	25.13
Theory by (Anderson et al.)	−0.1771	−0.00523	14.93	0.25	25.30
This study	−0.1867	−0.00523	15.60	0.23	24.54

•$H = 2C_{44} + C_{12} - C_{11}$ [100]

a)Shear modulus: $\mu = C_{44} - \frac{1}{5}H$ [101];

b)Poisson's ratio: $\upsilon = \frac{C_{12} - \frac{H}{5}}{2(C_{12} + C_{44} - 2\frac{H}{5})}$ [100];

c)Bulk modulus: $B = \frac{C_{11} + 2C_{12}}{3}$ [102].

3.3. Relationship between Young's Modulus and Planar Density of Unit Cell, Super Cells (2 × 2 × 2), Symmetry Cells of Perovskite ($CaTiO_3$) Lattice (Scientific Publication No. 3, Q1, 5 Quotation)

This chapter is based on the paper published in *Journal of Materials,* 2021, 14, 1−15 [81]. This chapter serves as an example of the introduction of a new technique for measuring the Young's modulus for crystallite structures, such as $CaTiO_3$ (SC).

Calcium titanate ($CaTiO_3$) was synthesized by the solvothermal method as another example of a cubic lattice. The XRD pattern of $CaTiO_3$ is presented in Fig. 3.11. The characteristic peaks of $CaTiO_3$ correspond to the report in [103]. The crystal structure of $CaTiO_3$ is cubic, the atomic positions of Ti are at (000), Ca at $(\frac{1}{2},\frac{1}{2},\frac{1}{2})$ and O at $(\frac{1}{2},0,0)$, $(0,\frac{1}{2},0)$, $(0,0,\frac{1}{2})$. According to X-ray powder diffraction results, the lattice parameter is 3.79 ± 0.02 Å, which is in good corresponds to the recorded value in the [104].

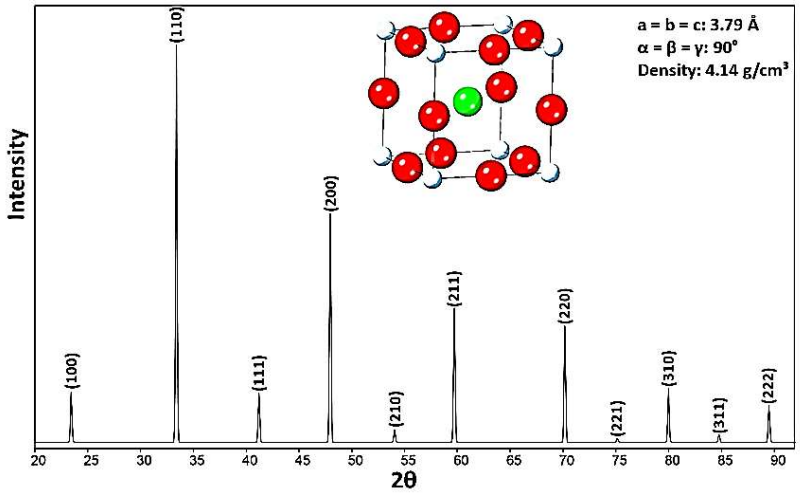

Fig. 3.11. X-ray diffraction of $CaTiO_3$ (powder sample)

For the evaluation of cells as results, the comprehensive calculations of planar density of diffracted planes in the unit cell, super cells (2 × 2 × 2) and super cells (8 × 8 × 8) of $CaTiO_3$ lattice are presented, and for example, the geometry and calculations of planar density values for (211) super cell (4 × 4 × 4) and (211) super cell (8 × 8 × 8) are depicted in Fig. 3.12.

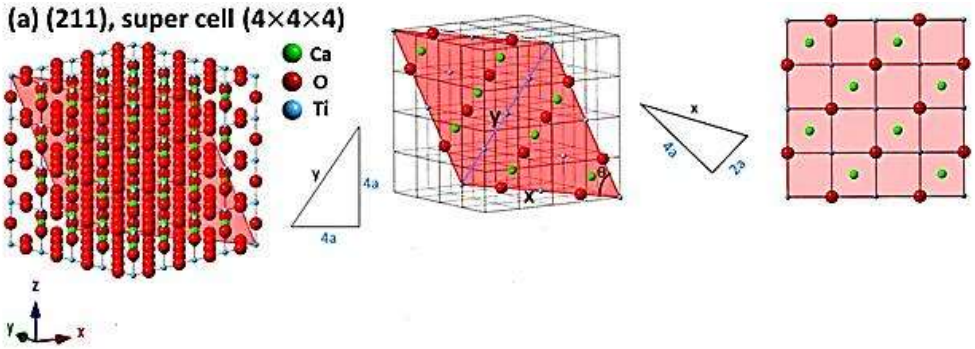

number of atoms in the plane (211) × area of each atom in the plane (211) =

$$\left[\left((2\times\frac{78.52}{360}+2\times\frac{101.48}{360}+4\times\frac{1}{2}+5)\times\pi\left(r_{Ti^{4+}}\right)^2\right)+\left((8\times\frac{1}{2}+4)\times\pi\left(r_{O^{2-}}\right)^2\right)\right]+\left[\left(8\times\pi\left(r_{Ca+}\right)^2\right)\right]=$$

$$[(8\times\pi\,(0.60)^2)+(8\times\pi\,(1.40)^2)+(8\times\pi\,(1)^2)]=83.44$$

$$\text{planer density}=\frac{\text{number of atoms in the plane (211)}\times\text{ area of each atom in the plane (211)}}{\text{area of the plane (211)}}=\frac{83.44}{334.1}=0.25$$

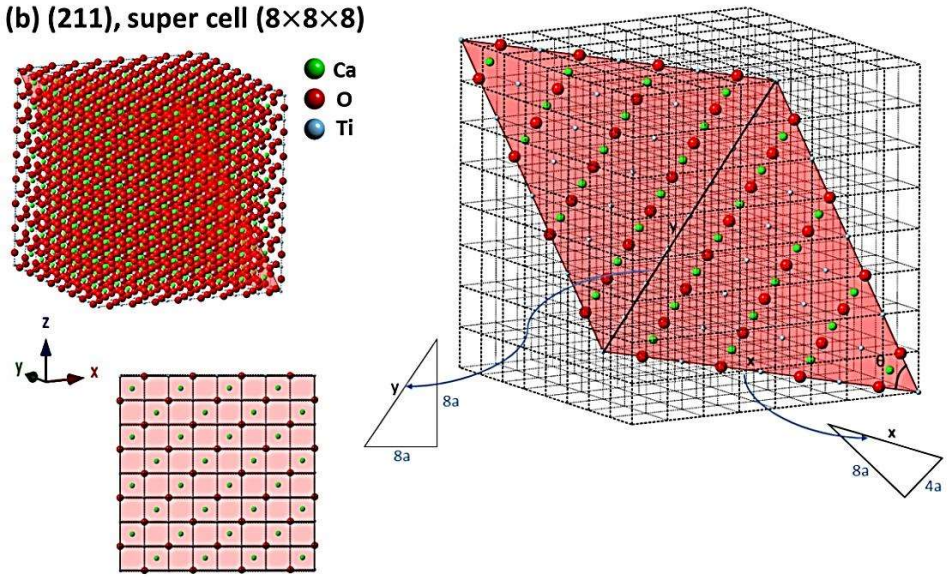

number of atoms in the plane (211) × area of each atom in the plane (211) =

$$\left[\left((2\times\frac{78.52}{360}+2\times\frac{101.48}{360}+12\times\frac{1}{2}+25)\times\pi\left(r_{Ti^{4+}}\right)^2\right)+\left((16\times\frac{1}{2}+24)\times\pi\left(r_{O^{2-}}\right)^2\right)\right]+\left[\left(32\times\pi\left(r_{Ca+}\right)^2\right)\right]=$$

$$[(32\times\pi\,(0.60)^2)+(32\times\pi\,(1.40)^2)+(32\times\pi\,(1)^2)]=333.76$$

$$\text{planer density}=\frac{\text{number of atoms in the plane (211)}\times\text{ area of each atom in the plane (211)}}{\text{area of the plane (211)}}=\frac{333.76}{1335.24}=0.25$$

Fig. 3.12. Geometry of planes and calculations of planar density of (a) (211) super cell (4 × 4 × 4) and (b) (211) super cell (8 × 8 × 8)

Based on the Equations 3.6–3.16, 3.4, Fig. 3.13, and the measured velocity according to Table 3.8, the stiffness constants values were obtained. C_{11} is in

agreement with the longitudinal distortion and longitudinal compression/tension; thus, C_{11} can be described as hardness. Moreover, the transverse distortion is connected to the C_{12}, and C_{12} is obtained from the transverse expansion correlated to the poisson's ratio. C_{44} is based on the shear modulus, and C_{44} is in settlement with C_{11} and C_{12} [105].

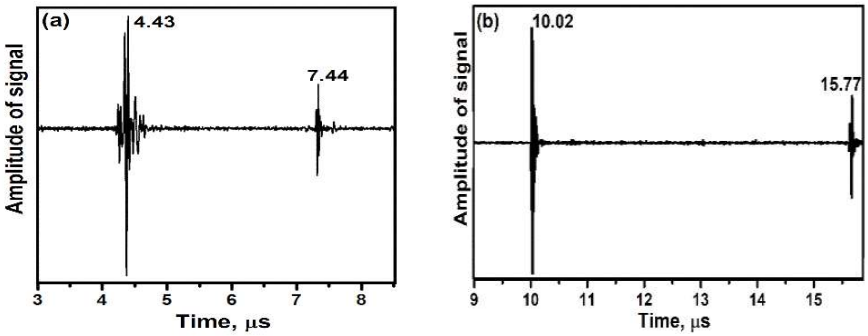

Fig. 3.13. Recorded signals extracted via (a) longitudinal waves and (b) transverse waves of $CaTiO_3$ specimen

Table 3.8. Values of longitudinal and transverse velocity of the sample

Longitudinal Velocity (m/s)	**Transverse Velocity (m/s)**	**Quasi Longitudinal or Quasi Transverse (m/s)**
$V_{1/1} = 9261.85$	$V_{2/3} = 4960.5$	$V_{12/12} = 4976.63$
$V_{2/2} = 8013.51$	$V_{1/2} = 4283.65$	

After substitution and calculation, C_{11}, C_{12}, and C_{44} were registered at 330.89, 93.03, and 94.91 GPa, respectively. These values of $CaTiO_3$ were in good agreement with the values submitted in [106, 107]. According to the results, t_s and t_l values are calculated as 5.75 and 3.01 μs, respectively. In addition, the density of the specimen is recorded as 3857.30 $\frac{Kg}{m^3}$, and the length of the specimen after powder pressing reached 11.21 mm. After calculation, Young's modulus value of $CaTiO_3$ was 153.87 GPa. This value corresponds with the value reported by Ramajo et al. [108]. Furthermore, the planar density and Young's modulus values related to the each diffracted plane of the unit, super (2 × 2 × 2), symmetry and super (8 × 8 × 8) cells of $CaTiO_3$ lattice are tabulated in Table 3.9.

Table 3.9. Planar density and Young's modulus values of the unit cell, super cells (2×2×2) and symmetry cells of $CaTiO_3$

Index	Planar Density of Unit Cell	Planar Density of Super Cell (2 × 2 × 2)	Planar Density of Symmetry Cells	Planar Density of Super Cell (8 × 8 × 8)	Young's Modulus (GPa)
(100)	0.93	0.93	0.93 in (2 × 2 × 2)	0.93	290.059
(110)	0.51	0.51	0.51 in (2 × 2 × 2)	0.51	221.652
(111)	0.04	0.04	0.04 in (2 × 2 × 2)	0.04	179.354
(200)	0.64	0.64	0.64 in (2 × 2 × 2)	0.64	290.059
(210)	0.41	0.41	0.41 in (2 × 2 × 2)	0.41	194.176
(211)	0.16	0.25	0.25 in (2 × 2 × 2)	0.25	150.612
(220)	0.6	0.6	0.6 in (2 × 2 × 2)	0.6	129.810
(221)	0.46	0.29	0.31 in (4 × 4 × 4)	0.31	109.622
(310)	0.24	0.24	0.23 in (4 × 4 × 4)	0.23	186.471
(311)	0.04	0.03	0.02 in (3 × 3 × 3)	0.02	140.386
(222)	0.99	0.88	0.88 in (3 × 3 × 3)	0.88	83.615

In order to compare Young's modulus values of $CaTiO_3$ in a unit cell, super cells (2 × 2 × 2) and symmetry cells, the fitting of Young's modulus values extracted by each diffracted plane versus planar density values are presented in Fig. 3.14. Further on, the results and the straight fitting line, Young's modulus values of unit cell, super cells (2 × 2 × 2) and symmetry cells were calculated as 162.62 ± 0.4 GPa, 151.71 ± 0.4 GPa, and 152.21 ± 0.4 GPa, respectively. As expected, the Young's modulus value of symmetry cells of $CaTiO_3$ (152.21 ± 0.4 GPa) is in good agreement with the experimental Young's modulus value extracted via ultrasonic-echo technique (153.87 ± 0.2 GPa). Moreover, Young's modulus value of unit cell (162.62 ± 0.4 GPa) has a greater difference with experimental Young's modulus value, and as a result, the unit cell of $CaTiO_3$ cannot be represented as whole cells. This is due to the fact that in a unit cell of $CaTiO_3$ crystallite, the defects are not taken into account, and in particular, the deformation is controlled, and the displacement of atoms in the planes is related to the dislocation networks [109]. Furthermore, a unit cell of $CaTiO_3$ is not involved in imperfections (such as dislocations, Frenkel and Schottky defects) with respect to the super cell [110]; therefore, the slope line value of the unit cell is reported (37.23) to be less than the slope line value of super cells (2 × 2 × 2) (63.67) and symmetry cells (62.41). Consequently, the effect of imperfections in expanded cells (super cells) is very impressive; thus, the unit cell of $CaTiO_3$ is considered the ideal lattice, while symmetry cells, such as (8 × 8 × 8) of $CaTiO_3$ are real lattices [111]; this is consistent with the experimental Young's modulus. It is clear that each imperfection will be caused by a decreasing Young's modulus [112], and in Fig. 3.14, this matter is confirmed when the Young's modulus value (intercept) in the unit cell of $CaTiO_3$ is higher than in the super cells (2 × 2 × 2) and symmetry cells. Apparently, a unit cell of $CaTiO_3$ is represented by the volume of a real crystal; thus, the unit cell is useful to acquire theoretical density. Nevertheless, the calculations of planar density based on the unit cell were obtained, but with errors. Overall, the values obtained with this technique can improve the mechanical properties due to the calculated values of Young's modulus that derived from X-ray diffraction.

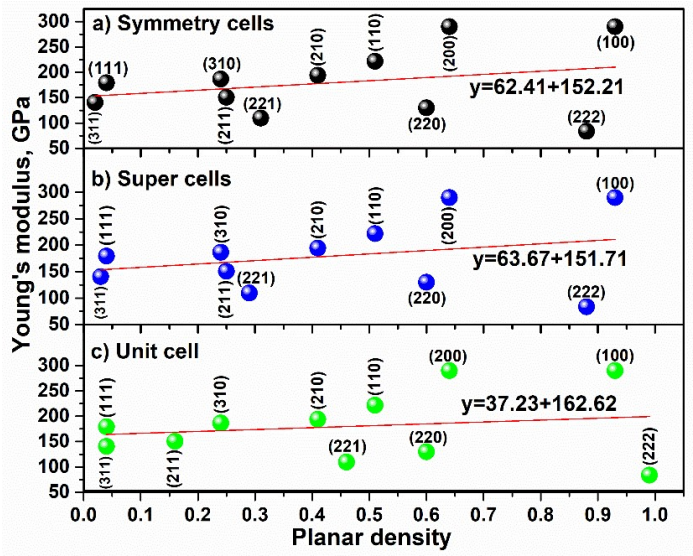

Fig. 3.14. Young's modulus versus planar density values of each diffracted plane related to the (a) symmetry cells, (b) super cells (2 × 2 × 2), and (c) unit cell of $CaTiO_3$

3.4. X-ray Diffraction Analysis and Williamson–Hall Method in USDM Model for Estimating More Accurate Values of Stress-Strain of Unit Cell and Super Cells (2 × 2 × 2) of Hydroxyapatite, Confirmed by Ultrasonic Pulse-Echo Test (Scientific Publication No. 4, Q1, 4 Quotations)

This chapter is based on the paper published in *Journal of Materials*, 2021, 14, 1–16 [113]. This chapter serves as an example of the introduction of a new technique for measuring the Young's modulus for crystallite structures, such as HA (Hexagonal).

The XRD pattern of synthesized HA powder is shown in Fig. 3.15. In addition, the XRD pattern has shown several diffraction peaks in the range from 20° to 70°, which can be described as hexagonal HA. The XRD pattern was evaluated based on X'pert, and the pattern was in agreement with the standard XRD peaks of HA (ICDD 9-432). Similar observations were reported in [88, 87].

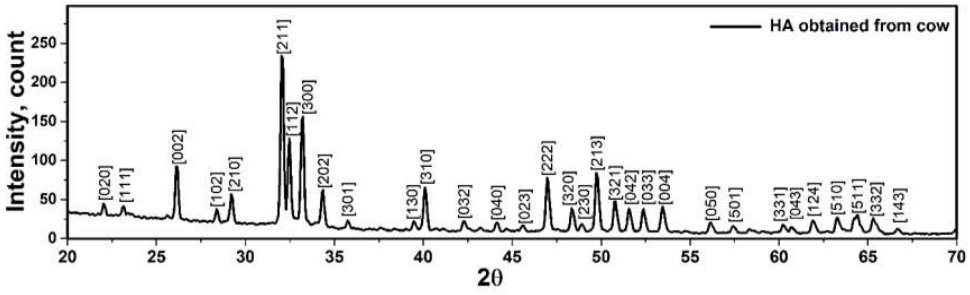

Fig. 3.15. X-ray diffraction pattern of HA synthesized at 950 °C

According to the X-ray diffraction, the planar density values of each diffracted plane in unit cell and super cells (2 × 2 × 2) of HA were calculated, and as an example, the array geometries and calculations of unit cell (020) and super cell (020)

are depicted in Fig. 3.16. In order to calculate the planar density values, diffracted planes were selected from a low angle to a high angle in tandem. It is worth mentioning that the matrix of all super cell lattices was considered to be 2 × 2 × 2. According to the center of atoms, the planar density is calculated by the area of atoms in the plane divided by the total area of that plane [114].

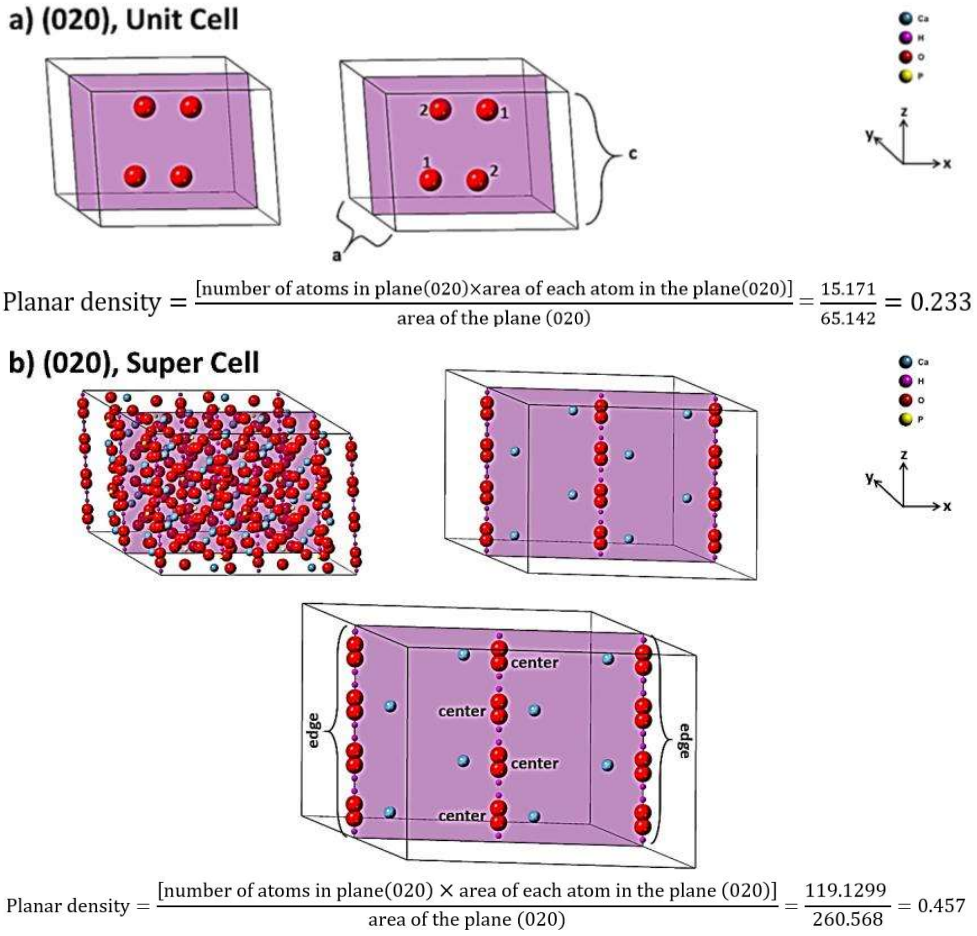

Fig. 3.16. Array and position of the involved atoms, such as (a) (020) unit cell and (b) (020) super cell of HA hexagonal

X-ray diffraction has provided data on diffracted planes and the location of atoms in each plane. It is clear that the planar density of each diffracted plane was calculated, and it could play an important role in the mechanical properties of each plane. The Young's modulus of each plane (E_{hkl}) of a HA lattice can be calculated with this technique. Taking into account Equation 3.5, h, k, and l are the plane indices; a and c are the lattice parameters; C and S are the elastic stiffness constant and elastic compliance, respectively.

By using the least squares method between the Young's modulus and the planar density of diffracted planes (based on the proposed method), the Young's modulus value of HA was determined with high precision. Consequently, the calculation of C and S parameters for crystallite materials is essential for the

application of this technique. In order to show the feasibility and accuracy of the proposed method for determining the Young's modulus, the values of Young's modulus of each plane versus the planar density of the unit cell and super cells (2 × 2 × 2) are shown in Fig. 3.17.

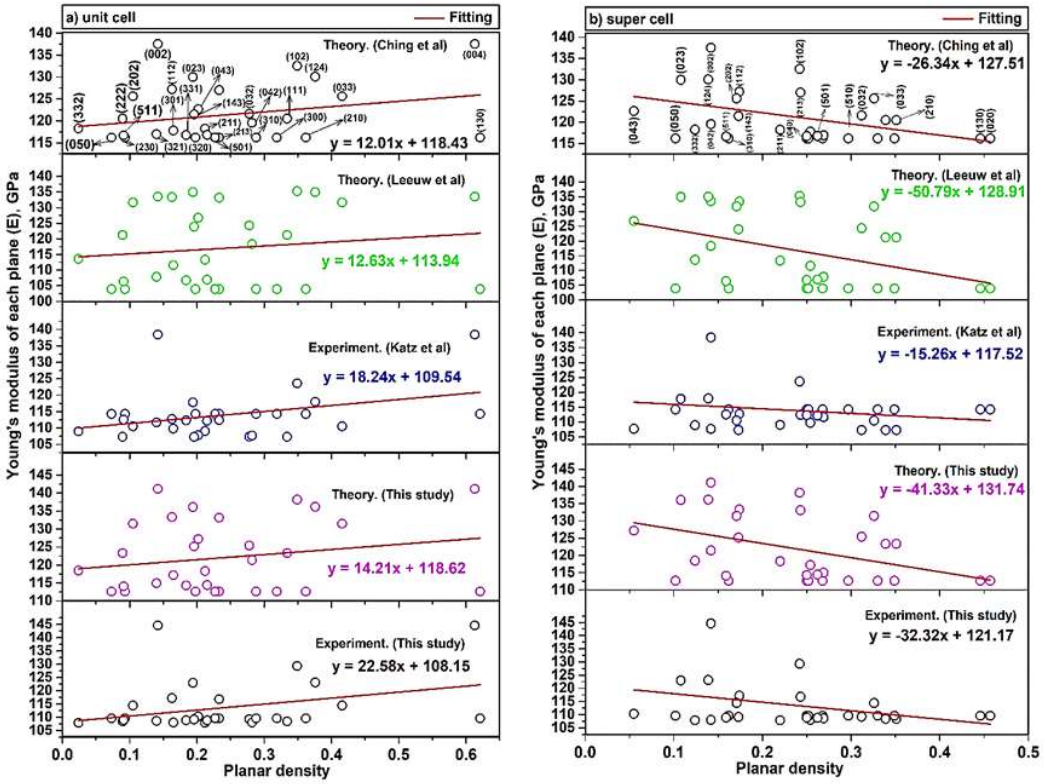

Fig. 3.17. Young's modulus of each plane (a) unit-cell (b) super cells (2 × 2 × 2) of HA extracted by XRD patterns and planar density

According to the uncertainty measurement, the measurements were replicated five times, and the Young's modulus value gained 113.08 ± 0.14 GPa by ultrasonic measurement. This value is in good agreement with the reported values of this study. In this study, the difference between theory and experiment values for both unit cell and super cells (2 × 2 × 2) were identical. This difference for unit cell and super cells (2 × 2 × 2) are 10.47 GPa and 10.57 GPa, respectively. This means that the theoretical calculation is valid, and by reducing it by about ~10 GPa, the experimental values can be obtained. The Young's modulus values of unit cell and super cell (2 × 2 × 2) lattices of HA are tabulated in Table 3.10.

Table 3.10. Young's modulus values of unit cell and super cell lattices of HA

Study	Young Modulus (E), (Gpa) in This Method (Intercept Value)	
	Unit Cell	Super Cells (2 × 2 × 2)
Theory (Ching et al.)	118.43	127.51
Theory (Leeuw et al.)	113.94	128.91
Experiment (Katz et al.)	109.54	117.52
Theory (This Study)	118.62	131.74
Experiment. (This Study)	108.15	121.17

It is noteworthy that the difference of Young's modulus values in the unit cell and super cells (2 × 2 × 2) is attributed to the locations of atoms. The calculated slope is a negative value in super cells (2 × 2 × 2). In the first aspect, it is clear that the slope depends on the planar density of the diffracted planes; thus, the fitting based on the planar density of the super cells with a matrix of 8 unit cells might give a better result for the intercept [115]. It is because 8 cells besides each other are completed and have more symmetry than two cells (Fig. 3.18) [115]. In the second aspect, the reason for the positive slope in the unit cell and the negative slope in the super cells (2 × 2 × 2) is related to the defects (imperfections), including point defects (vacancies, substitutional and interstitials), line defects (screw and edge dislocation), surface defects (grain boundaries), and volume defects (lack of order of atoms due to amorphous region in a very tiny area). The effect of these imperfections is impressive in super cells (2 × 2 × 2), while the unit cell is more ideal and less affected by these imperfections. This means that when the density of atoms in the planes is increased, lower forces are required for the dislocation motion, and the strength decreases. Consequently, the slope in super cells (2 × 2 × 2) is negative. In the case of super cells, when the number of atoms increases, with the increase of planar density, the effect of dislocation motion increases as well; therefore, the strength and Young's modulus will decrease, and the slope will be negative. The intercept of the fitting line is a value of Young's modulus, which can show the Young's modulus of the plane with zero planar density as a plane without any specific atom.

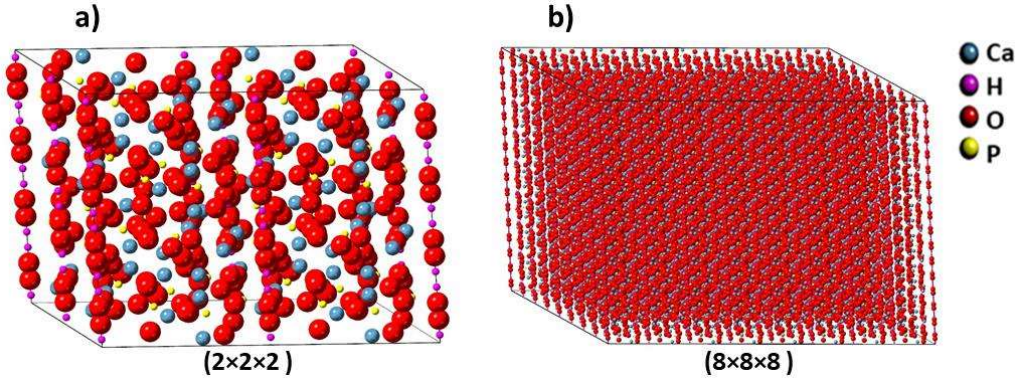

Fig. 3.18. (a) The un-symmetry of two unit cells and (b) symmetry of 8 unit cells of HA

Taking into account the W–H method in the USDM model, Young's modulus values are examined. It is clear that in Equation 3.6 and Fig. 3.19, the term of $\frac{4\sin\theta}{E_{hkl}}$ is along the X-axis, and the term of $\beta_{hkl}.\cos\theta$ is along the Y-axis individually.

$$\beta_{hkl}.\cos\Theta = \left(\frac{K\lambda}{L}\right) + 4\sigma\frac{\sin\theta}{E_{hkl}} \text{ [116].} \quad (3.6)$$

In this model, the condition is performed to calculate the strain and the average Young's modulus. The average Young's modulus value has been calculated in the research and studies on using the W–H method, but it is subject to errors, because if the average values of the Young's modulus are considered, the final value can be far from the standard value of Young's modulus in each peak extracted by the X-ray diffraction. In addition, in some studies, the Young's modulus value is considered a value that is listed in the literature but is not associated with the prepared materials. As an illustration, based on the study in [117], which refers to the use of the W–H method to calculate the crystal size and Scherrer analysis of HA, the average value of Young's modulus has a larger deviation than the actual value of the Young's modulus of HA. According to Fig. 3.19, the slope values are associated with the stress (σ). The obtained values were positive, and the positive values of intrinsic strain and stress can prove tensile stress and strain, and if the values were negative, they would be associated with compressive stress and strain. Additionally, the resulting values of σ and ε by utilizing the W–H method in the USDM model are shown in Table 3.11. Additionally, the value of σ is in good agreement with the values obtained from [118]. This technique can lead to an improvement in the mechanical properties of composites composed of HA due to the relationship between the Young's modulus and the planar density of unit cell and super cells (2 × 2 × 2) of HA.

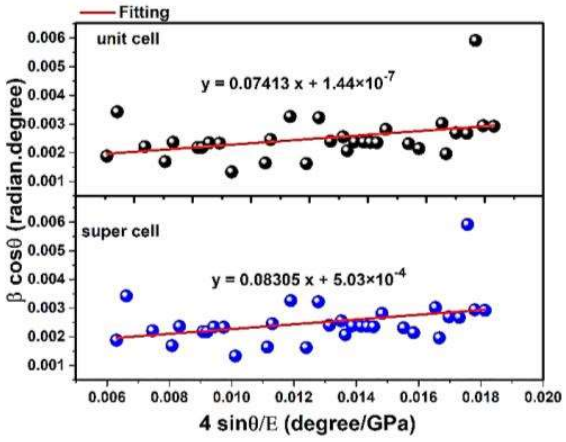

Fig. 3.19. The W–H in USDM model and plot of unit cell and super cells (2 × 2 × 2) of HA

Table 3.11. Mechanical properties values of unit cell and super cells (2 × 2 × 2) of HA

Mechanical Properties			
Structure	**σ (GPa)**	**ε**	**E[a] (GPa)**
Unit cell	0.07413	0.00068	108.15
Super cells (2 × 2 × 2)	0.08305	0.00068	121.17

a: experiments of Young's modulus values (this study)

3.5. New Approach for Preparing Invitro Bioactive Scaffold Consisted of Ag-Doped Hydroxyapatite + Polyvinyltrimethoxysilane (Scientific Publication No. 5, Q1, 2 Quotations)

This chapter is based on the paper published in *Journal of Polymers*, 2021, 13, 1−19 [119]. This article contains a prepared scaffold of Ag-doped HA+PVTMS for the first time. In this study, a mechanochemical process was carried out to synthesize Ag-doped HA. Taking into account the differential scanning calorimetry (DSC) curve of a hair band and slurry, the final sintering temperature was chosen 350 °C, and porous scaffold was fabricated. The porosities were opened, which can be suitable to increase the ratio of biocompatibility. The doping mechanism, structural evolution, morphological properties, mechanical properties, and bioactivity analysis were fully studied by spectroscopic and microscopic techniques.

According to Fig. 3.20, artificial HA was synthesized by sol−gel method. Taking into account the Ca/P ratio of HA, calcium nitrate tetrahydrate ($Ca(NO_3)_2.4H_2O$) and phosphorus pentoxide (P_2O_5) were used in the molar ratio of 10:3. Tandemly, 1) $Ca(NO_3)_2.4H_2O$) and P_2O_5 were dissolved in 10 ml of ethyl alcohol (C_2H_5OH) and distillated water. 2) The product was stirred at 350 rpm for 2 h. 3) The gel was prepared at the bottom of the dish. 4) The gel was dried at 110 °C in the air for 20 h. 5) Heat treatment at 850 °C for 15 h was considered for sintering.

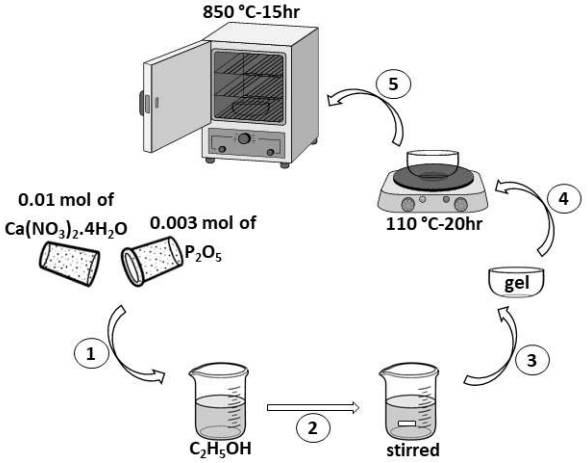

Fig. 3.20. The schematic flow diagram of the synthesis route of artificial HA

Vinyltrimethoxysilane (VTMS) was polymerized to 20-mers. PVTMS with tertiary butyl peroxide was an initiator under reflux for 2 h at 150 °C in flowing nitrogen [120, 121]. In addition, the synthesis route of PVTMS is shown in Fig. 3.21.

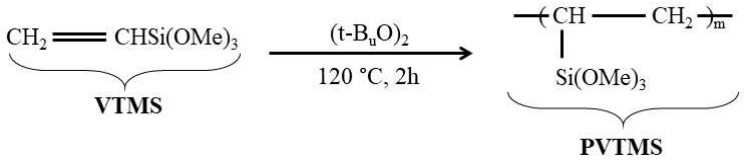

Fig. 3.21. Synthesis route of PVTMS

In this study, silver nitrate ($AgNO_3$) with 99% purity was used as the dopant. The amount of replacement of Ca^{2+} ions by Ag^+ corresponds to the formula $Ca_{10-X}Ag_X(PO_4)_6(OH)_{2-X}$ $_X$. In this case, X = 2, and $_X$ is represented as the x-mole of OH-vacancy formed by doping X-mole of Ag in the HA lattice. Moreover, the ratio of (Ca + Ag)/P was set to 1.67, while the degree of cationic substitution had been changed. 1) The powders of HA and $AgNO_3$ were grounded by using a high-energy planetary ball mill via a mechanochemical process for 4 h. In mechanochemical process, hard chromium steel shells and balls with a diameter of 20 mm were used. This process was carried out at ambient atmosphere and the rate of 500 rpm with a ball to powder ratio of 15:1. In addition, to prevent agglomeration of particles, the machine was stopped after 45 minutes. 2) After the end of mechanochemical process, the calcination was carried out at 900 °C at a rate of 10 °C per minute for degassing (90 min). 3) Taking into account the fact that HA is very sensitive to temperature, transformation, and decomposition, the spark plasma sintering (SPS) process was considered. In this process, the powder was placed in the graphite mold (diameter = 20 mm), and pressure and temperature values were set at 50 MPa and 600 °C for 10 minutes, respectively. The route of the fabricated Ag-doped HA composite is shown in Fig. 3.22. 4) Components of a slurry, consisting of Ag-doped HA (93 wt%)/PVTMS (5 wt%)/H_2O (1 wt%)/CH_3COOH (1 wt%), were prepared. 5) In addition, a hair band (commercial) was chosen as a new approach to obtain open porosities, 6) which was immersed in the slurry for 5 days at room temperature. According to Fig. 3.22, the hair band was cut and opened, and the tape was pulled out; the taped hair band was immersed in the slurry, and then, the tape was rolled up. 7) Then, the product was placed in the furnace at 350 °C for 1 h, according to the DSC curve, vinyl groups, and temperature of the burning hair band. Finally, the porous scaffold consisting of Ag-doped HA + PVTMS was fabricated. It is necessary to mention that HA is considered as a bioactive matrix due to the presence of calcium phosphate groups. Moreover, Ag is the best metal for the antibacterial environment. In addition, acetic acid (CH_3COOH) has played an important role as a dispersant for particles, especially for Ag, to prevent the formation of colloidal particles and prepare small particles. PVTMS played an important role as a drying control chemical additive (DCCA) to prevent cracking and shrinkage of scaffold. Moreover, as shown in Fig. 3.21, the free radicals of PVTMS structure can contribute to the flexibility of the scaffold through the

bonding between C-C and siloxane (Si-O-Si). Furthermore, PVTMS has carbon chains, and these chains can help to prevent the collapse of scaffold during the heat treatment, leaving solvent and volatile materials and creating porosity without damaging the scaffold. It should be noted that two different ways of synthesis were used, since HA is very sensitive to the calcination temperature, and for doping and maintaining the HA, the use of SPS was essential.

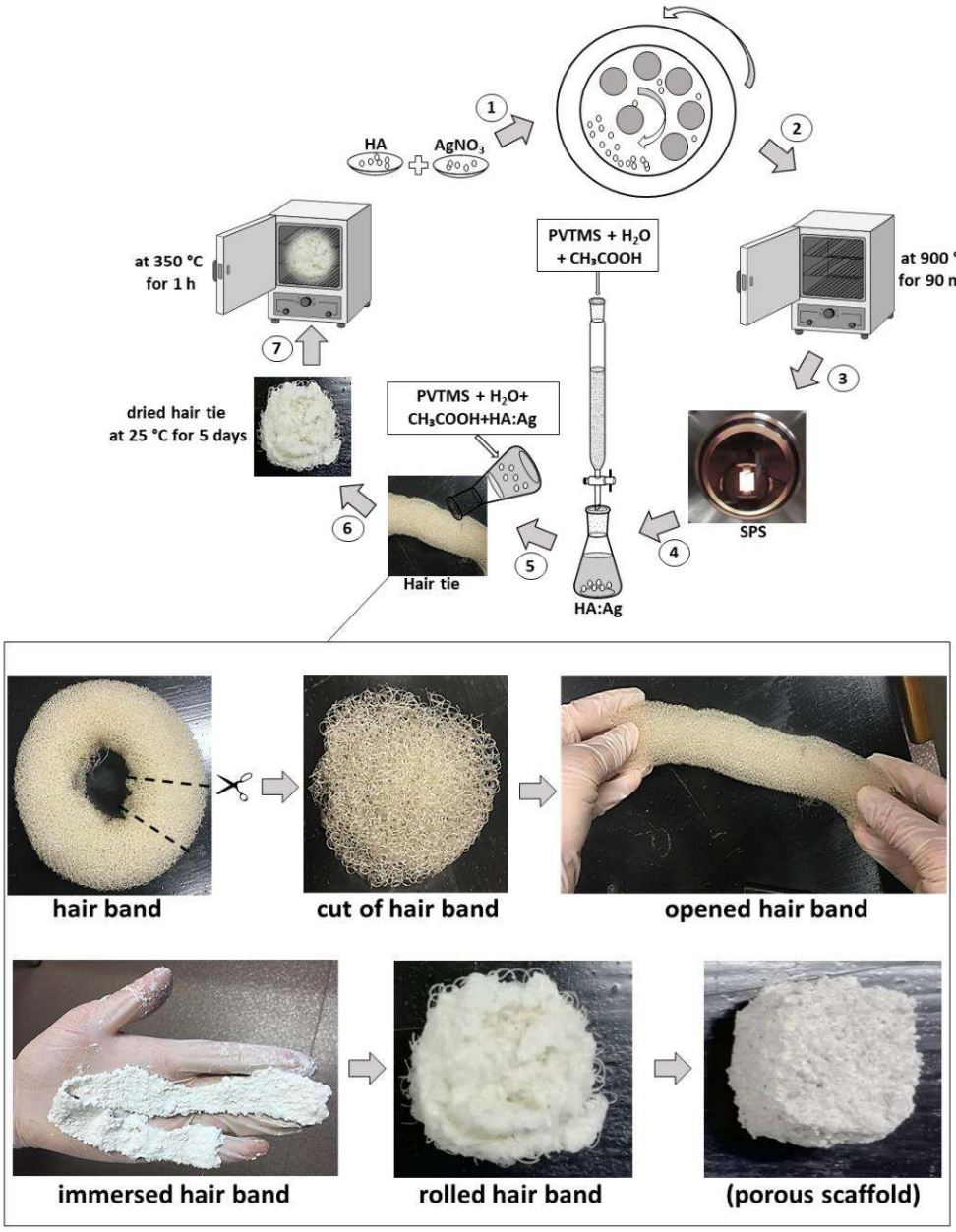

Fig. 3.22. The routes of fabricated Ag-doped HA + PVTMS scaffold

The scanning electron microscope (SEM) images of the Ag-doped HA + PVTMS scaffold are shown with different magnification in Fig. 3.23. There is no existence of an amorphous phase and agglomeration in the scaffold. The effect of leakage (exit) of O, H, and C in the rolled hair bond during the heat treatment leads

to the creation of porosities. The porosity size (>100 microns), the amount of porosity, and the open porosity are caused by a high coefficient of bioactivity, because the porosities are the best place for bonding between calcium and phosphate groups. According to Fig. 3.23, the uniformity of porosity is shown, and the average porosity size is ~>200 microns: this value is suitable for the immigration of osteoblasts in porosities [122]. The best advantage of this study is related to creating porosity with high size without the collapse of a scaffold. Furthermore, according to studies, the minimum porosity size for significant bone growth is 75–100 microns with an optimal range from 100 to 135 microns [123, 124]. Therefore, in this study, the porosity with a big size (higher than 200 microns) is produced. However, it is important to identify the upper limits of the pore size, as large pores may be affected by the mechanical properties of the scaffolds by increasing the pore volume [125].

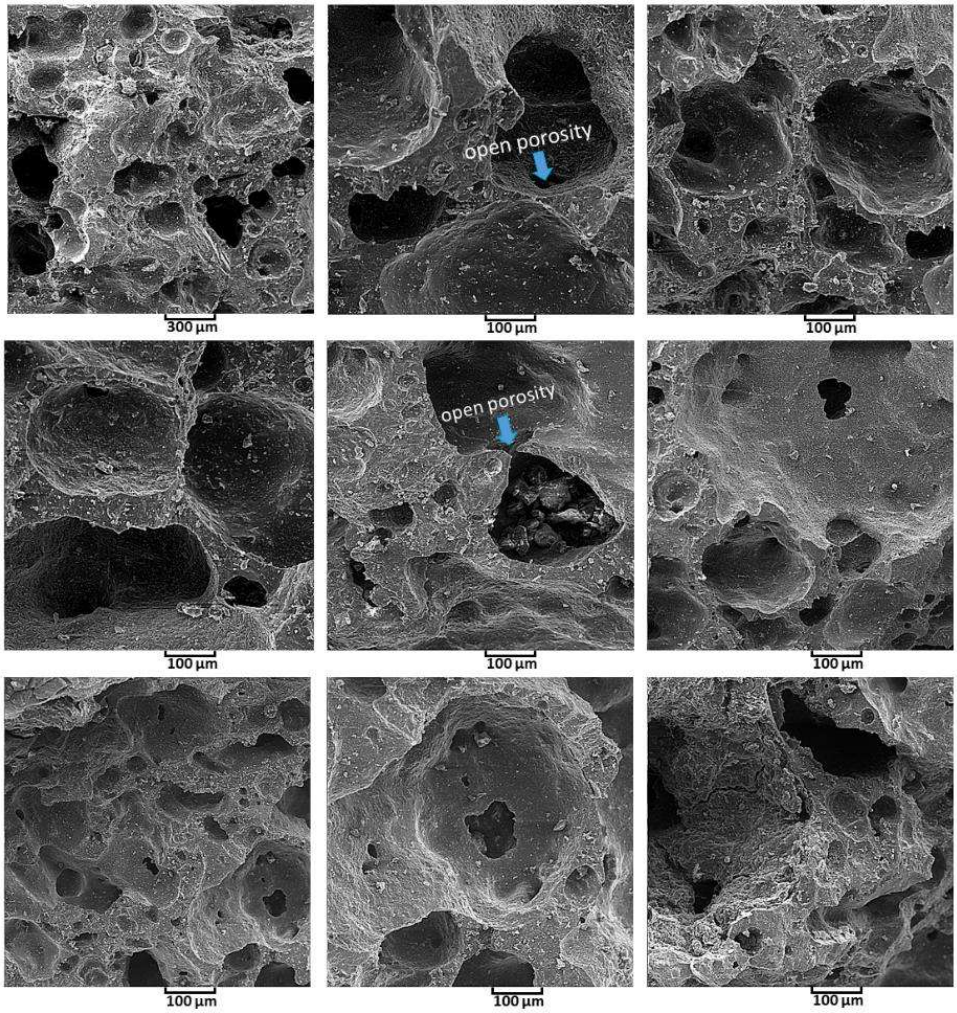

Fig. 3.23. The SEM images of Ag-doped HA + PVTMS scaffold

The stress-strain-compression curve of the Ag-doped HA + PVTMS scaffold is shown in Fig. 3.24. The maximum value of compressive strength is measured to be 15.71 MPa at a strain of ~0.77. According to Hooke's law, with the selection of difference values of two points in the elastic region, the elastic coefficient was

calculated ~3.86 MPa: this value is lower than the natural HA standard value, and it is associated with the porous scaffold, and specifically, the size of porosity is larger due to the focus of bioactivity of this study [43, 126]. The value of the maximum compressive strength was not predicted, according to the utilized hair band as a mold. This value is valuable because of 1) the fabrication of scaffold through using components, such as Ag-doped HA (93 wt%)/PVTMS (5 wt%)/H_2O (1 wt%)/CH_3COOH (1 wt%), without using metals with high concentration. 2) In this case, the bioactivity characteristics and creating large size of porosities were the main purpose, and taking into account the initial bioactivity of ingredients, the use of high concentration metals, such as Mg, Zn, Pt, can improve the value of compressive strength and mechanical properties.

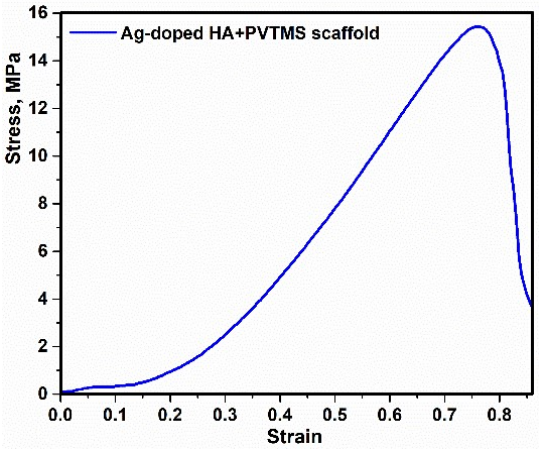

Fig. 3.24. The curve of stress-strain compression of Ag-doped HA + PVTMS scaffold

Simulated body fluid (SBF) was prepared according to the method of Kokubo et al. [127]. Taking into account the temperature at 37 °C, the materials were added and dissolved according to Fig. 3.25. Afterwards, $(CH_2OH)_3CNH_2$ and HCl were added (dropwise) to achieve the pH to 7.40 (final pH); then, the temperature was decreased (20 °C), and the distilled water was added [127]. In addition, the scaffold was immersed in SBF (100 ml) and kept in the oven at 37 °C (similar to body temperature). After 3, 5, 10, and 20 days, the scaffold was pulled out and washed with distillated water; then, the analyses, such as XRD, FTIR, SEM and EDAX, were performed.

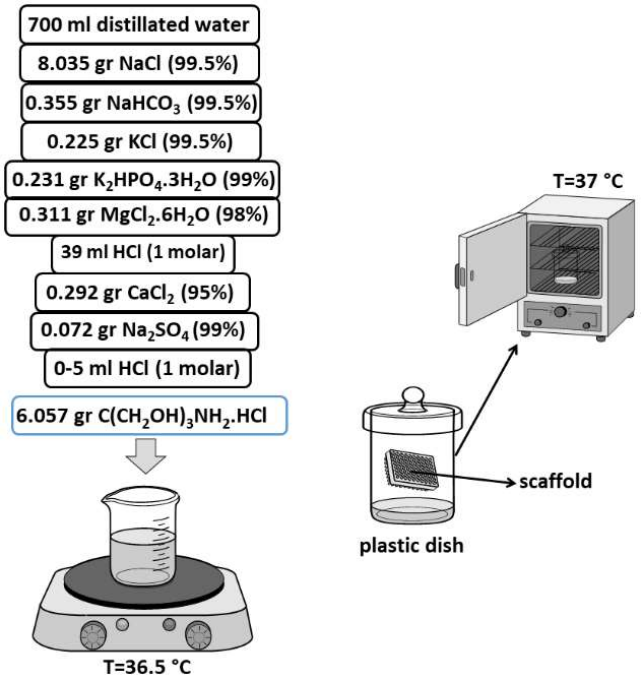

Fig. 3.25. Synthesis of SBF [127], immersed scaffold in the SBF at 37 °C

According to the SEM images (Fig. 3.26) of pulled out scaffold (after immersion), the synthesis of the viscose slurry as well as the existence of porosities and utilizing hair band as a novelty were useful and effective. The rate of precipitation of HA on the surface of the scaffold was very high when the porosities were filled only after 3 days of immersion (Fig. 3.26 a). In addition, with this idea (utilizing hair band as a mold), the diffusion of calcium and phosphor ions from SBF into the porosities was increased. Nevertheless, needle-shaped morphology (initial morphology) of HA [128] is converted to the sphere shapes. As mentioned in [129] and [130], these porosities are applicable according to the size of blood cells and requirements of the big porosities for siting the blood cells into the porosities and increasing the ratio of bioactivity. Taking into account the mechanical properties of porous scaffolds, whatever the amount and size of porosity are bigger, the ratio of bioactivity will be increased [131]. According to Fig. 3.26, the precipitation of HA increased over the time of immersed scaffold. Taking into account the mechanism of precipitation and preparation of HA on the surface of the scaffold, the existence of HCl in SBF is caused by increasing the precipitation of HA due to the increasing numbers of polar groups on the surface of the scaffold and increasing the ratio of absorbance [132, 133]. Furthermore, Fig. 3.26 shows the result of EDAX of existence of HA on the surface during 3, 5, 10, and 20 days. The ratio of Ca/P was 1.71, 2.07, 1.53, and 1.64 for immersed scaffold in SBF during 3, 5, 10, and 20 days, respectively. It is clear that the Ca/P ratio reached 1.64 after 20 days of immersion, and this value is closer to the ratio of Ca/P = 1.67 from natural HA [134].

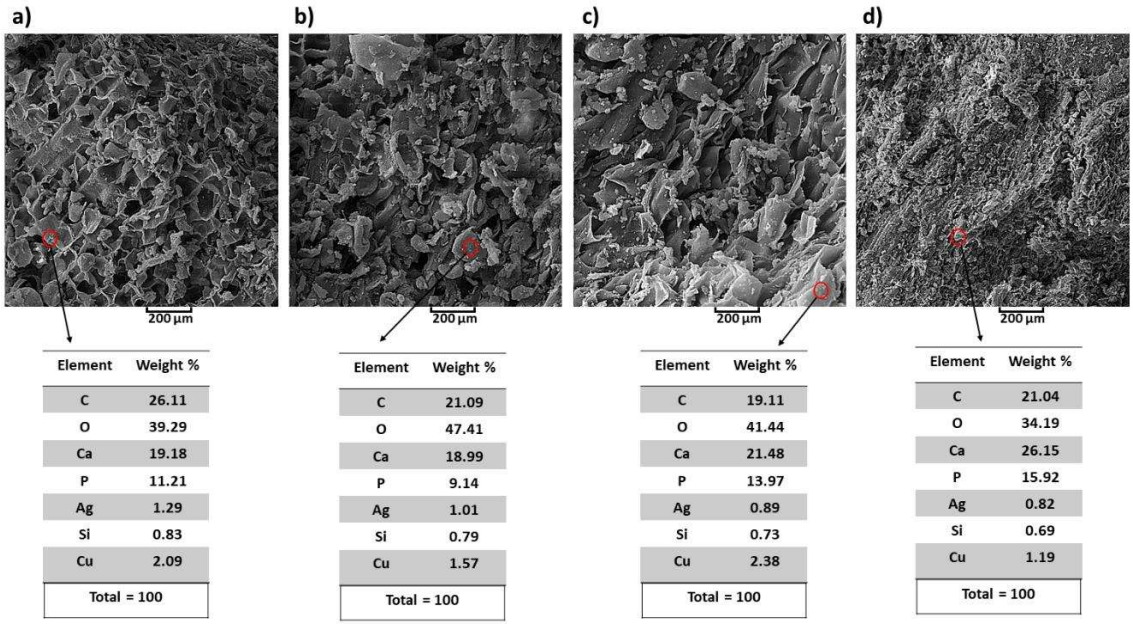

Fig. 3.26. SEM EDAX data of immersed scaffold in SBF after (a) 3 days, (b) 5 days, (c) 10 days, and (d) 20 days

3.6. The Effect of Calcination Temperature on the Photophysical and Mechanical Properties of Copper Iodide (5 mol%)-Doped Hydroxyapatite (Scientific Publication No. 6, Q2, 2 Quotations)

This chapter is based on the paper published in *Optical Materials Journal*, 2021, 121, 1–12 [135]. In this study, the prepared composites, which consisted of CuI (5 mol%)/HA, were very sensitive to the calcination temperature (from 25 to 900 °C). The main point of this work was to characterize CuI (5 mol% concentration)-doped HA and improve the properties, especially mechanical properties. Furthermore, the nanocomposite was prepared by an adapted method and calcined at different temperatures. In this study, facile controlled route to prepare the CuI (5 mol%)/HA nanocomposite was an advantage. The results confirmed that the formation of CuI/HA at different calcination temperatures with controlled nanosize of particles have the capability for applications in mechanical generations.

In this study, in order to achieve high uniformity and purity, copper (II) sulfate ($CuSO_4$) was coated on the clean quartz substrate by physical vapor deposition (PVD) method as a source of copper. The summarized synthesis method of copper iodide (CuI) particles is shown in Fig. 3.27. As shown in Fig. 3.27, first, the copper substrate was immersed in acetone (C_3H_6O) and isopropyl alcohol (C_3H_8O); then, the solution was etched and stirred with dilute aqueous chloroform ($CHCl_3$) (10 mol L^{-1}) for 20 minutes. Second, 5 ml of C_3H_8O and hydrochloric acid (HCl) were added to the solution under the vibrating ultrasound for 20 minutes; this procedure was repeated and filtered three times with deionized water; then ,the quartz substrate was removed. Third, 3 mmol solution of potassium iodide (KI) and 20 mL of deionized water were added and sonicated for 30 minutes; then, the reaction was completed.

Fourth, a gray precipitate was produced in the final step, and the product was washed, filtered, and dried at room temperature for 4 days.

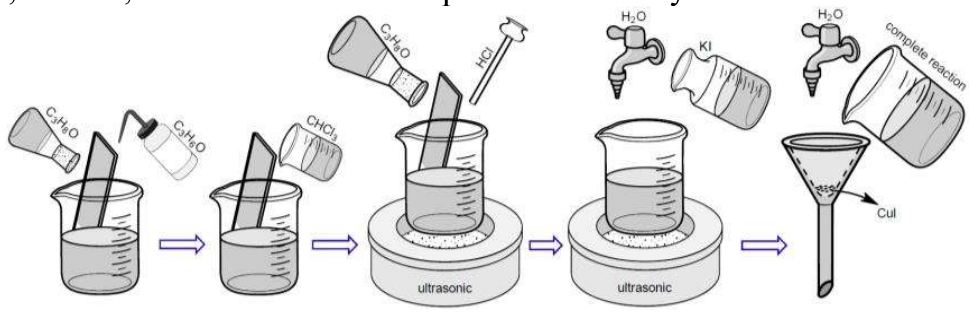

Fig. 3.27. Illustration of the synthesis method of CuI particles

The reagents were calcium nitrate tetrahydrate $Ca(NO_3)_2.4H_2O$ as a calcium ion source and diammonium hydrogen phosphate ($(NH_4)_2HPO_4$) as a phosphorus precursor. In addition, concentrated nitric acid (HNO_3) and sodium hydroxide (NaOH) were added, which played a role in the dispersion of particles, and copper iodide (CuI) was used as a dopant to prepare the CuI (5 mol%)/HA composite. In this procedure, nitric acid (HNO_3) and deionized water were added with the indicated amount of CuI, until the particles were completely dissolved and then heated until the crystallization occurred. The unique mole fraction of $I_2 + 2Cu(NO_3)_2$ was obtained, and after the dissolution of crystals, the mole fraction of CuI was 5 mol%. In the next step, according to the molar ratio of (Ca + CuI)/P = 1.67, $(NH_4)_2HPO_4$ was added dropwise to the mixture of $Ca(NO_3)_2.4H_2O$ and $I_2 + 2Cu(NO_3)_2$ (with stirring at 250 rpm), and pH of 14 was achieved by adding 2 $mol.l^{-1}$ NaOH at room temperature. The product was dried at 100 °C and 0.76 bar simultaneously, and after one day, the mixture was washed, filtered, and dried at 150 °C for 4 h. Finally, the compounds were calcined at 300 °C, 500 °C, 700 °C, and 900 °C for 2 h. The summary of the synthesis method of CuI (5 mol%)/HA is shown in Fig. 3.28, and the synthesis routes of CuI and CuI (5 mol%)/HA are shown in Fig. 3.29.

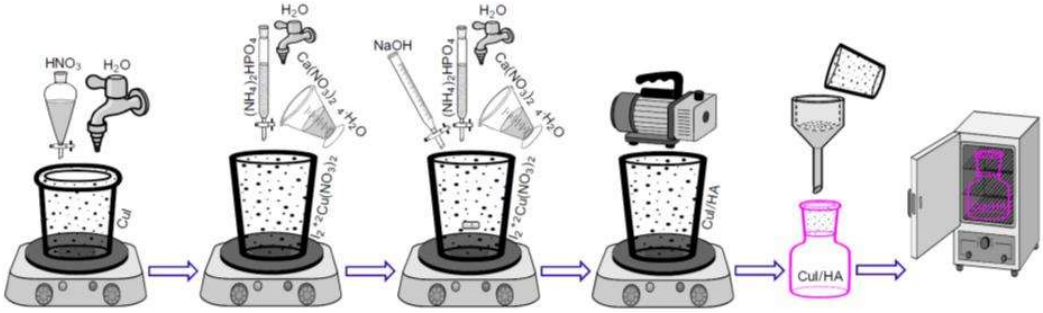

Fig. 3.28. Illustration of the synthesis method of CuI (5 mol%)/HA nanoparticles

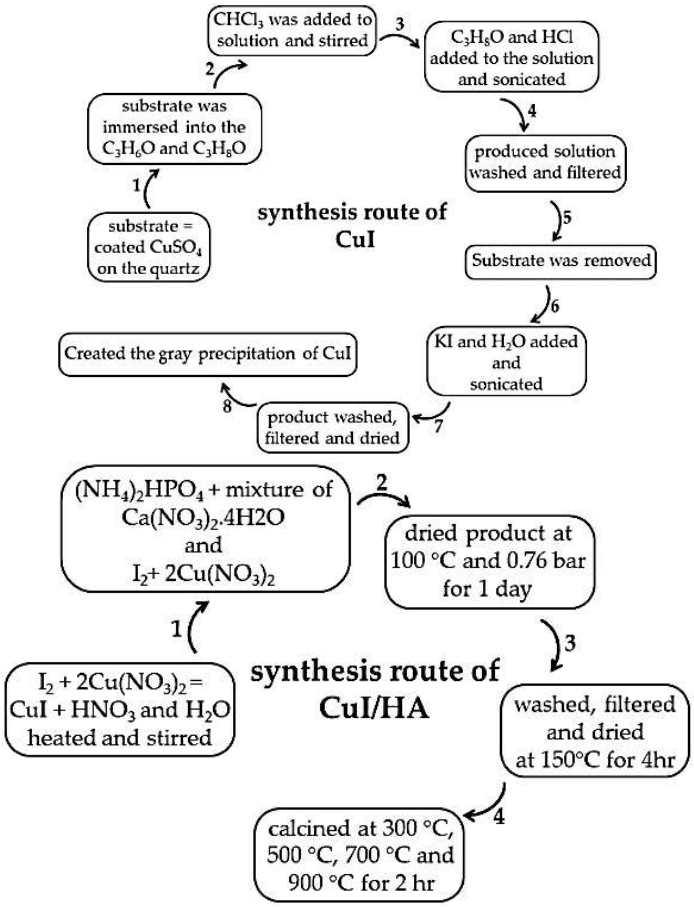

Fig. 3.29. The synthesis routes of CuI and CuI (5 mol%)/HA

The compression test at room temperature was used to investigate the mechanical properties. The relative rate of the jaw and the load cell values were 0.1 mm/min and 50 KN tandemly. The stress-strain curve of the composites and the powder compression system are shown in Fig. 3.30, and the values obtained by the mechanical test and the elasticity coefficient (slope of elastic surface) are listed in Table 3.11. The function of the elasticity coefficient is calculated by Equation 3.7.

$$E = \frac{\Delta\sigma}{\Delta\varepsilon} \text{ [70]} \qquad (3.7)$$

According to Equation 3.7, $\Delta\sigma$ and $\Delta\varepsilon$ were the difference values of two points in the elastic region. Moreover, in order to calculate the hardness values, a force of 300 g newton was applied, and the hardness was measured at five points; the results are shown in Table 3.12. The average value of micro hardness was in the range from 39.10 to 41.02 HV. The result of the compression test has shown that the calcination temperature of 900 °C led to an improvement in the mechanical test. At low calcination temperatures, the values of compression test and plasticity were decreased, which is related to the crystal size of the compounds, because the crystal size increased with increasing the intermetallic phase between Cu and I tandemly. Moreover, the value of elasticity coefficient was calculated for all compounds, and

the value was in the range from 3.11 to 4.68 GPa, and this range has more difference with natural HA [136].

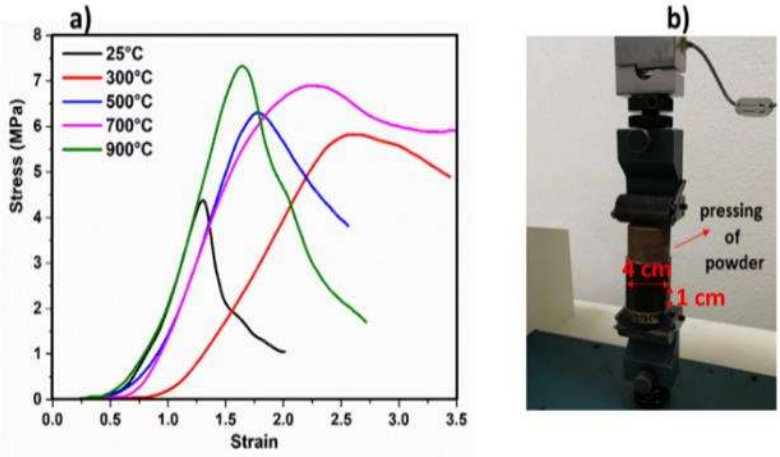

Fig. 3.30. (a) Compressive stress-strain curves of samples and (b) pressing of powder

Table 3.12. Values of σ_{yc} and ε extracted by compressive stress-strain curve of compounds

Compound	Hardness (HV)	E (GPa)	σ_{yc} (MPa)	ε in σ_{yc} (%)
25 °C	39.54	4.68	4.35	1.29
300 °C	39.21	3.89	5.83	2.59
500 °C	41.02	3.11	6.29	1.76
700 °C	39.10	4.09	6.89	2.22
900 °C	40.81	3.95	7.32	1.63

Digital speckle interferometry is one of the best-known methods for studying imperfections for nondestructive analysis. In this method, the application of force to the sample generates strain and stress distributions (interferometric lines) that can be interpreted. Typical strain values are often small in the range of micrometers. Therefore, the quality of the samples after mechanical formation was analyzed by utilizing the Speckle Pattern Interferometry (ESPI) (Fig. 3.31). In this measurement, a green light laser (532 nm) with 20 mW power was used. In Fig. 3.31, the object beam (3) illuminates the sample (5), and the scattered light is collected by the camera (2), where it interferes with the reference beam and the speckle pattern registered by the CCD sensor that is sent to the computer for further calculations. The speckle patterns are analyzed and visualized with the software PRISM VIZ.

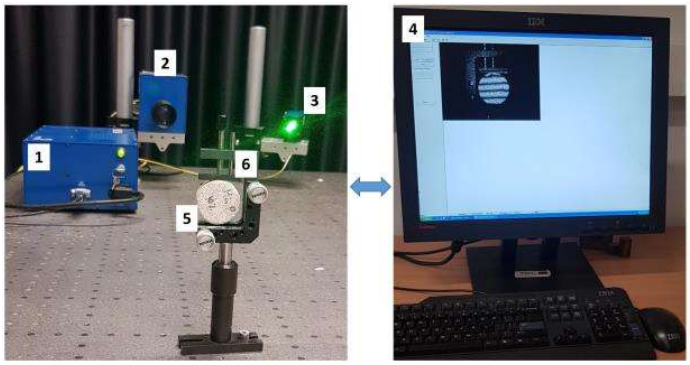

Fig. 3.31. Schematic configuration of speckle interferometry; the electronic speckle pattern interferometry system PRISM consists of: 1 – control block, 2 – video head, 3 – illumination head, 4 – monitor, 5 – specimen, 6 – holder

It is important to ensure the highest quality of samples, which depends on the distribution of material by volume, internal cracks, or air bubbles. The resulted images of the speckle pattern are shown in Fig. 3.32.

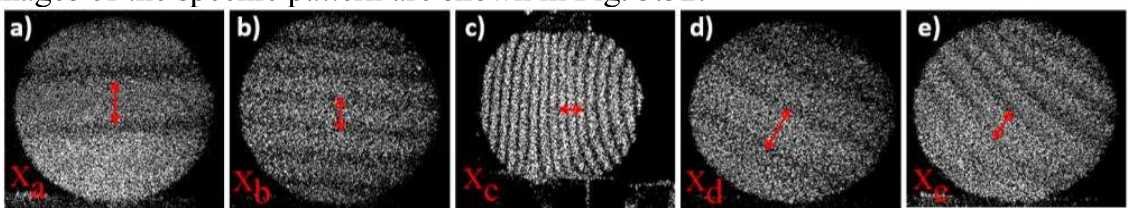

Fig. 3.32. Resulted speckle pattern interferometry images of specimens (a) CuI (5 mol%)/HA at 25 °C, calcined at (b) 300 °C, (c) 500 °C, (d) 700 °C, and (e) 900°C

According to Fig. 3.32, the samples deform uniformly under central loading, and there are no defects, while parallel oblique lines indicate non central loading. However, interferometric lines of the arbitrary shape can indicate the defects. These changes in the response of the sample to central loading are caused by defects. For example, air bubbles or cracks cause lower Young's modulus of the sample in some local zones. Therefore, concentric rings can be observed at these locations, which means higher deformation. In fact, whatever the interferometric lines are neared together and are denser, the size of the imperfection will increase [137, 138]. According to the interpretation and Fig. 3.32, the distances between the interferometric lines of the samples were evaluated, and as a result: $X_a > X_d > Xe \geq X_b > X_c$; therefore, the compound consisting of CuI (5 mol%)/HA at 25 °C and calcined at 700 °C has fewer imperfections than other compounds, and it is clear that the compound at calcination temperature of 700 °C has similar distributions of stress and strain as CuI (5 mol%)/HA at 25 °C. Nonetheless, this discussion relates directly to the surface of the samples, and the speckle interferometry is entirely focused on the surface. Furthermore, according to the speckle images, there are no significant imperfections, such as holes or cracks on the surface of the samples.

CONCLUSIONS

1. The new technique for calculating the crystallite size was introduced. HA was selected, which was obtained from cow, pig, and chicken bones. A comparison of different methods and models for calculating the nanocrystallite size of these bones was performed along with BET and TEM studies. The size of HA crystals in animal bones is of interest for both basic and applied sciences, e.g., doping of metals, bioglass, polymers, and composites, especially in the fabrication of implants. It has been found that:

1.1. The Modified Scherrer equation has the advantage of reducing errors and providing a more accurate value of the crystallite size from all or some of the different peaks.

1.2. The values of HA crystallite sizes were determined to be 60, 60, and 57 nm for cow, pig, and chicken, respectively.

1.3. The Modified Scherrer method is recommended for research and industrial applications due to its ease of use, a control point, the use of the least squares method for higher accuracy, and the setup of data with the experimental BET results.

2. A new method for measuring accurate value of the Young's modulus of crystalline materials is successfully presented, and it has been established that:

2.1. The planar density for the area of total atoms/ions in the plane divided by the area of the plane is responsible for the Young's modulus of that plane.

2.2. The Young's modulus of each plane (y-axis) is plotted against the planar density of that plane (x-axis), using the least squares method to obtain the Young's modulus of the materials at the intercept.

2.3. NaCl (commercially available) was chosen as an example to introduce a new technique for measuring Young's modulus, and as a result, the calculated value of Young's modulus agreed well with the value obtained by the ultrasonic technique.

2.4. The W–H method in the USDM model can be used to minimize the errors of the least squares method and obtain a correct Young's modulus, which is much more accurate than the average value.

2.5. The limitation is that the XRD data is applicable to the calculation of the uniform distribution of atoms in the crystal lattice with a unit cell; thus, the method cannot be used for amorphous materials.

3. A new approach to explore reliable Young's modulus quantity based on XRD is proposed for either single crystal or polycrystalline of $CaTiO_3$ as an example for cubic lattice. In this study, it should be noted that the discussion of scales does not refer to the expanded cells, and it has been determined that:

3.1. The Young's modulus values of $CaTiO_3$ extracted by planar density and least squares method were calculated to be 162.62 ± 0.4, 151.71 ± 0.4 and 152.21 ± 0.4 GPa for unit cell, super cells (2 × 2 × 2), and symmetry cells, respectively.

3.2. The Young's modulus value of $CaTiO_3$ reported by symmetry cells is in

good agreement with Young's modulus determined by the ultrasonic echo technique and literature.

3.3. A unit cell of $CaTiO_3$ is not representative of the distribution of atoms on the planes. In order to obtain the real value of planar density and find the symmetry of distribution of atoms on the planes, the expanded cells and use of symmetry cells are suggested.

3.4. The determination of the planar density values based on the unit cell or every super cells, except for (8 × 8 × 8), is an estimation.

3.5. The real value of Young's modulus of $CaTiO_3$ should be extracted from symmetry cells or super cells (8 × 8 × 8).

4. The W–H method in the USDM model for estimating more accurate values of stress-strain of unit cell and super cells (2 × 2 × 2) of HA was investigated. It has been found that:

4.1. According to this study, the slope of the elastic modules against planar density in super cells (2 × 2 × 2) was negative. The reason was related to the imperfections, and this means that when the density of atoms in the planes is increased, lower forces are required for the dislocation motion.

4.2. As a result, a plane without an atom is more realistic in a smaller area of the unit cell than a larger area of the super cells (2 × 2 × 2), and this means that the intercept of the unit cell is closer to the real values of the Young's modulus in the HA lattice.

4.3. Moreover, a comparison of the theoretical and experimental data of the Young's modulus of HA showed that there is a small difference between the values for both unit cell and super cells (2 × 2 × 2), namely 10.47 GPa and 10.57 GPa; this means that the theoretical calculation is valid, and the experimental value can be obtained by reducing it by about 10 GPa.

4.4. The Young's modulus values of HA in the unit cell and super cells (2 × 2 × 2) were 108.15 and 121.17 GPa, respectively.

5. The mechanochemical process was carried out to synthesize Ag-doped HA. Taking into account the DSC curve of the hair band and the slurry, the final sintering temperature was set at 350 °C, and a porous scaffold was prepared. The porosities were opened, which can be suitable to increase the ratio of biocompatibility. The doping mechanism, structural evolution, morphological properties, mechanical properties, and bioactivity analysis were studied by spectroscopic and microscopic techniques. It has been determined that:

5.1. A new approach to fabricate a porous scaffold by using hair band was carried out. In addition, the effects of Ag and PVTMS loading on the morphology of HA, phase compositions, and structural features were investigated.

5.2. The average porosity value was obtained at > 200 μm; thus, these values were suitable for sitting blood cells in these porosities, and the coefficient of bioactivity was enhanced.

5.3. PVTMS prevented from cracking and shrinkage of the scaffold, and the free radicals of PVTMS structure provided the flexibility of a scaffold by

bonding between C-C and siloxane (Si-O-Si); moreover, PVTMS prevented the collapse via carbon chains during the heat treatment.

5.4. The maximum value of compressive strength reached 15.71 MPa, and this value is valuable according to the Ag content and the absence of large amounts of metals.

6. The prepared composites, consisting of CuI (5 mol%)/HA, were very sensitive to the calcination temperature (from 25 °C to 900 °C). The main point of this work was to characterize CuI (5 mol%)-doped HA and improve the properties, especially mechanical properties. It has been determined that:

6.1. The stress-strain curves of the samples were depicted, and the maximum value of σ_{yc} was 7.32 MPa. Moreover, according to the extracted images by speckle interferometry analysis, the impressive imperfections were not observed on the surface of the specimens.

6.2. Finally, most of the properties increased with increasing calcination temperature, and the optimum point of calcination temperature reached 700 °C; furthermore, the CuI-doped HA was stabilized with almost no impurity phases present in the samples.

4. SANTRAUKA

Disertacija parašyta remiantis šešiais paskelbtais straipsniais. Pirmasis tyrimas yra susijęs su metodų palyginimu remiantis XRD modeliais kristalų dydžiui apskaičiuoti. Šiuo atveju buvo pateiktos hidroksiapatito (HA), gauto iš karvių, kiaulių ir vištų kaulų, XRD smailės, o kristalitų dydžio vertės buvo gautos XRD pagrįstais metodais. Palyginus visus metodus, Monshi-Scherrer'io metodas suteikė paprasto skaičiavimo galimybę ir sumažino paklaidą, taikant mažiausius kvadratus linijinėse diagramose, taip pat davė 60 nm, 60 nm ir 57 nm kristalitų dydžius atitinkamai karvės, kiaulės ir vištos kaulams. Antrajame tyrime pristatomas naujas kristalitinių medžiagų Youngo modulio gavimo metodas. Dirbant pagal šitą metodą, kristalitinių medžiagų Youngo modulis gaunamas taikant rentgeno spindulių difrakciją. Šiame tyrime Youngo modulio vertės gautos per pasirinktines plokštumas, tokias kaip atsitiktinės (*hkl*) tyrime. Youngo modulis apskaičiuojamas pagal santykį tarp tamprumo koeficientų, kristalinės gardelės geometrijos ir kiekvienos rentgeno spindulių difrakcijos plokštumos plotinio tankio. Šitas metodas įvestas naudojant plotinio tankio reikšmes kaip *X* ašį ir Youngo modulio reikšmes kaip *Y* ašį, kad ašinė atkarpa galėtų registruoti Youngo modulį dideliu tikslumu. Be to, kaip pavyzdys buvo pasirinktas natrio chloridas (NaCl) su FCC kristalo gardele, o Youngo NaCl modulio vertė buvo išmatuota 35,68 GPa. Trečiajame tyrime šis metodas taikomas perovskito gardelei ($CaTiO_3$), apskaičiuotas elementariųjų narvelių, supernarvelių (2×2×2) ir simetrijos narvelių Youngo modulis. Išskirtos Youngo modulio vertės buvo užregistruotos kaip 162,62, 151,71 ir 152,21 GPa elementariesiems narveliams, supernarveliams (2×2×2) ir simetrijos narveliams atitinkamai. Be to, apskaičiuota simetrijos narvelių Youngo modulio vertė gerai sutapo su eksperimentiniais metodais ir literatūros duomenimis. Ketvirtajame tyrime šis metodas buvo taikomas HA kaip šešiakampis elementariųjų narvelių ir supernarvelių (2×2×2) pavyzdys. Šiuo metodu išskirtos Youngo modulio vertės buvo atitinkamai 108,15 ir 121,17 GP elementariesiems narveliams ir supernarveliams (2×2×2). Penktajame tyrime plaukų raištis buvo pasirinktas kaip naujas būdas paruošti didelius ir atvirus nanokompozito, sudaryto iš Ag/HA/PVTMS, poringumus, nes šios porėtos vietos yra geriausios kraujo ląstelių branduolių susidarymo ir augimo vietos. Ištirtos paruoštų nanokompozitų fizinės, mechaninės bei bioaktyviosios savybės ir nustatyta maksimali gniuždymo stiprio vertė 15,71 MPa esant ~0,77 deformacijai. Šeštajame tyrime nanokompozitas, sudarytas iš 5 mol% kristaliniu CuI legiruoto HA, pirmą kartą buvo paruoštas paprastu cheminiu metodu ir kalcinuotas skirtingos temperatūros aplinkoje, pvz., 300 ◦C, 500 ◦C, 700 ◦C ir 900 ◦C atitinkamai. Šiame tyrime HA atliko matricos vaidmenį, o CuI buvo armatūra. Be to, šių nanokompozitų mechaninės savybės išsamiai aptartos taikant ASTM-E9 standartą, o CuI (5 mol%)/HA, kalcinuoto

900 ◦C temperatūroje, diapazonas buvo geresnis nei kitų junginių, o σ_{yc} ir kietumo vertės buvo apibrėžtos kaip 7,32 MPa ir 40,81 HV atitinkamai.

4.1. ĮVADAS

Hidroksiapatitas (HA) yra įvairių medžiagų kompleksas, kuris gali būti naudojamas biokompozitų gamybai. HA yra keramika, egzistuoja keletas dirbtinio HA paruošimo būdų, tokių kaip kietojo kūno reakcijos, mechanocheminis, sonocheminis, hidroterminis, zolio–gelio procesas ir nusodinimas. HA cheminė formulė yra ($Ca_{10}(PO_4)_6(OH)_2$), ir pastaruoju metu mokslininkai HA laikė potencialiu sunkiųjų metalų adsorbentu dėl didelio specifinio paviršiaus ploto, didelio terminio bei cheminio stabilumo ir didelės jonų mainų galimybės. Yra dvi HA kristalinės struktūros: 1) šešiakampė struktūra ir 2) monoklininė struktūra. Siekdami pagerinti HA savybes, mokslininkai Ca^{2+} jonus pakeitė kitų metalų jonais. HA struktūrą sudaro beveik kompaktiškas fosfatų grupių paketas su dviejų tipų Ca^{2+} jonais, su tokiomis kaip tunelinė ir lygiagreti padėtimis. Viena iš pagrindinių HA struktūros savybių yra daugybės pakeitimų galimybė, kuri nekeičia kristalografinės struktūros pagrindo. HA turi šešiakampę sistemą su $P6_3/m$ erdvine grupe ir mažai nukrypsta nuo stechiometrijos. Siekiant pagerinti HA keramikos mechanines savybes, plačiai ištirti įvairūs metodai, pvz., kompozitų gamyba ir mikrostruktūrų valdymas taikant naujus sukepinimo metodus arba naudojant nanostruktūrinius miltelius. Labiausiai besivystanti HA pritaikymo sritis – kaulų atkūrimui; nors HA biologiškai suderinamas, dėl savo trapumo jis neatitinka mechaninių reikalavimų kaulo pakaitalui; todėl dėmesys HA mechaninėms savybėms ir struktūrinei geometrijai gali būti naudingi moksliniams tyrimams, taip pat pramoniniam pritaikymui. Svarbu suprasti HA mechanines savybes sintezės procesų kristalizacijos ir augimo stadijose, nes Youngo modulis tiesiogiai veikia HA kristalo augimą mechaniškai įtemptose aplinkose. Taikant lengvą, ekonomišką ir patikimą Youngo modulio nustatymo metodą, būtina atkreipti dėmesį į HA struktūrinės geometrijos detales. Be to, tiriant HA struktūrinę geometriją, būtinas rentgeno spindulių difrakcijos tyrimas.

XRD profilio analizė yra patogus ir daug galimybių suteikiantis kristalito dydžio, gardelės deformacijos ir mechaninių savybių tyrimo metodas. Be to, rentgeno spindulių difrakcija yra įprasta medžiagų analizės procedūra. Taikant rentgeno spindulių difrakciją galima nustatyti medžiagų kristalų dydį, įtempį, deformaciją ir tankio energiją. Rentgeno spindulių modelių ir kristalografijos taikymas yra paprastas būdas nanokristalitų dydžiui apskaičiuoti.

Youngo modulis gali būti apibrėžtas kaip įtempio ir deformacijos santykis. Tamprumo konstantos yra būdingos kristalinės gardelės reakcijai prieš jėgas, nustatomai pagal tūrinį modulį, šlyties modulį, Youngo modulį ir Puasono

koeficientą. Tamprumo konstantos atlieka svarbų vaidmenį nustatant medžiagų stiprumą. Be to, tamprumo konstantos vertės koreliuoja su plotinio tankio vertėmis dėl gretimų atominių plokštumų ryšio charakteristikos ir ryšio bei struktūrinio stabilumo anizotropinio pobūdžio. Be to, tamprumo konstantos yra susijusios su įtempiais bei deformacijomis ir priklauso nuo kristalinės gardelės konfigūracijos, todėl tamprumo konstantos išvedamos iš kristalinės gardelės plokštumų ir lygiaverčių kristalografinių plokštumų, kurios turi panašų atominį plotinį tankį. Plotinis tankis yra viso kristalografinės plokštumos ploto dalis, kurią užima atomai. Tai svarbus kristalų struktūros parametras, jis nurodomas kaip atomų skaičius ploto vienete plokštumoje. Rentgeno spindulių difrakcija yra vienintelis metodas, leidžiantis nustatyti kiekvienos difrakcijos plokštumos mechanines ir mikrostruktūrines būsenas. Difrakcijos plokštumos naudojamos kaip deformacijos matuoklis matuojant Youngo modulį vienoje ar keliose difrakcijos vektoriaus plokštumose / kryptyse. Šiais laikais rentgeno spindulių difrakcija yra įprastas kristalinių struktūrų ir atomų tarpų tyrimo metodas. Rentgeno spindulių difrakcija pagrįsta monochrominių rentgeno spindulių ir kristalinio bandinio konstruktyvia interferencija. Hanabusa ir kt. pristatė naują plieno cementito fazės tamprumo konstantos matavimo metodą, tačiau šio metodo apribojimas susijęs su tuo, kad jį buvo galima taikyti tik aukštojo kampo srityse, o žemojo kampo srityse jo pritaikyti nepavyko. Priešingai, Williamson-Hall (W–H) metodas gerai tiko deformacijos skaičiavimui ir vertinimui. W–H metodu galima nustatyti gardelės deformaciją (ε), gardelės įtempį (σ) ir gardelės deformacijos energijos tankį (u). Tamprumo konstantos nurodomos pagal kristalinės gardelės deformaciją veikiant jėgai. Tokie tamprumo moduliai yra: Youngo modulis, šlyties modulis ir tūrinis modulis. Šie moduliai registruojami pagal būdingąsias medžiagų tamprumo savybes ir atsparumą apkrovos deformacijai. Medžiagų tamprumas apibūdinamas tokiais modeliais kaip Koši (Cauchy) tamprumas, hipotamprumas ir hipertamprumas. Hipertamprumas yra konstitucinis modelis idealiai tampriai medžiagai, kuri reaguoja į įtempių padidėjimą dėl deformacijos energijos tankio funkcijos, o hipotamprios medžiagos pagrindinė lygtis nepriklauso nuo baigtinio deformacijos kiekio, išskyrus tiesinę būseną. Tamprumo savybės yra glaudžiai susijusios su kristalų struktūra, vidiniu jungties tarp atomų pobūdžiu ir medžiagų anizotropine prigimtimi; todėl iš kristalinės gardelės skaičiavimų galima išvesti tamprumo konstantas. Mūsų tyrime pristatomas naujas kristalito dydžio ir Youngo modulio skaičiavimo bei matavimo metodas ir technologija. NaCl (FCC), $CaTiO_3$ (SC) ir HA (HCP) pateikiami kaip pavyzdžiai. Be to, išsamiai aptariama dviejų kompozitų, sudarytų iš CuI/HA ir Ag/PVTMS/HA, sintezė, fizinės ir mechaninės savybės.

Šio darbo tikslas – natūralaus ir dirbtinio hidroksiapatito (HA) ir HA pagrindu pagamintų nanokompozitų sintezė ir mechaninių savybių tyrimas, sukuriant naują

visapusišką nanokristalų dydžio analizės metodiką, Youngo modulį, pasižymintį dideliu tikslumu bei našumu visuose kristalito komponentuose ir taikant tyrimų rezultatus bioinžinerijoje.

Norint pasiekti darbo tikslą, suformuluojamos tokios užduotys.

1) Visų rentgeno spindulių difrakcijos metodų, skirtų natūralaus HA nanokristalų dydžiui apskaičiuoti, palyginimas.
2) Natūralaus HA nanokristalų dydžio tyrimas taikant rentgeno spindulių difrakciją.
3) Naujo metodo, skirto matuoti Youngo modulį kaip plotinio tankio funkciją kristalinių gardelių elementariajame narvelyje ir supernarvelyje, įvertinimas. Pavyzdžiui, Youngo modulio ir elementariųjų narvelių, supernarvelių (2×2×2) ir kubinių kristalinių gardelių, tokių kaip natrio chloridas (NaCl) ir perovskitas ($CaTiO_3$), simetrijos narvelių tankio tyrimas.
4) HA kaip šešiakampės gardelės elementariųjų narvelių ir supernarvelių įtempių deformacijų (2×2×2) įvertinimas ir W–H metodas vienodų įtempių deformacijos modelyje (USDM), gautame iš rentgeno spindulių difrakcijos.
5) Naujo bioaktyviojo nanokompozito, sudaryto iš Ag legiruoto HA ir poliviniltrimetoksisilano (PVTMS), paruošimas ir nanokompozito Ag legiruoto HA/PVTMS mechaninių savybių bei bioaktyvumo *in vitro* tyrimas.
6) Kalcinavimo temperatūros įtakos naujo nanokompozito, susidedančio iš HA/vario jodido (CuI), mechaninėms savybėms įvertinimas.

4.2. LITERATŪROS APŽVALGA

Atsižvelgdami į tai, kad organizme yra kalcio fosfatų (CaP), mokslininkai šiais laikais svarstė CaPs naudojimą pažeistiems kaulams pakeisti ir taisyti. Viena iš labiausiai pageidaujamų ir žinomiausių CaP grupių yra susijusi su hidroksiapatitu (HA) [42], [43]. Viena iš pagrindinių HA struktūros savybių yra daugybės pakeitimų galimybė, nekeičiant kristalografinės struktūros pagrindo. **4.1 pav.** parodyta šešiakampio HA elementariojo narvelio schema ir termiškai apdorojant susintetinto HA .cif failas. Yra dvi skirtingos kalcio jonų situacijos, iš viso 18 jonų glaudžiai supakuoti, kad būtų sukurta šešiakampė struktūra. Kiekviename šešiakampio kampe kalcio joną riboja 12 kalcio jonų, bendrų 3 šešiakampiams. Tuščios erdvės tarp dviejų šešiakampių yra užpildytos trimis fosfatų tetraedrais viename elementariajame narvelyje. HA esantys jonai gali būti pakaitomis pakeisti biologiškai naudingais jonais dėl būdingo šios kristalinės struktūros universalumo, ir tai taip pat gali būti vadinama legiravimu. Be to, galimas kalcio, fosfato ir (arba) hidroksilo jonų pakeitimas [44]. Pažymėtina, kad specifinė HA savybė yra susijusi

su OH^- jonais, formuojančiais vidinius kanalus išilgai *c* ašies. Ši savybė atlieka svarbų vaidmenį mechaninėse ir fizinėse savybėse [45].

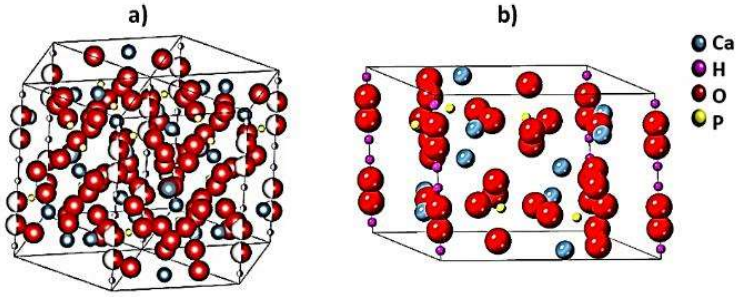

4.1 pav. Scheminis **(a)** HA elementariojo narvelio ir **(b)** HA struktūros, išgautos .cif failu, vaizdavimas [8]

Vienas iš iššūkių naudojant HA kaip bioaktyvųjį komponentą yra susijęs su infekcijos tikimybe; todėl antibakterinių medžiagų naudojimas yra geriausias būdas išspręsti šią problemą [46]. Kita vertus, tyrimais įrodyta, kad sidabras (Ag) turi antibakterinių savybių [47], [48]. Be to, Ag yra vienas geriausią biologinį suderinamumą turinčių elementų, nes jis susijęs su didele antibakterinio koeficiento verte (100 %) [49], [50]. Tačiau Ag biologinio suderinamumo savybės tiesiogiai priklauso nuo bioaktyviųjų kompozitų stiprumo, tankio ir pagamintos galutinės fazės. Yra keletas mechanizmų, kurie įtraukia Ag į sąveiką su biologinėmis makromolekulėmis [51]. Be to, įrodyta, kad Ag+ jungiasi su baltymų funkcinėmis grupėmis, todėl vyksta baltymų denatūracija [52]. Poliviniltrimetoksisilanas (PVTMS) turi funkcinę grupę, tokią kaip silanolis (Si-O-H), kuri gali padėti surišti; todėl jis naudingas siekiant užkirsti kelią kompozitų skilimui [53]. PVTMS yra rūšis polisiloksano pagrindu pagamintų komponentų, kurie ypač įdomūs dėl savo tankios siloksano struktūros, susietos su polimerinėmis grupėmis, be to, PVTMS yra biologiškai aktyvus ir pagerina mechanines savybes, suteikdamas stabilų Si-O-Si karkasą [54].

Vario jodido (CuI) tyrimai labai įdomūs, nes turi keletą privalumų, susijusių su tokiomis savybėmis kaip platus didelės juostos tarpas, jautrumas šviesai, diamagnetizmas, kaip dažiklis saulės elementuose ir superjoninis laidininkas [55], [56]. Keletas metalų, pvz., Ag^+, Sr^{2+}, Mn^{2+} ir Fe^{3+} su skirtingais masės procentais buvo naudojami HA legiravimui skirtingais metodais, o savybių vertinimai pateikti nuorodose [57], [58], [59], [60]. Be to, Renaudin ir kt. tyrimuose Cu^{2+} legiruotas HA buvo paruoštas zolio–gelio metodu [61]. Remiantis eksperimentiniais stebėjimais, neginčijama, kad Cu^{2+} legiruota HA struktūra sudaro ryšius, o Cu^{2+} katijonai yra išdėstyti išilgai kristalografinių hidroksilo vietų, formuojant linijinius O-Cu-O vienetus. Vėlesni tyrimai su variu parodė reikšmingus panašumus ir taip pat

atskleidė specifinę elgseną. Be to, didesnį legiravimo lygį galima pasiekti redukavus Cu^{2+} iki Cu^{+}, tačiau tam reikia aukštesnės sukepinimo temperatūros [62], [63], [64].

Uwe Holzwarth ir Neil Gibson paskelbė, kad Scherrerio lygtis yra susijusi su staigia rentgeno spindulių difrakcijos smaile. Lygtyje buvo įvestas apatinis indeksas (*hkl*), nes ji susijusi tik su viena smaile. Svarbu pažymėti, kad Scherrerio lygtis gali būti naudojama tik vidutiniams dydžiams iki maždaug 100 nm. Tai priklauso nuo instrumento, taip pat nuo signalo ir mėginio ryšio su kriterijaus triukšmu, nes, didėjant kristalito dydžiui, difrakcijos smailės išplėtimas mažėja. Gali būti labai sunku išskirti ir atskirti išsiplėtimą dėl kristalito dydžio nuo išsiplėtimo dėl kitų parametrų ir veiksnių. Klaidų visada yra, o sėkmingi skaičiavimo metodai gali sumažinti klaidas geriausiu įmanomu būdu ir leidžia gauti tikslesnius duomenis. Nanodalelių, išgautų XRD modeliais, dydžio apskaičiuoti neįmanoma, nes dalelėje yra keli nano- arba mikroskopinio dydžio kristalai. Rentgeno spinduliai gali prasiskverbti per kristalą, kad būtų gauta informacija, todėl dydžio apskaičiavimas susijęs ne su dalelėmis, o su kristalais. Scherrerio lygtis yra susijusi su difrakcijos smaile, pateikta **4.1 lygtyje** [65]; čia L – nanokristalo dydis; K – formos koeficientas, paprastai laikomas 0,89 keraminėms medžiagoms; λ – spinduliuotės bangos ilgis nanometrais ($\lambda_{Cu K\alpha}$ = 0,15405 nm); Θ – smailės difrakcinis kampas; β – visas smailės plotis radianais ties puse maksimumo (FWHM). Be to, smailių išplėtimas yra susijęs su fiziniu ir instrumentiniu išplėtimu [66], [67].

$$L=\frac{K\lambda}{\beta}.\frac{1}{\cos\theta} \qquad (4.1).$$

Norint sumažinti šią instrumento paklaidą, galima naudoti **4.2 lygtį**:

$$\beta_d^2 = \beta_m^2 - \beta_i^2 \qquad (4.2).$$

Šioje formulėje β_m – išmatuotas išplėtimas, β_i – instrumentinis išplėtimas, o β_d įvedamas kaip pataisytas išplėtimas, atsakingas už kristalo dydį. Instrumentinis išplėtimas bei fizinis mėginio išplėtimas, išmatuotas per visą plotį iki pusės maksimumo (FWHM), ir fizinio išplėtimo korekcija leidžia apskaičiuoti kristalo dydį pagal Scherrerio lygtį, kaip aprašyta [68], [69] nuorodoje. Yra keletas publikacijų, kuriose Scherrerio lygtis buvo apskaičiuojama tik ryškiausiai smailei, neatsižvelgiant į visų smailių skaičiavimus.

Huko dėsnis parodytas **4.3 lygtyje**; įtempis atitinka deformaciją esant mažiems poslinkiams. Tai yra pagrindinė forma, kai ši simetrija gali būti konvertuojama į šešis σ ir ε elementus [70].

$$\begin{pmatrix}\sigma_{xx}\\ \sigma_{yy}\\ \sigma_{zz}\\ \sigma_{yz}\\ \sigma_{zx}\\ \sigma_{xy}\end{pmatrix}=\begin{pmatrix}c_{11}\,c_{12}\,c_{13}\,c_{14}\,c_{15}\,c_{16}\\ c_{21}\,c_{22}\,c_{23}\,c_{24}\,c_{25}\,c_{26}\\ C_{31}C_{32}C_{33}C_{34}C_{35}C_{36}\\ C_{41}C_{42}C_{43}C_{44}C_{45}C_{46}\\ C_{51}C_{52}C_{53}C_{54}C_{55}C_{56}\\ C_{61}C_{62}C_{63}C_{64}C_{65}C_{66}\end{pmatrix}=\begin{pmatrix}\varepsilon_{xx}\\ \varepsilon_{yy}\\ \varepsilon_{zz}\\ \varepsilon_{yz}\\ \varepsilon_{zx}\\ \varepsilon_{xy}\end{pmatrix} \quad (4.3).$$

Be to, Huko dėsnį galima užrašyti kaip **(4.4 lygtis)**:

$$\begin{aligned}\sigma_{xx} &= C_{11}\varepsilon_{xx}+C_{12}\varepsilon_{yy}+C_{13}\varepsilon_{zz}+C_{14}\varepsilon_{yz}+C_{15}\varepsilon_{zx}+C_{16}\varepsilon_{xy},\\ \sigma_{yy} &= C_{21}\varepsilon_{xx}+C_{22}\varepsilon_{yy}+C_{23}\varepsilon_{zz}+C_{24}\varepsilon_{yz}+C_{25}\varepsilon_{zx}+C_{26}\varepsilon_{xy},\\ \sigma_{zz} &= C_{31}\varepsilon_{xx}+C_{32}\varepsilon_{yy}+C_{33}\varepsilon_{zz}+C_{34}\varepsilon_{yz}+C_{35}\varepsilon_{zx}+C_{36}, \quad (4.4).\\ \sigma_{yz} &= C_{41}\varepsilon_{xx}+C_{42}\varepsilon_{yy}+C_{43}\varepsilon_{zz}+C_{44}\varepsilon_{yz}+C_{45}\varepsilon_{zx}+C_{46}\varepsilon_{xy},\\ \sigma_{zx} &= C_{51}\varepsilon_{xx}+C_{52}\varepsilon_{yy}+C_{53}\varepsilon_{zz}+C_{54}\varepsilon_{yz}+C_{55}\varepsilon_{zx}+C_{56}\varepsilon_{xy},\\ \sigma_{xy} &= C_{61}\varepsilon_{xx}+C_{62}\varepsilon_{yy}+C_{63}\varepsilon_{zz}+C_{64}\varepsilon_{yz}+C_{65}\varepsilon_{zx}+C_{66}\varepsilon_{xy}.\end{aligned}$$

Tamprusis standis lemia kristalo reakciją į išorinį įtempimą ar deformaciją ir suteikia informacijos apie sukibimo charakteristikas, mechaninį ir struktūrinį stabilumą [71]. HA sistema turi penkias tamprumo konstantas (**4.5 lygtis**). Todėl penkių nepriklausomų (tampriojo standumo konstanta C_{ij}) reikšmės gali būti pavadintos C_{11}, C_{12}, C_{13}, C_{33}, C_{44}.

Hidroksiapatito matrica $$\begin{vmatrix}C_{11} & C_{12} & C_{13} & 0 & 0 & 0\\ C_{12} & C_{11} & C_{13} & 0 & 0 & 0\\ C_{13} & C_{13} & C_{33} & 0 & 0 & 0\\ 0 & 0 & 0 & C_{44} & 0 & 0\\ 0 & 0 & 0 & 0 & C_{44} & 0\\ 0 & 0 & 0 & 0 & 0 & \frac{1}{2}(C_{11}-C_{12})\end{vmatrix} \quad (4.5).$$

Įprastoms šešiakampėms sistemoms, tokioms kaip HA, ryšys tarp C_{ij} ir (tamprumo koeficientų S_{ij}) pateikiamas **(4.6–4.16)** lygtyse [72], [72].

$$S_{11}=\frac{1}{2}\left(\frac{C_{33}}{C_{33}(C_{11}+C_{12})-2(C_{13})^2}+\frac{1}{C_{11}-C_{12}}\right) \quad (4.6);$$

$$S_{12}=\frac{1}{2}\left(\frac{C_{33}}{C_{33}(C_{11}+C_{12})-2(C_{13})^2}-\frac{1}{C_{11}-C_{12}}\right) \quad (4.7);$$

$$S_{33}=\frac{C_{11}+C_{12}}{C_{33}(C_{11}+C_{12})-2(C_{13})^2} \quad (4.8);$$

$$S_{13} = -\frac{C_{13}}{C_{33}(C_{11}+C_{12})-2(C_{13})^2} \quad (4.9);$$

$$S_{44} = \frac{1}{C_{44}} \quad (4.10).$$

Pagal **4.6–4.10 lygtis**, norint gauti *S* reikšmes, reikia *C* reikšmių. Visas penkių verčių C_{11}, C_{12}, C_{13}, C_{33} ir C_{44} rinkinys buvo rastas ultragarsu matuojant fazės greičio anizotropiją. Šiose lygtyse ρ ir V yra atitinkamai bandinio tankis ir greitis [73], [74], [75].

$$C_{11} = \rho V_{1/1}^2,\ C_{22} = \rho V_{2/2}^2 \quad (4.11);$$

$$C_{66} = \rho V_{1/2}^2 = \rho V_{2/1}^2,\ C_{55} = \rho V_{1/3}^2 = \rho V_{3/1}^2 \quad (4.12);$$

$$C_{12} = \sqrt{(C_{11} + C_{66} - 2\rho V_{12/12}^2)(C_{22} + C_{66} - 2\rho V_{12/12}^2)} - C_{66} \quad (4.13);$$

$$C_{44} = \rho V_{2/3}^2 = \rho V_{3/2}^2 \quad (4.14);$$

$$C_{13} = \sqrt{(C_{11} + C_{55} - 2\rho V_{13/13}^2)(C_{33} + C_{55} - 2\rho V_{13/13}^2)} - C_{55} \quad (4.15);$$

$$C_{33} = \rho V_{3/3}^2 \quad (4.16).$$

Greičiams matuoti pagal [76] nuorodą buvo atliktas standartinis ultragarsinis impulsų aidas ASTM E797/E797-M-15. Atitinkamai, šlyties modulis yra proporcingas Burgers vektoriui ir Youngo moduliui; be to, dislokacijos tankis atitinka Youngo modulį [77], [78]. Ultragarso metodu Youngo modulio reikšmei matuoti naudotos išilginės ir skersinės bangos [79], [80]. Šiuo metodu (**4.17 lygtis**), remiantis ultragarso bangų greičiu ir mėginio tankiu, buvo nustatyta Youngo modulio reikšmė.

$$E = \frac{\rho c_l^2[3(\frac{c_l}{c_t})^2-4]}{(\frac{c_l}{c_t})^2-1} \quad (4.17).$$

1.17 lygtyje ρ, c_l ir c_t yra atitinkamai tankis, išilginių ir skersinių ultragarso bangų greitis. Be to, pagal **1.18 lygtį** išilginių ir skersinių bangų greitis gali būti registruojamas nustatant bandinio ilgį ir skirtumus tarp dviejų signalų aidų ($t = t_2 - t_1$) [81].

$$c = \frac{2L}{t} \quad (4.18).$$

Čia L – mėginio ilgis, t – skirtumas tarp dviejų aidų, o mėginio tankį galima nustatyti išmatavus mėginio masę ir tūrį [36]. Be to, pakeitus **1.17** ir **1.18 lygtis**, pagrindinė Youngo modulio skaičiavimo lygtis įvedama kaip **1.19 lygtis** [82].

$$E = \frac{4\rho\left(\frac{L}{t_s}\right)^2 (3t_s^2 - 4t_l^2)}{t_s^2 - t_l^2} \quad (4.19).$$

4.3. PATEIKTŲ STRAIPSNIŲ APŽVALGA IR DISKUSIJA

4.3.1. Natūralaus hidroksiapatito nanokristalų dydžio skaičiavimo metodų palyginimas naudojant rentgeno spindulių difrakciją (mokslinė publikacija nr. 1, Q1, 67 citata)

Šis skyrius parengtas remiantis straipsniu, paskelbtu *Nanomaterials*, **2020**, *10*, 1–21[44]. 1) Buvo paruošti karvių, kiaulių ir vištų šlaunikauliai. Pirmiausia galvijų kaulai buvo atskirti ir virinami karštame vandenyje, o tada 2 valandoms panardinami į acetoną, kad būtų pašalintas kolagenas ir riebalai (1 veiksmas, **4.2 pav.**). Atliekant 2 veiksmą kaulai buvo nuplauti distiliuotu vandeniu ir du kartus išdžiovinti. Tada kaulai atskirais žingsniais buvo dedami į krosnį aplinkos sąlygomis, o temperatūros didinimo greitis buvo 10 °C/min. Galiausiai kaulai buvo kaitinami 950 °C temperatūroje 2 valandas ir labai lėtai atšaldomi krosnyje. Po šio proceso pirmieji juodai išdeginti kaulai (dėl anglies išsiskyrimo) pavirto į baltą granuliuotą masę. Be to, kaulai buvo transformuoti į visiškai kristalizuotą HA 950 °C temperatūroje (3 veiksmas) [45]. Iš karvių, kiaulių ir vištų kaulų išgautas HA buvo patalpintas į planetinį rutulinį malūną su dubeniu (iš volframo karbido) ir rutuliukais, kad po terminio apdorojimo būtų sudarytos smulkios dalelės. Tiekimo santykis buvo 30 g miltelių ir 300 g rutuliukų (masės santykis 1 : 10), greitis nustatytas ties 250 aps./min., o malimo laikas nustatytas 2 val. su pauzės ir atbulinės eigos režimais (4 veiksmas) pagal procedūrą, aprašytą literatūroje [46], [47]. HA gamybos eigos vaizdai pateikti **4.2 pav.**

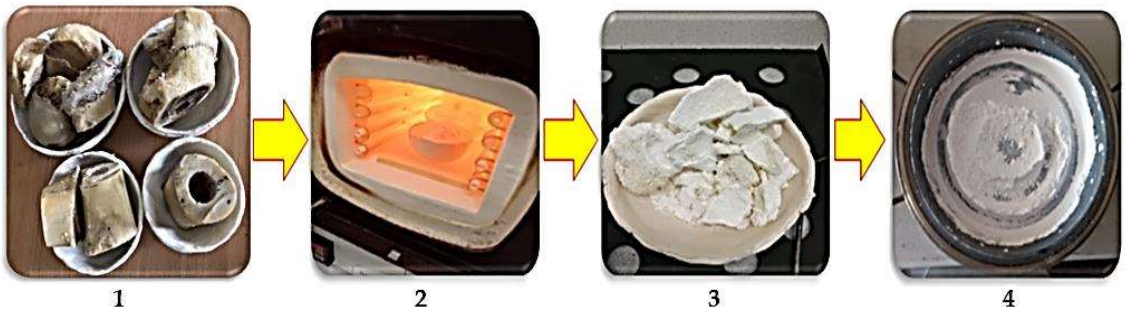

4.2 pav. HA gamybos iš karvių, kiaulių ir vištų kaulų eigos vaizdai (1–4 žingsniai)

Remiantis XRD modeliais **(4.3 pav.)**, pastebėta, kad HA mėginių kristalizacija buvo beveik panaši. XRD modelis rodomas kampais tarp $20° < 2\theta < 50°$.

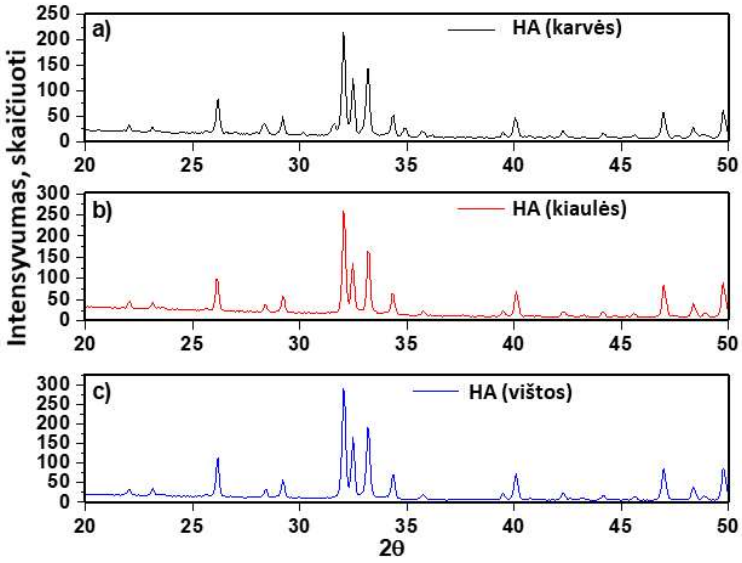

4.3 pav. HA XRD modeliai, gauti iš (**a**) karvės, (**b**) kiaulės ir (**c**) vištos kaulų

Lnβ lyginant su ln(1/cosΘ) parodyta **4.4 pav.** diagramose kartu su tiesinių mažiausiųjų kvadratų lygčių metodu, gautu iš tiesinės duomenų regresijos diagramose. Kristalų dydžiui pagal Monshi-Scherrerio lygtį nustatyti naudojama **4.20 lygtis**. Dirbant su *X'Pert* programine įranga, geriau kurti ir naudoti smailių duomenų .asc failą (su priesaga .asc) ir gauti smailių sąrašą, įskaitant FWHM, kuris yra susijęs su tinkamumo profilio piktograma (dešiniuoju pelės mygtuku spustelėkite smailę ir pasirinkite tinkamumo profilį X'Pert programinėje įrangoje), kad būtų sukurtas visiškas tinkamumas ieškant β (FWHM).

$$\frac{K\lambda}{L} = e^{(\text{intercept})} \qquad (4.20).$$

Tiesinės HA lygtys, gautos iš karvės, kiaulės ir vištos, užregistruotos atitinkamai $y = 2{,}7055x - 6{,}0921$, $y = 1{,}5815x - 6{,}0826$, ir $y = 2{,}7184x - 6{,}0285$, o ašinės atkarpos vertės kartu buvo −6,0921 karvių, −6,0826 kiaulių, ir −6,0285 vištų. Nepaisant to, ašinės atkarpos buvo apskaičiuotos atitinkamai $e^{(-6{,}0921)} = 0{,}00227$, $e^{(-6{,}0826)} = 0{,}00228$, ir $e^{(-6{,}0285)} = 0{,}00240$. Todėl $\frac{K\lambda}{L} = 0{,}00227$, $\frac{K\lambda}{L} = 0{,}00228$ ir $\frac{K\lambda}{L} = 0{,}00240$ atitinkamai karvėms, kiaulėms ir vištoms. Atlikus skaičiavimus, buvo gautos atitinkamai 60, 60 ir 57 nm kristalų dydžių reikšmės karvėms, kiaulėms ir vištoms.

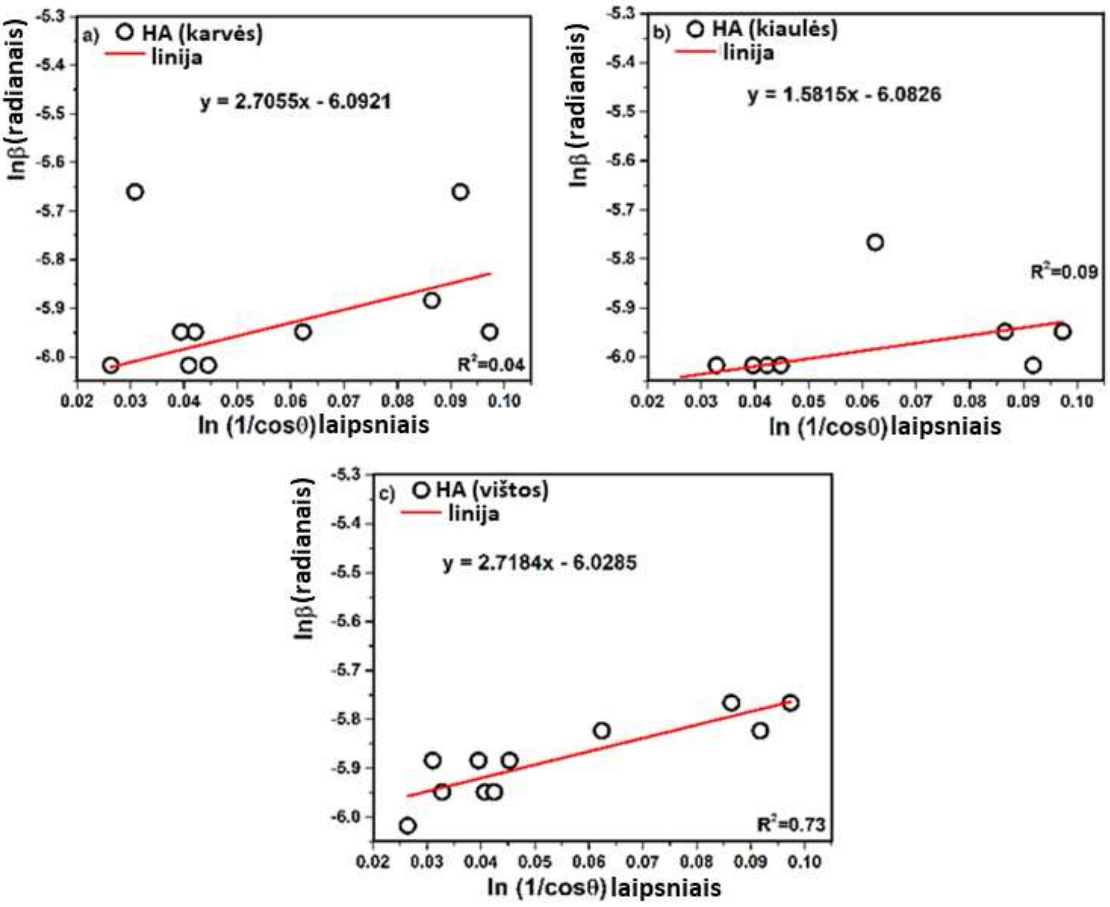

4.4 pav. Modifikuotos Scherrerio lygties linijinės diagramos ir skirtingos ašinės atkarpos HA, gautos (**a**) karvės, (**b**) kiaulės ir (**c**) vištos kaulams

4.3.2. Tamprumo modulio, susijusio su plokštumų atominiu tankiu kristalinių gardelių elementariajame narvelyje matavimas (mokslinė publikacija nr. 2, Q1, 15 citata)

Šis skyrius yra pagrįstas straipsniu, paskelbtu *Journal of Materials*, **2020**, *13*, 1–17 [30]. Šiuo atveju buvo atliktas kristalitinių medžiagų rentgeno spinduliuotės difrakcijos derinimas su kiekvienos difrakcijos plokštumos plotiniu tankiu. Galima tiksliai nustatyti kiekvienos kietos kristalitinės medžiagos Youngo modulio vertę. Junginiui *x* (milteliai / kristalinis bandinys) pasirinktas scheminis XRD modelis (**4.5 pav.**). Manoma, kad šie kristalitai yra atsitiktinai orientuoti vienas į kitą. Be to, jei milteliai dedami į monochrominės rentgeno spinduliuotės kelią, difrakcija atsiras nuo plokštumų tuose kristalituose, kurie yra orientuoti tinkamu kampu, kad būtų įvykdyta Braggo sąlyga. Norint labai tiksliai sekti įgyjamą Youngo modulio vertę, reikalingos tampriojo standumo konstantos vertės (C_{ij}) ir tamprumo koeficiento vertės (S_{ij}).

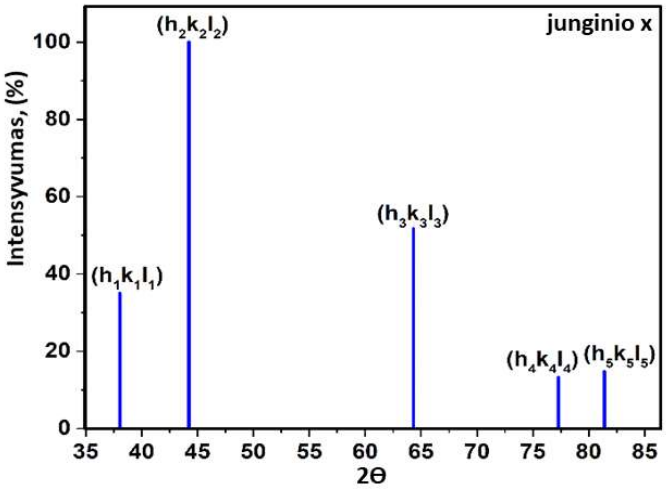

4.5 pav. *x* junginio rentgeno spindulių difrakcija

Youngo modulio vertė, išskirta iš kiekvienos junginio *x* plokštumos, palyginti su plotiniu tankiu, pateikta **4.6 pav**.

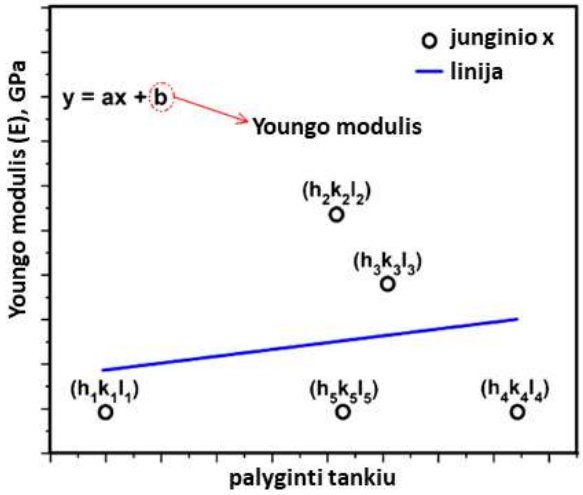

4.6 pav. Youngo modulis, išskirtas iš junginio *x* plokštumų, palyginti su plotiniu tankiu

Taikant šį metodą, Youngo modulio vienetas priklauso nuo tampriojo standumo konstantos vieneto ir tamprumo koeficiento verčių, o čia jis yra GPa. Be to, plotinio tankio reikšmė visada yra mažesnė už 1. Be to, plotinio tankio reikšmės priklauso nuo plokštumų padėties. Pavyzdžiui, šioje kreivėje (**4.6 pav.**) junginiui *x* $PD_{(h_4k_4l_4)} > PD_{(h_3k_3l_3)} > PD_{(h_5k_5l_5)} > PD_{(h_2k_2l_2)} > PD_{(h_1k_1l_1)}$. Be to, gali būti, kad dvi ar daugiau plokštumų turi panašias plotinio tankio vertes.

Kai taikomas šis metodas, skaičiuojant neatsižvelgiama į tuščias plokštumas viename elementariajame narvelyje. Tačiau jei elementariojo narvelio viduje esančioje plokštumoje nėra atomo, jie atsiras, kai plokštuma bus išplėsta į gretimus narvelius; atsiras atomai, elementarusis narvelis bus konvertuotas į supernarvelį, o

plotinį tankį galima apskaičiuoti remiantis dviem arba daugiau gretimų elementariųjų narvelių arba supernarvelių.

4.3.3. Ryšys tarp Youngo modulio ir elementariojo narvelio plotinio tankio, supernarvelių (2×2×2), perovskito simetrijos narvelių ($CaTiO_3$) gardelės (mokslinė publikacija nr. 3, Q1, 5 citata)

Šis skyrius pagrįstas straipsniu, paskelbtu *Journal of Materials*, **2021**, *14*, 1–15 [42]. Kalcio titanatas ($CaTiO_3$) buvo susintetintas solvoterminiu metodu kaip dar vienas kubinės gardelės pavyzdys. $CaTiO_3$ XRD modelis pateiktas **4.7 pav**. Būdingos $CaTiO_3$ smailės atitinka [60] nuorodoje pateiktą ataskaitą. $CaTiO_3$ kristalinė struktūra yra kubinė, Ti atominės padėtys yra ties (000), Ca ties $(\frac{1}{2},\frac{1}{2},\frac{1}{2})$ ir O ties $(\frac{1}{2},0,0)$, $(0,\frac{1}{2},0)$, $(0,0,\frac{1}{2})$. Remiantis rentgeno miltelinės difrakcijos rezultatais, gardelės parametras yra 3,79 ± 0,02 Å, o tai gerai atitinka [61] nuorodoje įrašytą vertę.

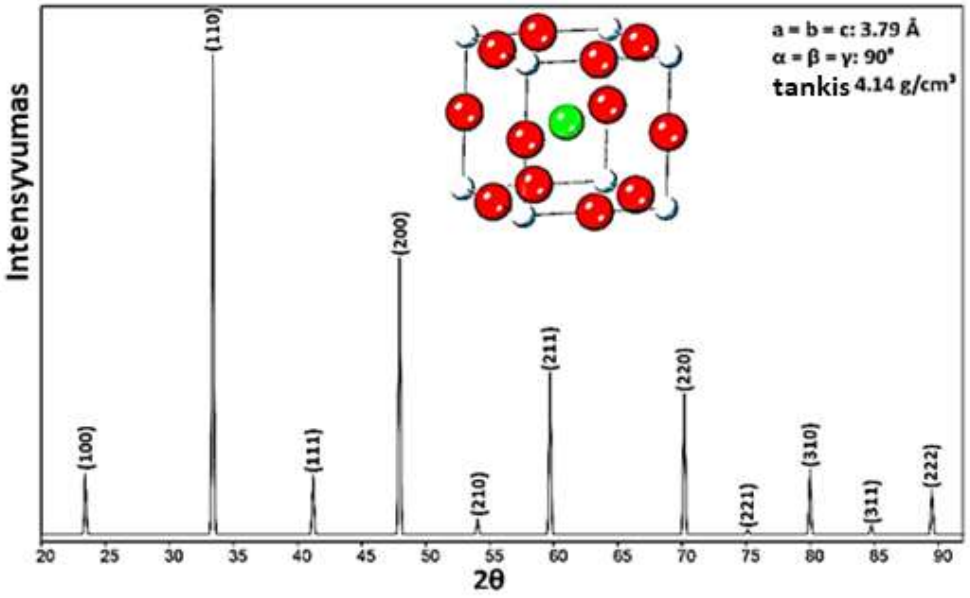

4.7 pav. $CaTiO_3$ (miltelių bandinio) rentgeno difrakcija

Norint įvertinti narvelius kaip rezultatus, pateikiami išsamūs $CaTiO_3$ gardelės elementariojo narvelio, supernarvelių (2×2×2) ir supernarvelių (8×8×8) difrakcijos plokštumų tankio skaičiavimai. Pavyzdžiui, (211) supernarvelių (4×4×4) ir (211) supernarvelių (8×8×8) plotinio tankio reikšmių geometrija ir skaičiavimai pavaizduoti **4.8 pav.**

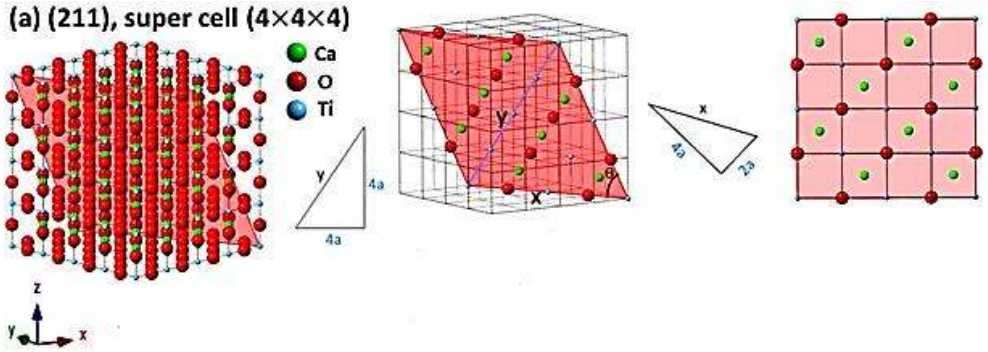

Atomų skaičius plokštumoje (211) × Kiekvieno atomo plotas plokštumoje (211)=

$$\left[\left(2\times\frac{78.52}{360}+2\times\frac{101.48}{360}+4\times\frac{1}{2}+5\right)\times\pi\left(r_{Ti^{4+}}\right)^2\right)+\left(\left(8\times\frac{1}{2}+4\right)\times\pi\left(r_{O^{2-}}\right)^2\right)\Big]+\left[\left(8\times\pi\left(r_{Ca+}\right)^2\right)\right]=$$

$$\left[(8\times\pi\,(0.60)^2)+(8\times\pi\,(1.40)^2)+(8\times\pi\,(1)^2)\right]=83.44$$

$$\text{Plokštuminis tankis}=\frac{\text{Atomų skaičius plokštumoje (211)}\times\text{Kiekvieno atomo plotas plokštumoje (211)}}{\text{plotas plokštumoje}}=\frac{83.44}{334.1}=0.25$$

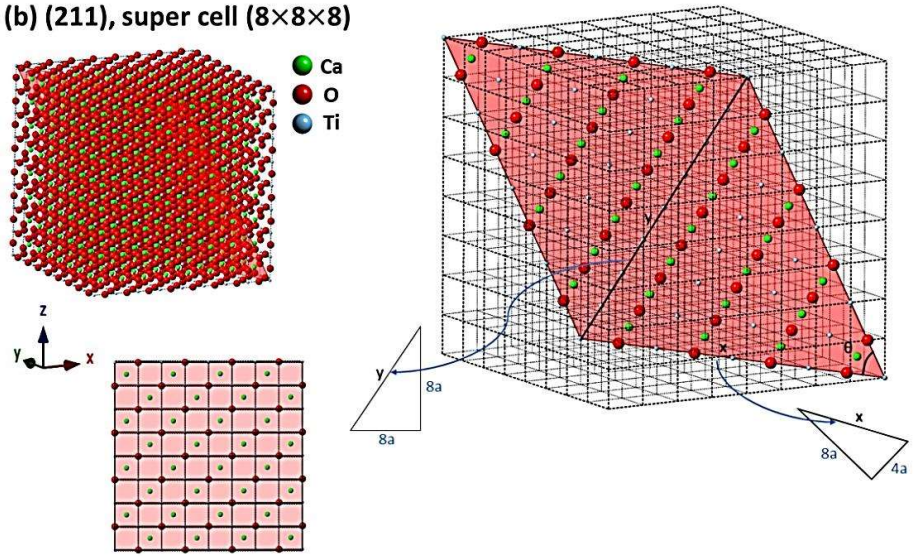

Atomų skaičius plokštumoje (211) × Kiekvieno atomo plotas plokštumoje (211)=

$$\left[\left(2\times\frac{78.52}{360}+2\times\frac{101.48}{360}+12\times\frac{1}{2}+25\right)\times\pi\left(r_{Ti^{4+}}\right)^2\right)+\left(\left(16\times\frac{1}{2}+24\right)\times\pi\left(r_{O^{2-}}\right)^2\right)\Big]+\left[\left(32\times\pi\left(r_{Ca+}\right)^2\right)\right]=$$

$$\left[(32\times\pi\,(0.60)^2)+(32\times\pi\,(1.40)^2)+(32\times\pi\,(1)^2)\right]=333.76$$

$$\text{Plokštuminis tankis}=\frac{\text{Atomų skaičius plokštumoje (211)}\times\text{Kiekvieno atomo plotas plokštumoje (211)}}{\text{plotas plokštumoje}}=\frac{333.76}{1335.24}=0.25$$

4.8 pav. Plokštumų geometrija ir plotinio tankio skaičiavimai:
(**a**) (211) supernarvelis (4×4×4) ir (**b**) (211) supernarvelis (8×8×8)

Remiantis **4.9 pav.** ir išmatuotu greičiu pagal **4.1 lentelę**, buvo gautos standumo konstantų reikšmės. C_{11} atitinka išilginį iškraipymą ir išilginį

suspaudimą / įtempimą, todėl C_{11} galima apibūdinti kaip kietumą. Be to, skersinis iškraipymas yra prijungtas prie C_{12}, o C_{12} gaunamas iš skersinio plėtimosi, susieto su Puasono koeficientu. C_{44} yra pagrįstas šlyties moduliu, taip pat C_{44} yra nusėdimo būsenos su C_{11} ir C_{12}[62].

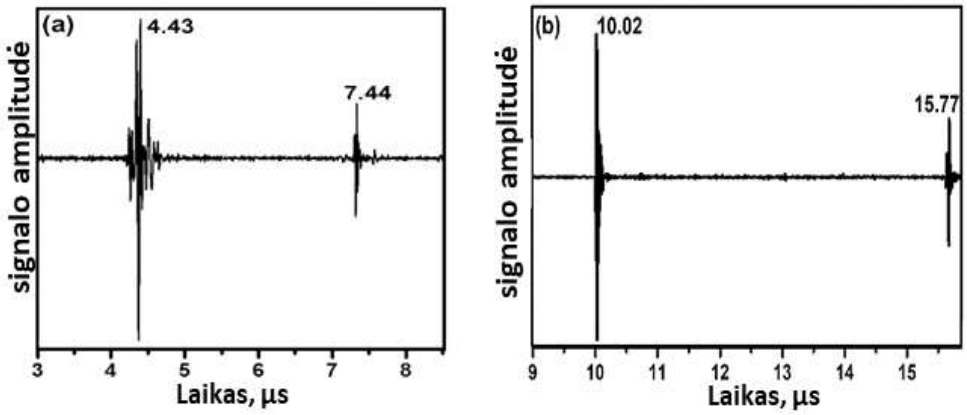

4.9 pav. Įrašyti signalai, gauti per (**a**) išilgines bangas ir (**b**) skersines $CaTiO_3$ mėginio bangas

4.1 lentelė. Bandinio išilginio ir skersinio greičio reikšmės

Išilginis greitis (m/s)	**Skersinis greitis (m/s)**	**Beveik išilginis arba beveik skersinis (m/s)**
$V_{1/1}$ = 9261,85	$V_{2/3}$ = 4960,5	$V_{12/12}$ = 4976,63
$V_{2/2}$ = 8013,51	$V_{1/2}$ = 4283,65	

Po pakeitimo ir skaičiavimo C_{11}, C_{12} ir C_{44} buvo užregistruoti atitinkamai 330,89; 93,03 ir 94,91 GPa. Šios $CaTiO_3$ vertės gerai sutapo su vertėmis, pateiktomis [63], [64] nuorodose. Pagal rezultatus t_s ir t_l reikšmės apskaičiuojamos atitinkamai 5,75 ir 3,01 µs. Be to, užregistruotas bandinio tankis 3857,30 kg/m^3, o bandinio ilgis po miltelių presavimo siekė 11,21 mm. Po skaičiavimo Youngo $CaTiO_3$ modulio vertė buvo 153,87 GPa. Ši vertė atitinka vertę, kurią nustatė Ramajo ir kt. [65]. Rezultatai ir tiesioji sutapimo linija, elementariųjų narvelių, supernarvelių (2×2×2) ir simetrijos narvelių Youngo modulio vertės buvo apskaičiuotos atitinkamai 162,62 ± 0,4 GPa, 151,71 ± 0,4 GPa ir 152,21 ± 0,4 GPa. Kaip ir tikėtasi, $CaTiO_3$ simetrijos narvelių Youngo modulio vertė (152,21 ± 0,4 GPa) gerai sutampa su eksperimentine Youngo modulio verte, gauta taikant ultragarso aido metodą (153,87 ± 0,2 GPa). Be to, Youngo modulio elementariojo narvelio vertė (162,62 ± 0,4 GPa) labiau skiriasi nuo eksperimentinės Youngo modulio vertės, todėl $CaTiO_3$ elementarusis narvelis negali būti pavaizduotas kaip visi narveliai. Taip yra dėl to, kad $CaTiO_3$ kristalito

elementariajame narvelyje neatsižvelgiama į kristalito defektus, ypač kontroliuojama deformacija, o atomų poslinkis plokštumose yra susijęs su dislokacijos tinklais [66].

4.3.4. Rentgeno spindulių difrakcijos analizė ir Williamsono-Hallo metodas USDM modelyje, skirtas tikslesnėms hidroksiapatito elementariųjų narvelių ir supernarvelių (2 × 2 × 2) įtempio deformacijos vertėms įvertinti, patvirtinta ultragarsiniu impulso aido testu (mokslinė publikacija nr. 4, Q1, 4 citata)

Šis skyrius yra pagrįstas straipsniu, paskelbtu *Journal of Materials*, **2021**, *14*, 1–16 [8]. Sintetintų HA miltelių XRD modelis parodytas **4.10 pav.** Be to, XRD modelis parodė keletą difrakcijos smailių diapazone nuo 20° iki 70°, kuriuos galima apibūdinti kaip šešiakampį HA. XRD modelis buvo įvertintas remiantis *X'pert* programiniu paketu ir modelis atitiko standartines HA XRD smailes (ICDD 9-432). Panašūs stebėjimai buvo pateikti [70], [71]nuorodose.

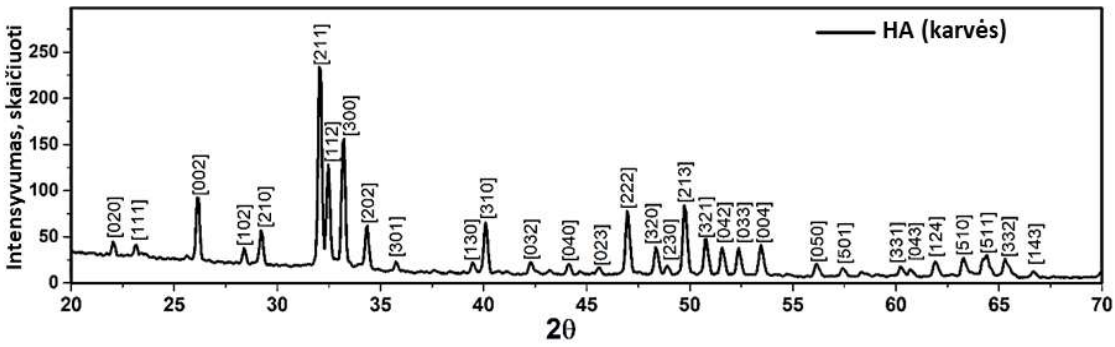

4.10 pav. HA, susintetinto 950 °C temperatūroje, rentgeno spindulių difrakcijos modelis

Pagal rentgeno spindulių difrakciją buvo apskaičiuotos kiekvienos difrakcijos plokštumos plotinio tankio vertės HA elementariuosiuose narveliuose ir supernarveliuose (2×2×2), o kaip pavyzdys – elementariųjų narvelių (020) ir supernarvelių grupės geometrija ir skaičiavimai, pavaizduoti **4.11 pav.** Norint apskaičiuoti plotinio tankio reikšmes, kartu buvo parinktos difrakcijos plokštumos nuo žemojo kampo iki aukštojo kampo. Verta paminėti, kad visų supernarvelių gardelių matrica buvo laikoma 2×2×2. Plotinis tankis apskaičiuojamas pagal atomų centrą, plokštumoje esančių atomų plotą padalijus iš bendro tos plokštumos ploto [72].

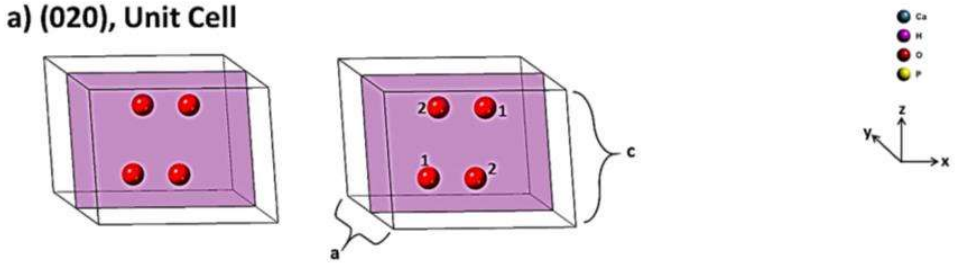

$$\text{Planar density} = \frac{[\text{number of atoms in plane(020)} \times \text{area of each atom in the plane(020)}]}{\text{area of the plane (020)}} = \frac{15.171}{65.142} = 0.233$$

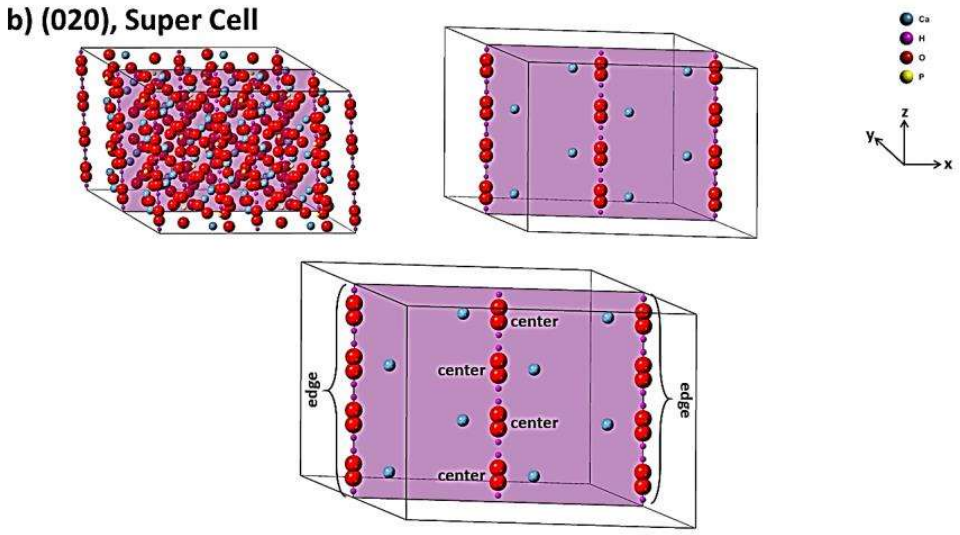

$$\text{Plokštuminis tankis} = \frac{\text{Atomų skaičius plokštumoje (020)} \times \text{Kiekvieno atomo plotas plokštumoje (020)}}{\text{plotas plokštumoje}} = \frac{119.1299}{260.568} = 0.457$$

4.11 pav. Dalyvaujančių atomų grupė ir padėtis: (**a**) (020) elementarusis narvelis ir (**b**) (020) šešiakampis HA supernarvelis

Norint parodyti mūsų siūlomo Youngo modulio nustatymo metodo įgyvendinamumą ir tikslumą, kiekvienos plokštumos Youngo modulio vertės, palyginti su elementariojo narvelio ir supernarvelių plotiniu tankiu (2×2×2), pateiktos **4.12 pav.**

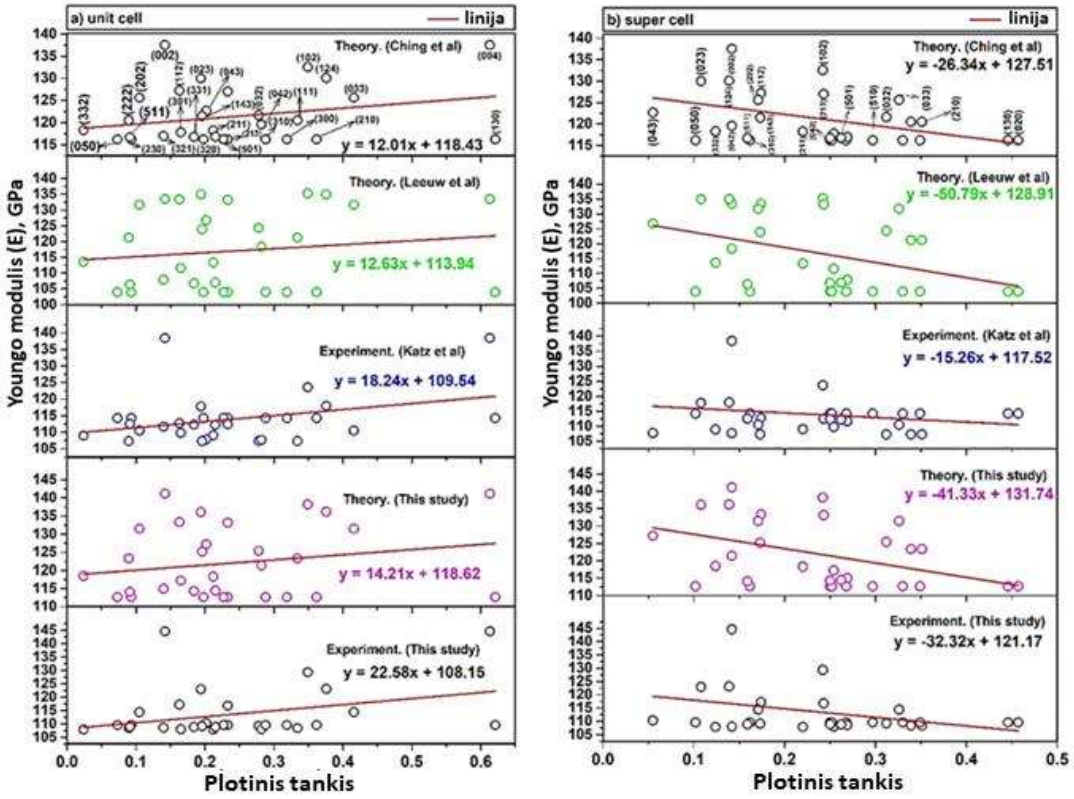

4.12 pav. Kiekvienos plokštumos **(a)** elementariojo narvelio **(b)** supernarvelių (2×2×2) HA Youngo modulis, išgautas XRD modeliais ir pagal plotinį tankį

Pagal neapibrėžties matavimą, matavimai buvo pakartoti penkis kartus ir matuojant ultragarsu gauta Youngo modulio vertė 113,08 ± 0,14 GPa. Ši vertė gerai sutampa su pateiktomis mūsų tyrimo vertėmis. Šiame tyrime tiek elementariųjų narvelių, tiek supernarvelių (2×2×2) skirtumas tarp teorinių ir eksperimentinių verčių buvo identiškas. Toks elementariųjų narvelių ir supernarvelių (2×2×2) skirtumas yra atitinkamai 10,47 GPa ir 10,57 GPa. Tai reiškia, kad teorinis skaičiavimas yra teisingas ir jį sumažinus apie ~10 GPa galima gauti eksperimentines vertes.

4.3.5. Naujas būdas *in vitro* paruošti bioaktyvius karkasus, sudarytus iš Ag legiruoto hidroksiapatito ir poliviniltrimetoksisilano (mokslinė publikacija nr. 5, Q1, 2 citata)

Šis skyrius yra pagrįstas straipsniu, paskelbtu *Journal of Polymers*, **2021**, *13*, 1–19 [77]. Čia pirmą kartą paruošėme karkasą iš Ag legiruoto HA+PVTMS. Šiame tyrime buvo atliktas mechanocheminis procesas, skirtas Ag legiruoto HA sintezei. Atsižvelgiant į plaukų raiščio ir suspensijos diferencinės skenuojamosios kalorimetrijos (DSC) kreivę, galutinė sukepinimo temperatūra parinkta 350 °C ir pagamintas akytas karkasas. Buvo atidengtos porėtos vietos, kurios gali būti

tinkamos padidinti biologinio suderinamumo santykiui. Spektroskopiniais ir mikroskopiniais metodais buvo visiškai ištirti legiravimo mechanizmas, struktūrinė raida, morfologinės savybės, mechaninės savybės ir bioaktyvumo analizė.

Šiame tyrime kaip priedas buvo naudojamas 99 % grynumo sidabro nitratas ($AgNO_3$). Ca^{2+} jonų pakeitimo Ag^+ kiekis atitinka formulę $Ca_{10-X}Ag_X(PO_4)_6(OH)_{2-X}$ $_X$. Šiuo atveju $X = 2$ ir $_X$ yra pavaizduotas kaip OH- laisvos vietos x molis, susidaręs įmaišius Ag X molį į HA gardelę. Be to, (Ca + Ag)/P santykis buvo nustatytas 1,67, o katijonų pakeitimo laipsnis buvo pakeistas. 1) HA ir $AgNO_3$ milteliai buvo sumalti naudojant didelės energijos planetinį rutulinį malūną, taikant mechaninį cheminį procesą 4 val. Mechanocheminiame procese buvo naudojami kieto chromo plieno korpusai ir rutuliukai, kurių skersmuo 20 mm. Šis procesas buvo atliktas esant aplinkos atmosferai ir 500 aps./min. greičiui, kai rutuliukų ir miltelių santykis buvo 15:1. Be to, siekiant išvengti dalelių aglomeracijos, mašina buvo kas 45 minutes sustabdoma. 2) Pasibaigus mechaniniam cheminiam procesui, buvo atliktas kalcinavimas 900 °C temperatūroje 10 °C per minutę greičiu degazavimui (90 min.). 3) Atsižvelgiant į tai, kad HA yra labai jautrus temperatūrai, transformacijai ir skilimui, buvo svarstomas kibirkštinio plazmos sukepinimo (SPS) procesas. Šiame procese milteliai buvo dedami į grafito formą (skersmuo = 20 mm), o slėgio ir temperatūros vertės buvo atitinkamai nustatytos 50 MPa ir 600 °C 10 minučių. Ag legiruoto HA kompozito gaminimo eiga parodyta **4.13 pav.** 4) Buvo paruoštas suspensijos komponentas, susidedantis iš Ag legiruoto HA (93 masės %)/PVTMS (5 masės %)/H_2O (1 masės %)/CH3COOH (1 masės %). 5) Be to, kaip naujas būdas gauti atvirą poringą struktūrą, buvo pasirinktas plaukų raištis (komercinis). 6) Jis 5 dienas buvo laikomas panardintas į suspensiją kambario temperatūroje. Pagal **4.13 pav.**, plaukų gumytė buvo nukirpta ir praardyta, panardinta į suspensiją, vėliau suvyniota. 7) Tada produktas buvo dedamas į 350 °C temperatūros krosnį 1 valandai pagal DSC kreivę, vinilo grupes ir degančio plaukų raiščio temperatūrą. Galiausiai buvo pagamintas porėtas karkasas, sudarytas iš Ag legiruoto HA+PVTMS. Būtina paminėti, kad HA yra laikoma bioaktyviąja matrica dėl kalcio fosfato grupių buvimo. Be to, Ag yra geriausias metalas antibakterinei aplinkai. Dar svarbu, kad acto rūgštis (CH_3COOH) atliko svarbų vaidmenį kaip dalelių, ypač Ag, dispergentas, neleidžiantis susidaryti koloidinėms dalelėms ir paruošti mažas daleles. PVTMS atliko svarbų vaidmenį kaip džiūvimą kontroliuojantis cheminis priedas (DCCA), apsaugantis nuo įtrūkimų ir karkaso susitraukimo.

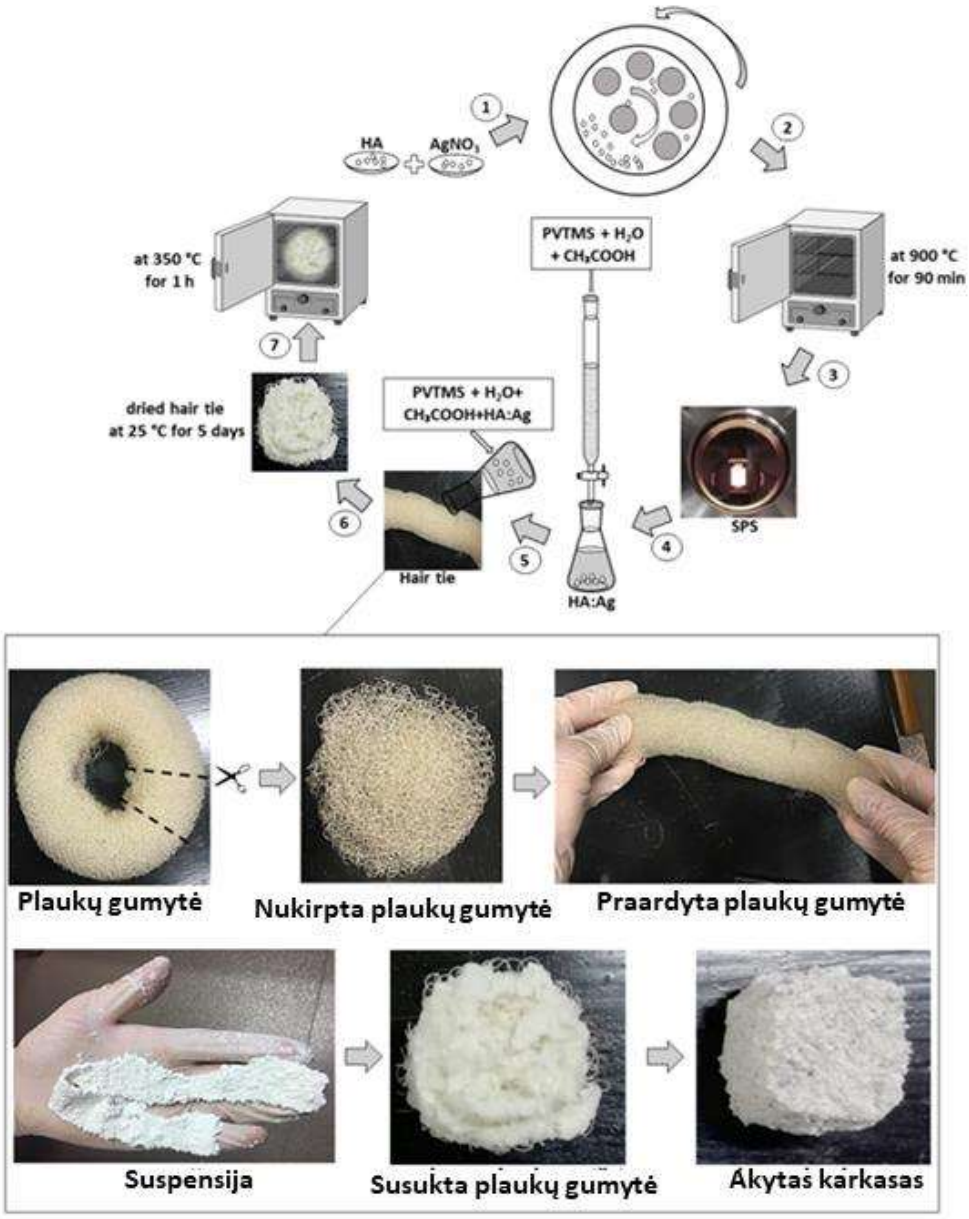

4.13 pav. Ag legiruoto HA+PVTMS karkaso gaminimo eiga

Ag legiruoto HA+PVTMS karkaso įtempių–deformacijų–suspaudimo kreivė parodyta **4.14 pav.** Išmatuota didžiausia gniuždymo stiprio vertė yra 15,71 MPa, kai deformacija yra ~0,77. Pagal Huko dėsnį, parenkant dviejų tamprumo srities taškų skirtumų reikšmes, tamprumo koeficientas apskaičiuojamas ~3,86 MPa, tad ši vertė yra mažesnė už natūralią HA standartinę vertę ir susijusi su porėtu karkasu, o konkrečiai akytumas yra didesnis dėl dėmesio bioaktyvumui šiame tyrime [7], [84]. Didžiausio gniuždymo stiprio vertė nebuvo prognozuojama naudojant plaukų raištį kaip formą. Ši vertė yra svarbi, nes: 1) karkasas gaminamas naudojant tokius komponentus kaip Ag legiruotas HA (93 masės %) / PVTMS (5 masės %) / H_2O

(1 masės %) / CH_3COOH (1 masės %), nenaudojant metalų didele koncentracija. 2) Šiuo atveju biologinio aktyvumo charakteristikos ir didelio poringumo sukūrimas buvo tikslas, o atsižvelgiant į pradinį ingredientų biologinį aktyvumą, naudojant didelės koncentracijos metalus, tokius kaip Mg, Zn, Pt, galima pagerinti gniuždymo stiprio ir mechaninio stiprumo savybių vertes.

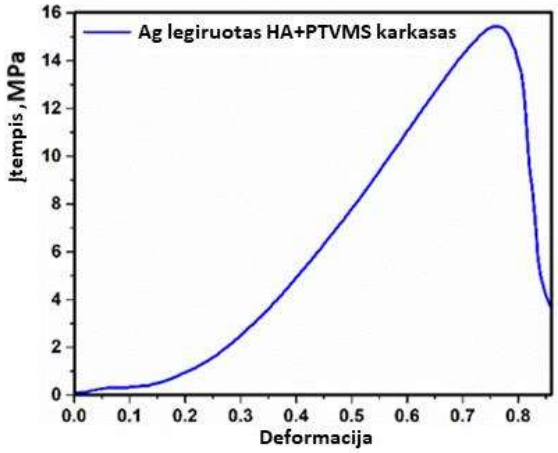

4.14 pav. Ag legiruoto HA+PVTMS karkaso įtempių–deformacijų–suspaudimo kreivė

4.3.6. Kalcinavimo temperatūros poveikis vario jodidu (5 mol%) legiruoto hidroksiapatito fotofizinėms ir mechaninėms savybėms (mokslinė publikacija nr. 6, Q2, 2 citata)

Šis skyrius yra pagrįstas straipsniu, paskelbtu *Optical Materials Journal*, 2021, *121*, 1–12 [93]. Šiame tyrime paruošti kompozitai, sudaryti iš CuI (5 mol%)/HA, buvo labai jautrūs kalcinavimo temperatūrai (nuo 25 °C iki 900 °C). Pagrindinis mūsų darbo tikslas buvo apibūdinti CuI (5 mol% koncentracija) legiruotą HA ir pagerinti savybes, ypač mechanines. Be to, nanokompozitas buvo paruoštas pritaikytu metodu ir kalcinuotas skirtingose temperatūrose. Šio tyrimo pranašumas buvo lengvai kontroliuojamas CuI (5 mol%)/HA nanokompozito paruošimo būdas. Rezultatai patvirtino, kad CuI/HA susidarymas esant skirtingoms kalcinavimo temperatūroms ir kontroliuojamas dalelių nanodydis gali būti pritaikytas mechaninėms kartoms. Mechaninėms savybėms ištirti buvo naudojamas suspaudimo bandymas kambario temperatūroje. Santykinis žiočių greitis ir apkrovos elementų reikšmės atitinkamai buvo 0,1 mm/min ir 50 KN. Kompozitų ir miltelių suspaudimo sistemos įtempių ir deformacijų kreivė parodyta **4.15 pav.**, o mechaniniu bandymu gautos vertės ir tamprumo koeficientas (tampriojo paviršiaus nuolydis) pateikiami **4.2 lentelėje**. Tamprumo koeficiento funkcija apskaičiuojama pagal **4.21 lygtį**.

$$E = \frac{\Delta\sigma}{\Delta\varepsilon} \text{ [31]} \qquad (4.21).$$

Pagal **4.21 lygtį**, $\Delta\sigma$ ir $\Delta\varepsilon$ buvo dviejų tampriosios srities taškų skirtumo reikšmės. Be to, norint apskaičiuoti kietumo vertes, buvo pritaikyta 300 g niutonų jėga, o kietumas buvo matuojamas penkiuose taškuose; rezultatai pateikti **4.2 lentelėje**.

Vidutinė mikrokietumo reikšmė buvo nuo 39,10 iki 41,02 HV. Suspaudimo bandymo rezultatas parodė, kad 900 °C deginimo temperatūra pagerino mechaninį bandymą. Esant žemai kalcinavimo temperatūrai, suspaudimo bandymo ir tamprumo vertės sumažėjo, o tai susiję su junginių kristalų dydžiu, nes kristalų dydis didėjo didėjant intermetalinei fazei tarp Cu ir I, atitinkamai. Be to, visų junginių tamprumo koeficiento vertė buvo apskaičiuota nuo 3,11 iki 4,68 GPa, ir šis diapazonas labiau skiriasi nuo natūralaus HA [94].

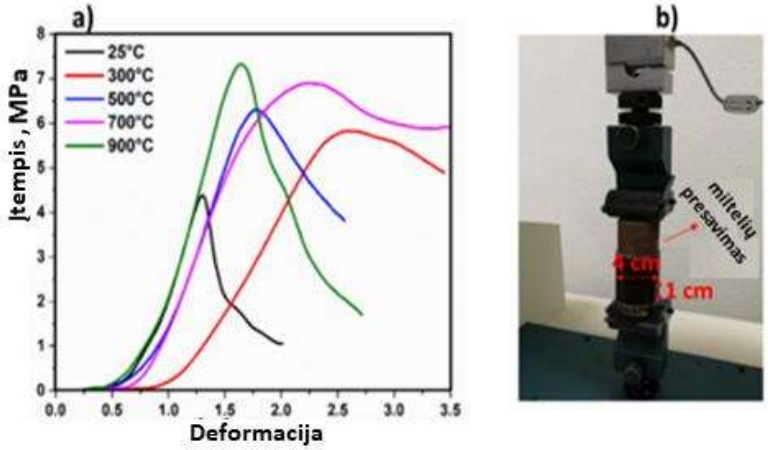

4.15 pav. a) mėginių gniuždymo įtempių–deformacijų kreivės ir **b)** miltelių presavimas

4.2 lentelė. σ_{yc} ir ε reikšmės, išskirtos pagal junginių gniuždymo įtempių–deformacijų kreivę

Junginys	Kietumas (HV)	*E* (GPa)	σ_{yc} (MPa)	ε dalis σ_{yc} (%)
25 °C	39,54	4,68	4,35	1,29
300 °C	39,21	3,89	5,83	2,59
500 °C	41,02	3,11	6,29	1,76
700 °C	39,10	4,09	6,89	2,22
900 °C	40,81	3,95	7,32	1,63

IŠVADOS

1. Pristatyta nauja kristalitų dydžio skaičiavimo metodika. Pasirinktas HA, gautas iš karvių, kiaulių ir vištų kaulų. Atliktas skirtingų šių kaulų nanokristalito dydžio skaičiavimo metodų ir modelių palyginimas kartu su BET ir TEM tyrimais. HA kristalų dydis gyvūnų kauluose svarbus tiek baziniams, tiek taikomiesiems mokslams, pvz., metalų, biostiklo, polimerų ir kompozitų legiravimui, ypač implantų gamybai. Buvo nustatyta, kad:

1.1. Modifikuota Scherrerio lygtis turi privalumą, nes sumažina paklaidas ir suteikia tikslesnę visų arba kai kurių skirtingų smailių kristalitų dydžio vertę.

1.2. Nustatyta, kad karvių, kiaulių ir vištų HA kristalitų dydžiai yra atitinkamai 60, 60 ir 57 nm.
1.3. Modifikuotas Scherrerio metodas rekomenduojamas moksliniams tyrimams ir pramonei dėl jo taikymo paprastumo, valdymo taško, mažiausių kvadratų metodo taikymo siekiant didesnio tikslumo ir duomenų nustatymo su eksperimentiniais BET rezultatais.
2. Sėkmingai pristatytas naujas kristalinių medžiagų Youngo modulio tikslios vertės matavimo metodas ir nustatyta, kad:
2.1. Plokštumos Youngo modulis apskaičiuojamas pagal visų atomų / jonų ploto plokštumoje plotinį tankį, padalytą iš plokštumos ploto.
2.2. Kiekvienos plokštumos (*y* ašies) Youngo modulis nubraižytas atsižvelgiant į tos plokštumos (*x* ašies) plotinį tankį, taikant mažiausiųjų kvadratų metodą, kad būtų gautas medžiagų Youngo modulis ašinėje atkarpoje.
2.3. NaCl (komercinis) buvo pasirinktas kaip pavyzdys, norint įdiegti naują Youngo modulio matavimo metodą, todėl apskaičiuota Youngo modulio vertė gerai sutapo su ultragarso metodu gauta verte.
2.4. W–H metodas USDM modelyje gali būti taikomas mažiausiųjų kvadratų metodo paklaidoms sumažinti ir gauti teisingam Youngo moduliui, kuris yra daug tikslesnis už vidutinę reikšmę.
2.5. Apribojimas tas, kad XRD duomenys taikomi apskaičiuojant vienodą atomų pasiskirstymą kristalinėje gardelėje su elementariuoju narveliu, todėl toks metodas negali būti taikomas amorfinėms medžiagoms.
3. Siūlomas naujas metodas, skirtas tirti patikimą Youngo modulio dydį, pagrįstą XRD, naudojant monokristalinį arba polikristalinį $CaTiO_3$ kaip kubinės gardelės pavyzdį. Šiame tyrime reikia pažymėti, kad skalių aptarimas neapima išplėstų narvelių, ir buvo nustatyta, kad:
3.1. Apskaičiuota, jog plotinio tankio ir mažiausiųjų kvadratų metodu ekstrahuoto $CaTiO_3$ Youngo modulio vertės yra atitinkamai $162{,}62 \pm 0{,}4$, $151{,}71 \pm 0{,}4$ ir $152{,}21 \pm 0{,}4$ GPa elementariesiems narveliams, supernarveliams (2×2×2) ir simetrijos narveliams.
3.2. $CaTiO_3$ simetrijos narvelių Youngo modulio vertė gerai sutampa su Youngo moduliu, nustatytu ultragarso aido metodu ir pagal literatūrą.
3.3. $CaTiO_3$ elementarusis narvelis neatspindi atomų pasiskirstymo plokštumose. Norint gauti tikrąją plotinio tankio vertę ir rasti atomų pasiskirstymo plokštumose simetriją, siūloma naudoti išplėstinius narvelius ir simetrijos narvelius.
3.4. Plotinio tankio verčių nustatymas pagal elementarųjį narvelį arba kiekvieną supernarvelį, išskyrus (8×8×8), yra įvertinimas.
3.5. Tikroji Youngo $CaTiO_3$ modulio vertė turėtų būti išskirta simetrijos narveliais arba supernarveliais (8×8×8).

4. Ištirtas W–H metodas USDM modelyje, skirtas tikslesnėms HA elementariųjų narvelių ir supernarvelių (2×2×2) įtempių deformacijų reikšmėms įvertinti. Buvo nustatyta, kad:
4.1. Remiantis šiuo tyrimu, tamprumo modulių nuolydis prieš plotinį tankį supernarveliuose (2×2×2) buvo neigiamas. Priežastis susijusi su netobulumais, o tai reiškia, kad, didėjant atomų tankiui plokštumose, dislokacijos judėjimui reikalingos mažesnės jėgos.
4.2. Dėl to plokštuma be atomo yra realesnė mažesniame elementariojo narvelio plote nei didesniame supernarvelių plote (2×2×2), o tai reiškia, kad elementariojo narvelio ašinė atkarpa yra arčiau tikrosios Youngo modulio reikšmės HA gardelėje.
4.3. Be to, palyginus HA Youngo modulio teorinius ir eksperimentinius duomenis, paaiškėjo, kad yra nedidelis skirtumas tarp elementariųjų narvelių ir supernarvelių (2×2×2) verčių, t. y. atitinkamai 10,47 GPa ir 10,57 GPa; tai reiškia, kad teorinis skaičiavimas galioja ir eksperimentinę vertę galima gauti sumažinus ją maždaug 10 GPa.
4.4. Youngo modulio vertės HA elementariuosiuose narveliuose ir supernarveliuose (2×2×2) buvo gautos atitinkamai 108, 15 ir 121, 17 GPa.
5. Mechanocheminis procesas buvo atliktas siekiant susintetinti Ag legiruotą HA. Atsižvelgiant į plaukų raiščio ir suspensijos DSC kreivę, galutinė sukepinimo temperatūra nustatyta 350 ˚C ir paruoštas porėtas karkasas. Poringumas buvo atvertas, o tai gali būti tinkama padidinti biologinio suderinamumo santykį. Spektroskopiniais ir mikroskopiniais metodais buvo tiriamas legiravimo mechanizmas, struktūrinė raida, morfologinės savybės, mechaninės savybės ir bioaktyvumo analizė. Nustatyta, kad:
5.1. Buvo pritaikytas naujas būdas pagaminti akytam karkasui naudojant plaukų gumytę. Be to, ištirtas Ag ir PVTMS apkrovos poveikis HA morfologijai, fazių kompozicijoms ir struktūrinėms savybėms.
5.2. Vidutinė akytumo reikšmė gauta esant >200 μm, todėl šios akytų sluoksnių vertės buvo tinkamos kraujo ląstelėms, ir buvo padidintas bioaktyvumo koeficientas.
5.3. PVTMS neleido karkasui įtrūkti ir susitraukti, o PVTMS struktūros laisvieji radikalai suteikė karkasui lankstumo, sujungdami C–C ir siloksaną (Si–O–Si), o PVTMS neleido sugniužti per anglies grandines terminio apdorojimo metu.
5.4. Didžiausia gniuždymo stiprio vertė siekė 15,71 MPa, o ši vertė yra reikšminga pagal Ag kiekį ir didelio metalų kiekio nebuvimą.
6. Paruošti kompozitai, susidedantys iš CuI (5 mol%)/HA, buvo labai jautrūs deginimo temperatūrai (nuo 25 °C iki 900 °C). Pagrindinis mūsų darbo tikslas buvo apibūdinti CuI (5 mol%) legiruotą HA ir pagerinti savybes, ypač mechanines. Nustatyta, kad:

6.1. Buvo pavaizduotos bandinių įtempių ir deformacijų kreivės, o didžiausia σ_{yc} vertė buvo 7,32 MPa. Be to, remiantis dėmių interferometrijos analize išskirtais vaizdais, bandinių paviršiuje nepastebėta reikšmingų netobulumų.
6.2. Galiausiai, dauguma savybių sustiprėjo didėjant deginimo temperatūrai, o optimalus deginimo temperatūros taškas pasiektas 700 $^{\circ}$C; be to, CuI legiruotas HA buvo stabilizuotas, kai mėginiuose nebuvo beveik jokių priemaišų fazių.

5. REFERENCES

[1] J.R. PARSONS, J.L. RICCI, H. ALEXANDER, P.K. BAJPAI, Osteoconductive Composite Grouts for Orthopedic Use, Ann. N. Y. Acad. Sci. 523 (1988) 190–207.
https://doi.org/10.1111/J.1749-6632.1988.TB38512.X.

[2] W. Suchanek, M. Yoshimura, Processing and properties of hydroxyapatite-based biomaterials for use as hard tissue replacement implants, J. Mater. Res. 1998 131. 13 (2011) 94–117. https://doi.org/10.1557/JMR.1998.0015.

[3] L.L. Hench, E.C. Ethridge, Biomaterials—The Interfacial Problem, Adv Biomed Eng. 5 (1975) 35–150.
https://doi.org/10.1016/B978-0-12-004905-9.50007-4.

[4] L.L. Hench, Bioceramics: From Concept to Clinic, J. Am. Ceram. Soc. 74 (1991) 1487–1510. https://doi.org/10.1111/J.1151-2916.1991.TB07132.X.

[5] D.F. Williams, Review Tissue-biomaterial interactions, J. Mater. Sci. 22 (1987) 3421–3445.

[6] A. Remes, D.F. Williams, Immune response in biocompatibility, Biomaterials. 13 (1992) 731–743.
https://doi.org/10.1016/0142-9612(92)90010-L.

[7] C.M. Botelho, R. Brooks, M. Kanitakahara, C. Ohtsuki, S. Best, M.A. Lopers, N. Rushton, W. Bonfield, J.D. Santos, C.M. Botelho, R. Brooks, M. Kanitakahara, C. Ohtsuki, S. Best, M.A. Lopers, N. Rushton, W. Bonfield, J.D. Santos, Effect of Protein Adsorption onto the Dissolution of Silicon-Substituted Hydroxyapatite, J. Encapsulation Adsorpt. Sci. 1 (2011) 72–79. https://doi.org/10.4236/JEAS.2011.14010.

[8] W. Bonfield, M. Wang, K.E. Tanner, Interfaces in analogue biomaterials, Acta Mater. 46 (1998) 2509–2518.
https://doi.org/10.1016/S1359-6454(98)80035-9.

[9] W.W. Wright, International encyclopedia of composites: Volumes 1 & 2 Edited by Stuart M. Lee, VCH Publishers, New York, 1990. Price DM 450

per Volume. Vol. 1 pp. xvi + 563. ISBN 0-89573-731-0 Vol. 2 pp. xii + 524. ISBN 0-89573-732-9, Polym. Int. 25 (1991) 132–132. https://doi.org/10.1002/PI.4990250219.

[10] W.J. Landis, J.J. Librizzi, M.G. Dunn, F.H. Silver, A study of the relationship between mineral content and mechanical properties of turkey gastrocnemius tendon, J. Bone Miner. Res. 10 (1995) 859–867. https://doi.org/10.1002/JBMR.5650100606.

[11] R. Marzouki, A. Guesmi, M.F. Zid, A. Driss, R. Marzouki, A. Guesmi, M.F. Zid, A. Driss, Synthesis, Crystal Structure and Electrical Properties of a New Mixed Compound (Na0.71Ag0.29)2CoP2O7, Cryst. Struct. Theory Appl. 1 (2012) 68–73. https://doi.org/10.4236/CSTA.2012.13013.

[12] D. Luna-Zaragoza, E.T. Romero-Guzmán, L.R. Reyes-Gutiérrez, D. Luna-Zaragoza, E.T. Romero-Guzmán, L.R. Reyes-Gutiérrez, Surface and Physicochemical Characterization of Phosphates Vivianite, Fe2(PO4)3 and Hydroxyapatite, Ca5(PO4)3OH, J. Miner. Mater. Charact. Eng. 8 (2009) 591–609. https://doi.org/10.4236/JMMCE.2009.88052.

[13] E.B. Jaffe, ABSTRACTS OF THE LITERATURE ON SYNTHESIS OF APATITES AND SOME RELATED PHOSPHATES, (n.d.).

[14] E. Yılmaz, B. Çakıroğlu, A. Gökçe, F. Findik, H.O. Gulsoy, N. Gulsoy, Ö. Mutlu, M. Özacar, Novel hydroxyapatite/graphene oxide/collagen bioactive composite coating on Ti16Nb alloys by electrodeposition, Mater. Sci. Eng. C. 101 (2019) 292–305. https://doi.org/10.1016/J.MSEC.2019.03.078.

[15] S. Lazić, Microcrystalline hydroxyapatite formation from alkaline solutions, J. Cryst. Growth. 147 (1995) 147–154. https://doi.org/10.1016/0022-0248(94)00587-7.

[16] K. Onuma, A. Ito, T. Tateishi, Investigation of a growth unit of hydroxyapatite crystal from the measurements of step kinetics, J. Cryst. Growth. 167 (1996) 773–776. https://doi.org/10.1016/0022-0248(96)00421-6.

[17] N.S. Chickerur, M.S. Tung, W.E. Brown, A mechanism for incorporation of

carbonate into apatite, Calcif. Tissue Int. 1980 321. 32 (1980) 55–62. https://doi.org/10.1007/BF02408521.

[18] Y. Ota, T. Iwashita, T. Kasuga, Y. Abe, Novel Preparation Method of Hydroxyapatite Fibers, J. Am. Ceram. Soc. 81 (1998) 1665–1668. https://doi.org/10.1111/J.1151-2916.1998.TB02529.X.

[19] M. Rabiei, A. Palevicius, A. Monshi, S. Nasiri, A. Vilkauskas, G. Janusas, Comparing Methods for Calculating Nano Crystal Size of Natural Hydroxyapatite Using X-Ray Diffraction, Nanomater. 2020, Vol. 10, Page 1627. 10 (2020) 1627. https://doi.org/10.3390/NANO10091627.

[20] E.E. Berry, The structure and composition of some calcium-deficient apatites, J. Inorg. Nucl. Chem. 29 (1967) 317–327. https://doi.org/10.1016/0022-1902(67)80033-2.

[21] P. Ducheyne, L.L. Hench, A. Kagan, M. Martens, A. Bursens, J.C. Mulier, Effect of hydroxyapatite impregnation on skeletal bonding of porous coated implants, J. Biomed. Mater. Res. 14 (1980) 225–237. https://doi.org/10.1002/JBM.820140305.

[22] D.M. Liu, T. Troczynski, W.J. Tseng, Water-based sol–gel synthesis of hydroxyapatite: process development, Biomaterials. 22 (2001) 1721–1730. https://doi.org/10.1016/S0142-9612(00)00332-X.

[23] P. Layrolle, A. Ito, T. Tateishi, Sol-Gel Synthesis of Amorphous Calcium Phosphate and Sintering into Microporous Hydroxyapatite Bioceramics, J. Am. Ceram. Soc. 81 (1998) 1421–1428. https://doi.org/10.1111/J.1151-2916.1998.TB02499.X.

[24] J.-C. Schroti'er, A. Cardenas, M. Smaihi, N. Hovnanian, Silicon and Phosphorus Alkoxide Mixture: Sol-Gel Study by Spectroscopic Technics, J. Sol-Gel Sci. Technol. 4 (1995) 195–204.

[25] K. Agrawal, G. Singh, D. Puri, S. Prakash, Synthesis and Characterization of Hydroxyapatite Powder by Sol-Gel Method for Biomedical Application, J. Miner. Mater. Charact. Eng. 10 (2011) 727–734. https://doi.org/10.4236/jmmce.2011.108057.

[26] K. Agrawal, G. Singh, D. Puri, S. Prakash, K. Agrawal, G. Singh, D. Puri, S. Prakash, Synthesis and Characterization of Hydroxyapatite Powder by Sol-Gel Method for Biomedical Application, J. Miner. Mater. Charact. Eng. 10 (2011) 727–734. https://doi.org/10.4236/JMMCE.2011.108057.

[27] C. Chai, B. Ben-Nissan, S. Pyke, L. Evans, Sol-Gel Derived Hydroxylapatite Coatings for Biomedical Applications, Http://Dx.Doi.Org/10.1080/10426919508935016. 10 (2007) 205–216. https://doi.org/10.1080/10426919508935016.

[28] A.P. Ameen, R.D. Short, R. Johns, G. Schwach, The surface analysis of implant materials. The surface composition of a titanium dental implant material., Clin. Oral Implants Res. 4 (1993) 144–150. https://doi.org/10.1034/J.1600-0501.1993.040305.X.

[29] S. Ramakrishna, J. Mayer, E. Wintermantel, K.W. Leong, Biomedical applications of polymer-composite materials: a review, Compos. Sci. Technol. 61 (2001) 1189–1224. https://doi.org/10.1016/S0266-3538(00)00241-4.

[30] R. Murugan, S. Ramakrishna, K. Panduranga Rao, Nanoporous hydroxy-carbonate apatite scaffold made of natural bone, Mater. Lett. 60 (2006) 2844–2847. https://doi.org/10.1016/J.MATLET.2006.01.104.

[31] X. Deng, J. Hao, C. Wang, Preparation and mechanical properties of nanocomposites of poly(d,l-lactide) with Ca-deficient hydroxyapatite nanocrystals, Biomaterials. 22 (2001) 2867–2873. https://doi.org/10.1016/S0142-9612(01)00031-X.

[32] S.C. Liou, S.Y. Chen, D.M. Liu, Synthesis and characterization of needlelike apatitic nanocomposite with controlled aspect ratios, Biomaterials. 24 (2003) 3981–3988. https://doi.org/10.1016/S0142-9612(03)00303-X.

[33] Z. Fu, J. Cui, B. Zhao, S.G. Shen, K. Lin, An overview of polyester/hydroxyapatite composites for bone tissue repairing, J. Orthop. Transl. 28 (2021) 118–130. https://doi.org/10.1016/J.JOT.2021.02.005.

[34] Q. Pan, Y. Li, J. Xu, Y. Kang, Y. Li, B. Wang, Y.P. Yang, S. Lin, G. Li, The

effects of tubular structure on biomaterial aided bone regeneration in distraction osteogenesis, J. Orthop. Transl. 25 (2020) 80–86. https://doi.org/10.1016/J.JOT.2020.09.009.

[35] D.K. Patel, S.D. Dutta, J. Hexiu, K. Ganguly, K.T. Lim, Bioactive electrospun nanocomposite scaffolds of poly(lactic acid)/cellulose nanocrystals for bone tissue engineering, Int. J. Biol. Macromol. 162 (2020) 1429–1441. https://doi.org/10.1016/J.IJBIOMAC.2020.07.246.

[36] S. Surucu, H. Turkoglu Sasmazel, Development of core-shell coaxially electrospun composite PCL/chitosan scaffolds, Int. J. Biol. Macromol. 92 (2016) 321–328. https://doi.org/10.1016/J.IJBIOMAC.2016.07.013.

[37] G. Sen Shi, Y.Y. Li, Y.P. Luo, J.F. Jin, Y.X. Sun, L.Z. Zheng, Y.X. Lai, L. Li, G. hui Fu, L. Qin, S.H. Chen, Bioactive PLGA/tricalcium phosphate scaffolds incorporating phytomolecule icaritin developed for calvarial defect repair in rat model, J. Orthop. Transl. 24 (2020) 112–120. https://doi.org/10.1016/J.JOT.2020.05.008.

[38] X. Yang, L. Li, D. Yang, J. Nie, G. Ma, Electrospun Core–Shell Fibrous 2D Scaffold with Biocompatible Poly(Glycerol Sebacate) and Poly-l-Lactic Acid for Wound Healing, Adv. Fiber Mater. 2 (2020) 105–117. https://doi.org/10.1007/S42765-020-00027-X/FIGURES/6.

[39] L.L. Hench, Sol-gel materials for bioceramic applications, Curr. Opin. Solid State Mater. Sci. 2 (1997) 604–610.
https://doi.org/10.1016/S1359-0286(97)80053-8.

[40] Z. Zhou, B. Zheng, Y. Gu, C. Shen, J. Wen, Z. Meng, S. Chen, J. Ou, A. Qin, New approach for improving anticorrosion and biocompatibility of magnesium alloys via polydopamine intermediate layer-induced hydroxyapatite coating, Surfaces and Interfaces. 19 (2020) 100501. https://doi.org/10.1016/J.SURFIN.2020.100501.

[41] A. Zomorodian, M.P. Garcia, T. Moura E Silva, J.C.S. Fernandes, M.H. Fernandes, M.F. Montemor, Biofunctional composite coating architectures based on polycaprolactone and nanohydroxyapatite for controlled corrosion

activity and enhanced biocompatibility of magnesium AZ31 alloy, Mater. Sci. Eng. C. 48 (2015) 434–443. https://doi.org/10.1016/J.MSEC.2014.12.027.

[42] M. Wang, B. Duan, Materials and Their Biomedical Applications, Encycl. Biomed. Eng. 1–3 (2019) 135–152. https://doi.org/10.1016/B978-0-12-801238-3.99860-X.

[43] R. Marzieh, N. Sohrab, P. Arvydas, J. Giedrius, Preparation and investigation of bioactive organic-inorganic nano-composite derived from PVB-co-VA-co-VAc/HA, 15th Int. Conf. Mechatron. Syst. Mater. MSM 2020. (2020). https://doi.org/10.1109/MSM49833.2020.9201632.

[44] Y. Han, Q. Wei, P. Chang, K. Hu, O.V. Okoro, A. Shavandi, L. Nie, Three-Dimensional Printing of Hydroxyapatite Composites for Biomedical Application, Cryst. 2021, Vol. 11, Page 353. 11 (2021) 353. https://doi.org/10.3390/CRYST11040353.

[45] V. Bystrov, E. Paramonova, L. Avakyan, J. Coutinho, N. Bulina, Simulation and Computer Study of Structures and Physical Properties of Hydroxyapatite with Various Defects, Nanomater. 2021, Vol. 11, Page 2752. 11 (2021) 2752. https://doi.org/10.3390/NANO11102752.

[46] V.K. Sharma, R.A. Yngard, Y. Lin, Silver nanoparticles: Green synthesis and their antimicrobial activities, Adv. Colloid Interface Sci. 145 (2009) 83–96. https://doi.org/10.1016/J.CIS.2008.09.002.

[47] L. Mei, Z. Lu, X. Zhang, C. Li, Y. Jia, Polymer-Ag nanocomposites with enhanced antimicrobial activity against bacterial infection, ACS Appl. Mater. Interfaces. 6 (2014) 15813–15821. https://doi.org/10.1021/AM502886M.

[48] R.G. Saratale, G.D. Saratale, G. Ghodake, S.K. Cho, A. Kadam, G. Kumar, B.H. Jeon, D. Pant, A. Bhatnagar, H.S. Shin, Wheat straw extracted lignin in silver nanoparticles synthesis: Expanding its prophecy towards antineoplastic potency and hydrogen peroxide sensing ability, Int. J. Biol. Macromol. 128 (2019) 391–400. https://doi.org/10.1016/J.IJBIOMAC.2019.01.120.

[49] L. Badrour, A. Sadel, M. Zahir, L. Kimakh, A. El Hajbi, Synthesis and

physical and chemical characterization of Ca10−xAgx(PO4)6(OH)2−xx apatites, Ann. Chim. Sci. Des Matériaux. 23 (1998) 61–64. https://doi.org/10.1016/S0151-9107(98)80012-3.

[50] G.D. Saratale, R.G. Saratale, D.S. Kim, D.Y. Kim, H.S. Shin, Exploiting Fruit Waste Grape Pomace for Silver Nanoparticles Synthesis, Assessing Their Antioxidant, Antidiabetic Potential and Antibacterial Activity Against Human Pathogens: A Novel Approach, Nanomater. 2020, Vol. 10, Page 1457. 10 (2020) 1457. https://doi.org/10.3390/NANO10081457.

[51] C.S. Ciobanu, S.L. Iconaru, M.C. Chifiriuc, A. Costescu, P. Le Coustumer, D. Predoi, Synthesis and antimicrobial activity of silver-doped hydroxyapatite nanoparticles, Biomed Res. Int. 2013 (2013). https://doi.org/10.1155/2013/916218.

[52] S.K. Rastogi, V.J. Rutledge, C.L. Gibson, D.A. Newcombe, J.R. Branen, A.L. Branen, Ag colloids and Ag clusters over EDAPTMS-coated silica nanoparticles: synthesis, characterization, and antibacterial activity against Escherichia coli, Nanomedicine Nanotechnology, Biol. Med. 7 (2011) 305–314. https://doi.org/10.1016/J.NANO.2010.11.003.

[53] M. Lim, D. Kim, J. Seo, H. Han, Preparation and properties of poly(vinyl alcohol)/vinyltrimethoxysilane (PVA/VTMS) hybrid films with enhanced thermal stability and oxygen barrier properties, Macromol. Res. 2014 2210. 22 (2014) 1096–1103. https://doi.org/10.1007/S13233-014-2146-2.

[54] A. Motalebi, M. Nasr-Esfahani, R. Ali, M. Pourriahi, Improvement of corrosion performance of 316L stainless steel via PVTMS/henna thin film, Prog. Nat. Sci. Mater. Int. 22 (2012) 392–400. https://doi.org/10.1016/J.PNSC.2012.10.006.

[55] M. Ferhat, A. Zaoui, M. Certier, J.P. Dufour, B. Khelifa, Electronic structure of the copper halides CuCl, CuBr and Cul, Mater. Sci. Eng. B. 39 (1996) 95–100.

https://doi.org/10.1016/0921-5107(95)01518-3.

[56] V.N. Ermakov, S.P. Kruchinin, A. Fujiwara, Electronic Nanosensors Based

On Nanotransistor With Bistability Behaviour, (2008) 341–349. https://doi.org/10.1007/978-1-4020-9146-9_26.

[57] Y. Huang, Z. Xu, X. Zhang, X. Chang, X. Zhang, Y.C. Li, T. Ye, R. Han, S. Han, Y. Gao, X. Du, H. Yang, Nanotube-formed Ti substrates coated with silicate/silver co-doped hydroxyapatite as prospective materials for bone implants, J. Alloys Compd. 697 (2017) 182–199. https://doi.org/10.1016/j.jallcom.2016.12.139.

[58] A. Dubnika, D. Loca, V. Rudovica, M.B. Parekh, L. Berzina-Cimdina, Functionalized silver doped hydroxyapatite scaffolds for controlled simultaneous silver ion and drug delivery, Ceram. Int. 43 (2017) 3698–3705. https://doi.org/10.1016/j.ceramint.2016.11.214.

[59] C.S. Ciobanu, S.L. Iconaru, F. Massuyeau, L.V. Constantin, A. Costescu, D. Predoi, Synthesis, structure, and luminescent properties of europium-doped hydroxyapatite nanocrystalline powders, J. Nanomater. 2012 (2012). https://doi.org/10.1155/2012/942801.

[60] M. Mirzaee, M. Vaezi, Y. Palizdar, Synthesis and characterization of silver doped hydroxyapatite nanocomposite coatings and evaluation of their antibacterial and corrosion resistance properties in simulated body fluid, Mater. Sci. Eng. C. 69 (2016) 675–684. https://doi.org/10.1016/j.msec.2016.07.057.

[61] G. Renaudin, S. Gomes, J.-M. Nedelec, First-Row Transition Metal Doping in Calcium Phosphate Bioceramics: A Detailed Crystallographic Study, Materials (Basel). 10 (2017) 92. https://doi.org/10.3390/ma10010092.

[62] S. Gomes, A. Kaur, J.M. Grenèche, J.M. Nedelec, G. Renaudin, Atomic scale modeling of iron-doped biphasic calcium phosphate bioceramics, Acta Biomater. 50 (2017) 78–88. https://doi.org/10.1016/j.actbio.2016.12.011.

[63] S. Khamseh, M. Ganjaee Sari, E. Alibakhshi, M. Nemati Valandaran, Hydrogen-free Cu: Amorphous-C: N Coating on TC4 Titanium Alloy: The Role of Gas Ratio on Mechanical and Antibacterial Potency, Prog. Color. Color. Coatings. 14 (2021) 281–291.

https://doi.org/10.30509/pccc.2021.166770.1102.

[64] A. V. Artem'ev, M.P. Davydova, X. Hei, M.I. Rakhmanova, D.G. Samsonenko, I.Y. Bagryanskaya, K.A. Brylev, V.P. Fedin, J.-S. Chen, M. Cotlet, J. Li, Family of Robust and Strongly Luminescent CuI-Based Hybrid Networks Made of Ionic and Dative Bonds, Chem. Mater. 32 (2020) 10708–10718. https://doi.org/10.1021/ACS.CHEMMATER.0C03984.

[65] Nachrichten von der Gesellschaft der Wissenschaften zu Göttingen, Mathematisch-Physikalische Klasse, n.d.

[66] R. Das, S.S. Nath, R. Bhattacharjee, Preparation of linoleic acid capped gold nanoparticles and their spectra, Phys. E Low-Dimensional Syst. Nanostructures. 43 (2010) 224–227. https://doi.org/10.1016/J.PHYSE.2010.07.008.

[67] P.C. Dey, R. Das, Effect of silver doping on the elastic properties of CdS nanoparticles, (n.d.). https://doi.org/10.1007/s12648-018-1214-4.

[68] R.S. Darweesh, N.M. Ayoub, S. Nazzal, Gold nanoparticles and angiogenesis: molecular mechanisms and biomedical applications , Int. J. Nanomedicine. 14 (2019) 7643–7663. https://doi.org/10.2147/IJN.S223941.

[69] Y.T. Prabhu, K.V. Rao, V.S.S. Kumar, B.S. Kumari, Y.T. Prabhu, K.V. Rao, V.S.S. Kumar, B.S. Kumari, X-Ray Analysis by Williamson-Hall and Size-Strain Plot Methods of ZnO Nanoparticles with Fuel Variation, World J. Nano Sci. Eng. 4 (2014) 21–28. https://doi.org/10.4236/WJNSE.2014.41004.

[70] K. Rajabi, S. Hosseini-Hashemi, Application of the generalized Hooke's law for viscoelastic materials (GHVMs) in nanoscale mass sensing applications of viscoelastic nanoplates: A theoretical study, Eur. J. Mech. - A/Solids. 67 (2018) 71–83. https://doi.org/10.1016/J.EUROMECHSOL.2017.08.015.

[71] M.B. Kanoun, S. Goumri-Said, K. Abdullah, Theoretical study of physical properties and oxygen incorporation effect in nanolaminated ternary carbides 211-MAX phases, Adv. Sci. Technol. Mn+1AXn Phases. (2012) 177–196. https://doi.org/10.1533/9780857096012.177.

[72] Y. Li, R.B. Thompson, Relations between elastic constants Cij and texture

parameters for hexagonal materials, J. Appl. Phys. 67 (1998) 2663. https://doi.org/10.1063/1.345479.

[73] M. Mah, D.R. Schmitt, Correction to "Determination of the complete elastic stiffnesses from ultrasonic phase velocity measurements," J. Geophys. Res. Solid Earth. 108 (2003) 2490. https://doi.org/10.1029/2003JB002710.

[74] J.R. Neighbours, G.E. Schacher, Determination of Elastic Constants from Sound-Velocity Measurements in Crystals of General Symmetry, J. Appl. Phys. 38 (2004) 5366. https://doi.org/10.1063/1.1709328.

[75] W.C. Van Buskirk, S.C. Cowin, R.N. Ward, Ultrasonic Measurement of Orthotropic Elastic Constants of Bovine Femoral Bone, J. Biomech. Eng. 103 (1981) 67–72. https://doi.org/10.1115/1.3138262.

[76] ASTM E797/E797M-15 - Standard Practice for Measuring Thickness by Manual Ultrasonic Pulse-Echo Contact Method, (n.d.). https://webstore.ansi.org/Standards/ASTM/astme797e797m15 (accessed May 7, 2022).

[77] Mechanics of Microstructured Materials, Mech. Microstruct. Mater. (2004). https://doi.org/10.1007/978-3-7091-2776-6.

[78] N. Pandech, K. Sarasamak, S. Limpijumnong, Elastic properties of perovskite ATiO3 (A = Be, Mg, Ca, Sr, and Ba) and PbBO3 (B = Ti, Zr, and Hf): First principles calculations, J. Appl. Phys. 117 (2015) 174108. https://doi.org/10.1063/1.4919837.

[79] H. Wang, P.L. Prendiville, P.J. McDonnell, W. V. Chang, An ultrasonic technique for the measurement of the elastic moduli of human cornea, J. Biomech. 29 (1996) 1633–1636.
https://doi.org/10.1016/S0021-9290(96)80017-0.

[80] Nondestructive Evaluation: A Tool in Design, Manufacturing and Service - Don E. Bray, Roderick K. Stanley - Google Books, (n.d.). https://books.google.com.et/books?id=5WtmjwEACAAJ&printsec=copyright#v=onepage&q&f=false (accessed May 7, 2022).

[81] M. Rabiei, A. Palevicius, S. Nasiri, A. Dashti, A. Vilkauskas, G. Janusas,

Relationship between Young's Modulus and Planar Density of Unit Cell, Super Cells (2 × 2 × 2), Symmetry Cells of Perovskite (CaTiO3) Lattice, Mater. 2021, Vol. 14, Page 1258. 14 (2021) 1258. https://doi.org/10.3390/MA14051258.

[82] R.S. Figliola, D.E. Beasley, Theory and design for mechanical measurements, (n.d.).

[83] M. Rabiei, A. Palevicius, A. Monshi, S. Nasiri, A. Vilkauskas, G. Janusas, Comparing methods for calculating nano crystal size of natural hydroxyapatite using X-ray diffraction, Mdpi.Com. 10 (2020). https://doi.org/10.3390/nano10091627.

[84] Characteristics of calcium phosphate powders synthesized from cuttlefish bone and phosphoric acid | Semantic Scholar, (n.d.). https://www.semanticscholar.org/paper/Characteristics-of-calcium-phosphate-powders-from-Lee Chun/54d063086000d9259ba66c34c8588944e1d50678 (accessed May 11, 2022).

[85] J. Venkatesan, Z.J. Qian, B. Ryu, N. Ashok Kumar, S.K. Kim, Preparation and characterization of carbon nanotube-grafted-chitosan - Natural hydroxyapatite composite for bone tissue engineering, Carbohydr. Polym. 83 (2011) 569–577. https://doi.org/10.1016/J.CARBPOL.2010.08.019.

[86] M.K. Herliansyah, D.A. Nasution, M.H. Bin Abdul Shukor, A. Ide-Ektessabi, M.W. Wildan, A.E. Tontowi, Preparation and Characterization of Natural Hydroxyapatite: A Comparative Study of Bovine Bone Hydroxyapatite and Hydroxyapatite from Calcite, Mater. Sci. Forum. 561–565 (2007) 1441–1444. https://doi.org/10.4028/WWW.SCIENTIFIC.NET/MSF.561-565.1441.

[87] Characterisation of natural hydroxyapatite extracted from bovine cortical bone ash | Semantic Scholar, (n.d.). https://www.semanticscholar.org/paper/Characterisation-of-natural-hydroxyapatite-from-ash-Bahrololoom-Javidi/5c9c0b81a419ea76f5d2c65a19c5bd68de42964b (accessed May 11,

2022).

[88] S. Shahabi, F. Najafi, A. Majdabadi, T. Hooshmand, M. Haghbin Nazarpak, B. Karimi, S.M. Fatemi, Effect of gamma irradiation on structural and biological properties of a PLGA-PEG-hydroxyapatite composite, Sci. World J. 2014 (2014). https://doi.org/10.1155/2014/420616.

[89] L.L. Hench, J. Wilson, An Introduction to bioceramics, World Scientific, Singapore ;;River Edge N.J., 1993.

[90] A. Esmaeilkhanian, F. Sharifianjazi, A. Abouchenari, A. Rouhani, N. Parvin, M. Irani, Synthesis and Characterization of Natural Nano-hydroxyapatite Derived from Turkey Femur-Bone Waste, Appl. Biochem. Biotechnol. 189 (2019) 919–932.
https://doi.org/10.1007/S12010-019-03046-6/TABLES/1.

[91] A. Monshi, M.R. Foroughi, M.R. Monshi, A. Monshi, M.R. Foroughi, M.R. Monshi, Modified Scherrer Equation to Estimate More Accurately Nano-Crystallite Size Using XRD, World J. Nano Sci. Eng. 2 (2012) 154–160. https://doi.org/10.4236/WJNSE.2012.23020.

[92] A. Doostmohammadi, A. Monshi, R. Salehi, M.H. Fathi, S. Karbasi, U. Pieles, A.U. Daniels, Preparation, chemistry and physical properties of bone-derived hydroxyapatite particles having a negative zeta potential, Mater. Chem. Phys. 132 (2012) 446–452. https://doi.org/10.1016/J.MATCHEMPHYS.2011.11.051.

[93] M. Rabiei, A. Palevicius, A. Dashti, S. Nasiri, A. Monshi, A. Vilkauskas, G. Janusas, Measurement Modulus of Elasticity Related to the Atomic Density of Planes in Unit Cell of Crystal Lattices, Mater. 2020, Vol. 13, Page 4380. 13 (2020) 4380. https://doi.org/10.3390/MA13194380.

[94] N. Bernstein, H.J. Gotsis, D.A. Papaconstantopoulos, M.J. Mehl, Tight-binding calculations of the band structure and total energies of the various polytypes of silicon carbide, Phys. Rev. B - Condens. Matter Mater. Phys. 71 (2005) 075203. https://doi.org/10.1103/PHYSREVB.71.075203/FIGURES/9/MEDIUM.

[95] H.B. Huntington, The Elastic Constants of Crystals, Solid State Phys. - Adv. Res. Appl. 7 (1958) 213–351. https://doi.org/10.1016/S0081-1947(08)60553-6.

[96] O. Joshua, F.J. Bayo-Kujore, K.O. Olusola, S.M. Abdou, H. Moharam, Characterization of table salt samples from different origins and ESR detection of the induced effects due to gamma irradiation, J. Phys. Conf. Ser. 1253 (2019) 012036. https://doi.org/10.1088/1742-6596/1253/1/012036.

[97] S.H. Jury, R.C. Ernst, The first approximate conditions for the formation of liquid crystals in solution, J. Phys. Colloid Chem. 53 (1949) 609–624. https://doi.org/10.1021/J150470A002/ASSET/J150470A002.FP.PNG_V03.

[98] Handbook on Physical Properties of Semiconductors - Sadao Adachi - Google Books, (n.d.). https://books.google.lt/books?hl=en&lr=&id=U-4T5Kvfdx0C&oi=fnd&pg=PR33&dq=Handbook+on+Physical+Properties+of+Semiconductors%3B+Springer:+New+York,+NY&ots=_hhgOoHyDD&sig=GvoHPZl-HylRcLprJ8piyo5N3Jk&redir_esc=y#v=onepage&q&f=false (accessed May 11, 2022).

[99] A.N. Norris, Poisson's ratio in cubic materials, Proc. R. Soc. A Math. Phys. Eng. Sci. 462 (2006) 3385–3405. https://doi.org/10.1098/RSPA.2006.1726.

[100] L. Liu, X.Z. Wu, R. Wang, H.F. Feng, S. Wu, High-pressure effect on elastic constants, stacking fault energy and correlation with dislocation properties in MgO and CaO, Eur. Phys. J. B. 85 (2012) 226. https://doi.org/10.1140/epjb/e2012-30032-4.

[101] F.S. Khan, P.B. Allen, Temperature Dependence of the Elastic Constants of p+ Silicon, Phys. Status Solidi. 128 (1985) 31–38. https://doi.org/10.1002/PSSB.2221280104.

[102] E. Güler, M. Güler, Elastic and Mechanical Properties of Cubic Diamond under Pressure, Chinese J. Phys. 53 (2015) 195–205. https://doi.org/10.6122/CJP.20141230.

[103] S. Sahoo, S.K.S. Parashar, S.M. Ali, CaTiO3 nano ceramic for NTCR thermistor based sensor application, J. Adv. Ceram. 3 (2014) 117–124.

https://doi.org/10.1007/s40145-014-0100-6.

[104] E. Cockayne, B.P. Burton, Phonons and static dielectric constant in from first principles, Phys. Rev. B - Condens. Matter Mater. Phys. 62 (2000) 3735–3743. https://doi.org/10.1103/PhysRevB.62.3735.

[105] Y. Li, R.B. Thompson, Relations between elastic constants Cij and texture parameters for hexagonal materials, J. Appl. Phys. 67 (1990) 2663–2665. https://doi.org/10.1063/1.345479.

[106] M. De Jong, W. Chen, T. Angsten, A. Jain, R. Notestine, A. Gamst, M. Sluiter, C.K. Ande, S. Van Der Zwaag, J.J. Plata, C. Toher, S. Curtarolo, G. Ceder, K.A. Persson, M. Asta, Charting the complete elastic properties of inorganic crystalline compounds, Sci. Data 2015 21. 2 (2015) 1–13. https://doi.org/10.1038/sdata.2015.9.

[107] S. Tariq, A. Ahmed, S. Saad, S. Tariq, Structural, electronic and elastic properties of the cubic CaTiO3 under pressure: A DFT study, AIP Adv. 5 (2015) 077111. https://doi.org/10.1063/1.4926437.

[108] M.A. Ramírez, R. Parra, M.M. Reboredo, J.A. Varela, M.S. Castro, L. Ramajo, Elastic modulus and hardness of CaTiO3, CaCu3Ti4O12 and CaTiO3/CaCu3Ti4O12 mixture, Mater. Lett. 64 (2010) 1226–1228. https://doi.org/10.1016/J.MATLET.2010.02.058.

[109] V. Berdichevsky, Energy of dislocation networks, Int. J. Eng. Sci. 103 (2016) 35–44. https://doi.org/10.1016/j.ijengsci.2016.02.011.

[110] Introduction to Dislocations - 5th Edition, (n.d.). https://www.elsevier.com/books/introduction-to-dislocations/hull/978-0-08-096672-4 (accessed December 29, 2020).

[111] U. Englert, Symmetry Relationships between Crystal Structures. Applications of Crystallographic Group Theory in Crystal Chemistry. By Ulrich Müller., Angew. Chemie Int. Ed. 52 (2013) 11973–11973. https://doi.org/10.1002/anie.201306902.

[112] O.H. Duparc, É. Polytechnique, O.B.M.H. Duparc, A review of some elements in the history of grain boundaries, centered on Georges Friedel, the

coincident “site” lattice and the twin index Crystallography History View project ANR FluTi View project A review of some elements in the history of grain boundaries, centered on Georges Friedel, the coincident “site” lattice and the twin index, Artic. J. Mater. Sci. (2011). https://doi.org/10.1007/s10853-011-5367-1.

[113] M. Rabiei, A. Palevicius, A. Dashti, S. Nasiri, A. Monshi, A. Doustmohammadi, A. Vilkauskas, G. Janusas, X-ray Diffraction Analysis and Williamson-Hall Method in USDM Model for Estimating More Accurate Values of Stress-Strain of Unit Cell and Super Cells (2×2×2) of Hydroxyapatite, Confirmed by Ultrasonic Pulse-Echo Test, Mater. 2021, Vol. 14, Page 2949. 14 (2021) 2949. https://doi.org/10.3390/MA14112949.

[114] M. Rabiei, A. Palevicius, A. Dashti, S. Nasiri, A. Monshi, A. Vilkauskas, G. Janusas, Measurement Modulus of Elasticity Related to the Atomic Density of Planes in Unit Cell of Crystal Lattices, Mater. 2020, Vol. 13, Page 4380. 13 (2020) 4380. https://doi.org/10.3390/MA13194380.

[115] M. Rabiei, A. Palevicius, S. Nasiri, A. Dashti, A. Vilkauskas, G. Janusas, Relationship between Young’s Modulus and Planar Density of Unit Cell, Super Cells (2 × 2 × 2), Symmetry Cells of Perovskite (CaTiO3) Lattice, Mater. 2021, Vol. 14, Page 1258. 14 (2021) 1258. https://doi.org/10.3390/MA14051258.

[116] R. Jacob, J. Isac, X-ray diffraction line profile analysis of Ba0.6Sr0.4FexTi(1-x) O3-δ, (x=0.4), ~ 12 ~ Int. J. Chem. Stud. 2 (2015) 12–21.

[117] K. Venkateswarlu, A. Chandra Bose, N. Rameshbabu, X-ray peak broadening studies of nanocrystalline hydroxyapatite by Williamson–Hall analysis, Phys. B Condens. Matter. 405 (2010) 4256–4261. https://doi.org/10.1016/J.PHYSB.2010.07.020.

[118] K. Itatani, K. Tsuchiya, Y. Sakka, I.J. Davies, S. Koda, Superplastic deformation of hydroxyapatite ceramics with B2O3 or Na2O addition fabricated by pulse current pressure sintering, J. Eur. Ceram. Soc. 31 (2011)

2641–2648. https://doi.org/10.1016/J.JEURCERAMSOC.2011.01.014.

[119] M. Rabiei, A. Palevicius, R. Ebrahimi-Kahrizsangi, S. Nasiri, A. Vilkauskas, G. Janusas, New Approach for Preparing In Vitro Bioactive Scaffold Consisted of Ag-Doped Hydroxyapatite + Polyvinyltrimethoxysilane, Polym. 2021, Vol. 13, Page 1695. 13 (2021) 1695. https://doi.org/10.3390/POLYM13111695.

[120] Y. Abe, T. Namiki, K. Tuchida, Y. Nagao, T. Misono, Preparation and properties of silicon-containing hybrid gels from vinyltrimethoxysilane, J. Non. Cryst. Solids. 147–148 (1992) 47–51. https://doi.org/10.1016/S0022-3093(05)80591-5.

[121] K. Tsuru, S. Hayakawa, C. Ohtsuki, A. Osaka, Bioactive Gel Coatings Derived from Vinyltrimethoxysilane, 1998.

[122] C.M. Murphy, M.G. Haugh, F.J. O'Brien, The effect of mean pore size on cell attachment, proliferation and migration in collagen-glycosaminoglycan scaffolds for bone tissue engineering, Biomaterials. 31 (2010) 461–466. https://doi.org/10.1016/j.biomaterials.2009.09.063.

[123] S.F. Hulbert, F.A. Young, R.S. Mathews, J.J. Klawitter, C.D. Talbert, F.H. Stelling, Potential of ceramic materials as permanently implantable skeletal prostheses, J. Biomed. Mater. Res. 4 (1970) 433–456. https://doi.org/10.1002/jbm.820040309.

[124] J.J. Klawitter, J.G. Bagwell, A.M. Weinstein, B.W. Sauer, J.R. Pruitt, An evaluation of bone growth into porous high density polyethylene, J. Biomed. Mater. Res. 10 (1976) 311–323. https://doi.org/10.1002/jbm.820100212.

[125] V. Karageorgiou, D. Kaplan, Porosity of 3D biomaterial scaffolds and osteogenesis, Biomaterials. 26 (2005) 5474–5491. https://doi.org/10.1016/j.biomaterials.2005.02.002.

[126] K. Prasad, O. Bazaka, M. Chua, M. Rochford, L. Fedrick, J. Spoor, R. Symes, M. Tieppo, C. Collins, A. Cao, D. Markwell, K. (Ken) Ostrikov, K. Bazaka, Metallic Biomaterials: Current Challenges and Opportunities, Materials (Basel). 10 (2017) 884. https://doi.org/10.3390/ma10080884.

[127] T. Kokubo, H. Takadama, How useful is SBF in predicting in vivo bone bioactivity?, Biomaterials. 27 (2006) 2907–2915. https://doi.org/10.1016/J.BIOMATERIALS.2006.01.017.

[128] A. Ruksudjarit, K. Pengpat, G. Rujijanagul, T. Tunkasiri, Synthesis and characterization of nanocrystalline hydroxyapatite from natural bovine bone, Curr. Appl. Phys. 8 (2008) 270–272. https://doi.org/10.1016/j.cap.2007.10.076.

[129] G. Lutzweiler, A.N. Halili, N.E. Vrana, The overview of porous, bioactive scaffolds as instructive biomaterials for tissue regeneration and their clinical translation, Pharmaceutics. 12 (2020) 1–29. https://doi.org/10.3390/pharmaceutics12070602.

[130] H. Wang, J. Pieper, F. Péters, C.A. van Blitterswijk, E.N. Lamme, Synthetic scaffold morphology controls human dermal connective tissue formation, J. Biomed. Mater. Res. Part A. 74A (2005) 523–532. https://doi.org/10.1002/jbm.a.30232.

[131] Use of bioactive glass compositions to stimulate osteoblast production, (2001).

[132] M. Bohner, J. Lemaitre, Can bioactivity be tested in vitro with SBF solution?, Biomaterials. 30 (2009) 2175–2179. https://doi.org/10.1016/j.biomaterials.2009.01.008.

[133] H.M. Kim, T. Himeno, M. Kawashita, T. Kokubo, T. Nakamura, The mechanism of biomineralization of bone-like apatite on synthetic hydroxyapatite: an in vitro assessment., J. R. Soc. Interface. 1 (2004) 17. https://doi.org/10.1098/RSIF.2004.0003.

[134] M. Ansari, S. Morteza Naghib, F. Moztarzadeh, A. Salati, SYNTHESIS AND CHARACTERIZATION OF HYDROXYAPATITE-CALCIUM HYDROXIDE FOR DENTAL COMPOSITES, 2011.

[135] S. Nasiri, M. Hosseinnezhad, M. Rabiei, A. Palevicius, G. Janusas, The effect of calcination temperature on the photophysical and mechanical properties of copper iodide (5 mol%)–doped hydroxyapatite, Opt. Mater.

(Amst). 121 (2021) 111559.
https://doi.org/10.1016/J.OPTMAT.2021.111559.

[136] D.S. Gomes, A.M.C. Santos, G.A. Neves, R.R. Menezes, A brief review on hydroxyapatite production and use in biomedicine, Ceramica. 65 (2019) 282–302. https://doi.org/10.1590/0366-69132019653742706.

[137] M. Schuth, F. Vössing, L. Yang, A Shearographic Endoscope for Nondestructive Test, J. Hologr. Speckle. 1 (2004) 46–52. https://doi.org/10.1166/jhs.2004.007.

[138] Y.M. He, C.J. Tay, H.M. Shang, A new method for generating and analysing digital speckle shearing correlation fringe patterns, Opt. Laser Technol. 30 (1998) 27–31. https://doi.org/10.1016/S0030-3992(97)00062-5.

6. CURRICULUM VITAE

Name, surname: Marzieh Rabiei
E-mail: marzieh.rabiei@ktu.edu

Education:
2004–2009 Bachelor's Degree
in Materials Engineering, Islamic Azad University, Shahreza Branch, Faculty of Materials Engineering

2010–2012 Master's Degree
in Materials Engineering, Islamic Azad University, Najafabad Branch, Faculty of Materials Engineering

2019–2023 PhD studies
in Mechanical Engineering, Kaunas University of Technology, Department of Mechanical Engineering

Work experience:
May 01, 2020–December 18, 2020
Project: "Development of new technology for the formation of microstructures in functional materials (01.2.2-CPVA-K-703)", Department of Mechanical Engineering and Design, Kaunas University of Technology

7. LIST OF PUBLICATIONS

1. [S1; CH; OA] **Rabiei, Marzieh**; Palevicius, Arvydas; Monshi, Ahmad; Nasiri, Sohrab; Vilkauskas, Andrius; Janusas, Giedrius. Comparing methods for calculating nano crystal size of natural hydroxyapatite using X-Ray diffraction // Nanomaterials. Basel : MDPI. ISSN 2079-4991. 2020, vol. 10, iss. 9, art. no. 1627, p. 1-21. DOI: 10.3390/nano10091627. [Science Citation Index Expanded (Web of Science); Scopus; Academic Search Complete] [IF: 5,076; AIF: 6,588; IF/AIF: 0,770; Q1 (2020, InCites JCR SCIE)], https://www.mdpi.com/2079-4991/10/9/1627
2. [S1; CH; OA] **Rabiei, Marzieh**; Palevicius, Arvydas; Dashti, Amir; Nasiri, Sohrab; Monshi, Ahmad; Vilkauskas, Andrius; Janusas, Giedrius. Measurement modulus of elasticity related to the atomic density of planes in unit cell of crystal lattices // Materials. Basel : MDPI. ISSN 1996-1944. 2020, vol. 13, iss. 19, art. no. 4380, p. 1-17. DOI: 10.3390/ma13194380. [Science Citation Index Expanded (Web of Science); Scopus; Academic Search Complete] [IF: 3,623; AIF: 5,678; IF/AIF: 0,638; Q1 (2020, InCites JCR SCIE)] [CiteScore: 4,20; SNIP: 1,261; SJR: 0,682; Q2 (2020, Scopus Sources)], https://www.mdpi.com/1996-1944/13/19/4380
3. [S1; CH; OA] **Rabiei, Marzieh**; Palevicius, Arvydas; Nasiri, Sohrab; Dashti, Amir; Vilkauskas, Andrius; Janusas, Giedrius. Relationship between Young's modulus and planar density of unit cell, super cells (2×2×2), symmetry cells of Perovskite (CaTiO3) lattice // Materials. Basel : MDPI. ISSN 1996-1944. 2021, vol. 14, iss. 5, art. no. 1258, p. 1-15. DOI: 10.3390/ma14051258. [Science Citation Index Expanded (Web of Science); Scopus; DOAJ] [IF: 3,623; AIF: 5,678; IF/AIF: 0,638; Q1 (2020, InCites JCR SCIE)], https://www.mdpi.com/1996-1944/14/5/1258
4. [S1; CH; OA] **Rabiei, Marzieh**; Palevicius, Arvydas; Dashti, Amir; Nasiri, Sohrab; Monshi, Ahmad; Doustmohammadi, Akram; Vilkauskas, Andrius; Janusas, Giedrius. X-ray diffraction analysis and Williamson- Hall method in USDM model for estimating more accurate values of stress-strain of unit cell and super cells (2×2×2) of hydroxyapatite, confirmed by ultrasonic pulse-echo test // Materials. Basel : MDPI. ISSN 1996-1944. 2021, vol. 14, iss. 11, art. no. 2949, p. 1-16. DOI: 10.3390/ma14112949. [Science Citation Index Expanded (Web of Science); Scopus; DOAJ] [IF: 3,623; AIF: 5,678; IF/AIF: 0,638; Q1 (2020, InCites JCR SCIE)] [CiteScore: 4,20; SNIP: 1,261; SJR: 0,682; Q2 (2020, Scopus Sources)], https://www.mdpi.com/1996-1944/14/11/2949
5. [S1; CH; OA] **Rabiei, Marzieh**; Palevicius, Arvydas; Ebrahimi-Kahrizsangi, Reza; Nasiri, Sohrab; Vilkauskas, Andrius; Janusas, Giedrius. New approach for preparing In vitro bioactive scaffold consisted of Ag-doped hydroxyapatite + polyvinyltrimethoxysilane // Polymers. Basel: MDPI. ISSN 2073-4360. 2021, vol. 13, iss. 11, art. no. 1695, p. 1-19. DOI: 10.3390/polym13111695. [Science Citation Index Expanded (Web of Science); Scopus; DOAJ] [IF: 4,329; AIF: 4,658; IF/AIF:

0,929; Q1 (2020, InCites JCR SCIE)] [CiteScore: 4,70; SNIP: 1,200; SJR: 0,770; Q1 (2020, Scopus Sources)],
https://www.mdpi.com/2073-4360/13/11/1695

6. [S1; NL] Nasiri, Sohrab; Hosseinnezhad, Mozhgan; **Rabiei, Marzieh**; Palevicius, Arvydas; Janusas, Giedrius. The effect of calcination temperature on the photophysical and mechanical properties of copper iodide (5 mol%)–doped hydroxyapatite // Optical materials. Amsterdam : Elsevier. ISSN 0925-3467. eISSN 1873-1252. 2021, vol. 121, art. no. 111559, p. 1-12. DOI: 10.1016/j.optmat.2021.111559. [Science Citation Index Expanded (Web of Science); Scopus] [IF: 3,080; AIF: 4,623; IF/AIF: 0,666; Q2 (2020, InCites JCR SCIE)] [CiteScore: 4,80; SNIP: 0,955; SJR: 0,598; Q2 (2020, Scopus Sources)],
https://www.sciencedirect.com/science/article/pii/S092534672100759X

Participation in international conferences

1. **Rabiei, Marzieh**; Ebrahimi-Kahrizsangi, Reza; Nasiri, Sohrab. New approach for fabricating scaffold consisted of Ag-doped hydroxyapatite/polyvinyltrimethoxysilane // IRWBM 2021: 2nd international research workshop in biomechanical microsystems 2021: 22 October 2021, Kaunas University of Technology, Lithuania: program and abstracts. Kaunas: Kaunas University of Technology. 2021, p. 16.
2. **Rabiei, Marzieh**; Nasiri, Sohrab; Palevicius, Arvydas; Janusas, Giedrius. Modified Williamson-Hall method in USDM model for estimating more accurate values of Young's modulus of hydroxyapatite // Advanced materials and technologies: book of abstracts of 23rd international conference-school, 23–27 August 2021, Palanga, Lithuania. Kaunas: Kaunas University of Technology. ISSN 2669-1930. 2021, C-P173, p. 207.
3. **Rabiei, Marzieh**; Palevicius, Arvydas; Janusas, Giedrius; Nasiri, Sohrab. Direct interface between Young's modulus and planar density of $CaTiO_3$ // 8th international conference on mechanical, construction, industrial and civil engineering, 22 August 2021. Istanbul. Civilica. 2021, 48, pp. 1–32.
4. **Rabiei, Marzieh**; Palevicius, Arvydas; Janusas, Giedrius; Nasiri, Sohrab. Young's modulus versus planar density of unit cells, super cells, symmetry cells of $CaTiO_3$ // Fourth conference on technology development in mechanical and aerospace engineering: 22 July 2021, Tehran, Iran. Civilica. 2021, 28, pp. 1–14.
5. **Rabiei, Marzieh**; Palevicius, Arvydas; Janušas, Giedrius. Fabrication and investigation of bioactivity nano-composite obtained form PVB-co-VA-co-VAc/HA // Advanced materials and technologies: book of abstracts of 22nd international conference-school, 24–28 August 2020, Palanga, Lithuania. Kaunas: Kaunas University of Technology. ISSN 1822-7759. 2020, A-P121, p. 150.
6. **Rabiei, Marzieh**; Nasiri, Sohrab; Palevicius, Arvydas; Janusas, Giedrius. Preparation and investigation of bioactive organic-inorganic nano-composite derived from PVB-co-VA-coVAc/HA // MSM 2020: 15th international conference mechatronic systems and materials, 1–3 July 2020, Białystok, Poland: book of abstracts. Bialystok: Bialystok University of Technology. 2020, p. 18.
7. **Rabiei, Marzieh**; Monshi, Ahmad. A novel approach of nano monolith based on bio glass 45S5, with entering PVTMS // IRWBM 2019: International research workshop in biomechanical microsystems 2019, 23 October 2019, Kaunas University of Technology, Lithuania: program and abstracts. Kaunas, 2019, p. 12.

8. ACKNOWLEDGMENTS

Prof. Habil. Dr. Arvydas Palevicius (Kaunas University of Technology, Technological Sciences, Mechanical Engineering) is sincerely thanked for the supervision of my doctoral research, consultations, valuable advice, and great support.

Prof. Habil. Dr. Giedrius Janusas (Kaunas University of Technology, Technological Sciences, Mechanical Engineering) is kindly thanked for advising on my study, measurements of mechanical properties, characteristics, for sharing knowledge in elastic modulus, and valuable scientific discussions.

UDK 546.41.057+539.32+620.3](043.3)

SL 344. 2022-*-*, * leidyb. apsk. l. Tiražas 14 egz. Užsakymas X
Išleido Kauno technologijos universitetas, K. Donelaičio g. 73, 44249 Kaunas
Spausdino leidyklos „Technologija“ spaustuvė, Studentų g. 54, 51424 Kaunas